ABSTRACT

Title of Dissertation:	PERFORMANCE AND DURABILITY ENHANCEMENT OF SOLID OXIDE FUEL CELL ELECTRODES VIA SURFACE MODIFICATION
	Ian Alexander Robinson, Doctor of Philosophy, 2020
Dissertation directed by:	Professor, Eric Wachsman Ph.D., Materials Science and Engineering

Solid oxide fuel cells (SOFCs) electrochemically convert chemical fuels to usable electricity with high efficiency and can operate on any oxidizable fuel. SOFCs fuel flexibility is accompanied by clean conversion by only converting the fuel to H_2O and CO_2 without the production of NO_x. Additionally, the design of the device allows for a facile integration of carbon capture because the exhaust from the anode and cathode are already separated, allowing for a separated CO_2 stream for carbon capture. Technical limitations have prohibited the commercial deployment of SOFCs at an impactful scale and the SOFC market is currently worth <$1 billion. The high operating temperature (T>800 °C) of SOFCs limits possible applications due to high degradation rates within cell components and a high balance of plant costs to use the requisite

specialized high temperature materials. The primary limitation to using a lower temperature SOFC is the sluggish kinetics of the air electrode or cathode oxygen reduction reaction (ORR) at lower temperatures. This work increases the activity and durability of SOFC electrodes at lower temperatures by utilizing a facile, effective, low cost surface modification technique, defect engineering, and universal cathode scaffold design. Surface modification of SOFC cathodes also prevents the deactivation of the SOFC cathode typically caused by contaminant gasses like CO_2 in $Sr_{0.5}Sm_{0.5}CoO_{3-\delta}$ (SSC) cathodes. The surface modification technique also shows breakthroughs in the activity of SOFC cathodes SSC and $La_{1-x}Sr_xCo_{1-y}Fe_yO_{3-\delta}$ (LSCF), allowing the SOFC to operate below 600 °C.

The use of an engineered porous functional layer is shown to reduce the electronic leakage current in ceria-based electrolytes. This type of functional layer also increases the overall performance and durability of a SOFC at lower temperatures. Additionally, an approach was developed to deposit any desired cathode electrocatalyst on a universal scaffold to enable low-temperature operation and is compatible with existing cell components. 1 W/cm^2 at 550 °C is achieved by utilizing the scaffold infiltration approach and demonstrates that high performance operations at low temperatures is achievable. Finally, the fuel flexibility of metal-supported solid oxide fuel cells (MS-SOFCs) was demonstrated to highlight their potential applications for carbon neutral transportation.

PERFORMANCE AND DURABILITY ENHANCEMENT OF SOLID OXIDE FUEL CELL ELECTRODES VIA SURFACE MODIFICATION

by

Ian Alexander Robinson

Dissertation submitted to the Faculty of the Graduate School of the
University of Maryland, College Park, in partial fulfillment
of the requirements for the degree of
Doctor of Philosophy
2020

Advisory Committee:
Professor Eric Wachsman, Chair
Professor Isabel Lloyd
Professor Liangbing Hu
Professor Lourdes Salamanca-Riba
Professor Christopher Cadou

Acknowledgements

I would like to thank my advisor Professor Eric Wachsman for guiding me from my undergraduate studies through my dissertation research as a Ph.D. student.

I would also like to thank my two mentors Hussain Abdul Jabbar and Yi-Lin Huang for their experimental guidance throughout both my graduate and undergraduate studies.

I also would like to thank the other Wachsman group members who I collaborated with during my studies: Sam Horlick, Evans Gritton, Mann Sakbodin, Chris Pellegrinelli, Patrick Stanley, Tom Hays, Alireza Pesaran and Greg Hitz.

I thank my undergraduate students who aided me in my research along the way: Haley Kaplan, Jonathan Obenland, and Nick Robinson.

I would also like to thank the Tucker group at LBNL for teaching me about testing metal-supported SOFCs.

I would also like to thank my friends and family for their support during this process and for encouraging me along the way.

Lastly, I would like to thank my fiancée Amanda for her support during the entire length of my graduate studies.

Table of Contents

List of Tables

List of Figures

List of Abbreviations

ADMM- Alternating Direction Method of Multipliers

AFL - Anode Functional Layer

ASL – Anode Support Layer

ASR - Area Specific Resistance

BSCF - $Ba_{0.5}Sr_{0.5}Co_{1.5}Fe_{0.5}O_{3-\delta}$

CTE – Coefficient of Thermal Expansion

DEL – Dense Electrolyte Layer

DME – Dimethyl Ether

DRT- Distribution of Relaxation Times

EELS – Electron Energy Loss Spectroscopy

EDS- X-ray Energy Desorption Spectroscopy

EIS- Electrochemical Impedance Spectroscopy

FE – Faradaic Efficiency

FIB – Focused Ion Beam

FRA – Frequency Response Analyzer

GDC- $Gd_xCe_{1-x}O_{2-\delta}$

HAADF – High-Angle Annular Dark Field

HR-TEM – High Resolution TEM

iV – Current Voltage

LSC- $La_{1-x}Sr_xCoO_{3-\delta}$

LSCF- $La_xSr_{1-x}Fe_{1-y}Co_yO_{3-\delta}$

LSM- $La_xSr_{1-x}MnO_{3-\delta}$

LT-SOFC- Low Temperature SOFC

MIEC -Mixed Ionic Electronic Conductivity

MS-SOFC – Metal Supported SOFC

ORR- Oxygen Reduction Reaction

OCV- Open Circuit Voltage

PBCC - $PrBa_{0.8}Ca_{0.2}Co_2O_{5+\delta}$

PBSCF- $PrBa_{0.5}Sr_{0.5}Co_{1.5}Fe_{0.5}O_{5+\delta}$

PCFC- Protonic Ceramic Fuel Cell

pCO_2 – Partial pressure of CO_2

PCO - $Pr_xCe_{1-x}O_{2-\delta}$

PEM - Proton Exchange Membrane

PFL – Porous Functional Layer

PGM – Platinum Group Metal

pO_2- Partial pressure of oxygen

PPD – Peak Power Density

5-5-90 Pr-Sm-GDC – 5 wt% Pr 5wt% Sm 90 wt% GDC

PSC- Pr-Sr-Co (1-1-2 Molar Ratio)

Pr-SM- Pr Surface Modification

SDC - $Ce_{1-x}Sm_xO_{2-\delta}$

SM – Surface Modification

SOC- Solid Oxide Cell

SOEC – Solid Oxide Electrolysis Cell

SOFC – Solid Oxide Fuel Cell

SSC – $Sr_{0.5}Sm_{0.5}CoO_{3-\delta}$

STFC - $SrTi_{0.3}Fe_{0.55}Co_{0.15}O_{3-\delta}$

TEM – Transmission Electron Microscopy

t_{o2-} - oxygen ion transference number

ToF-SIMS – Time of Flight Secondary Ion Mass Spectroscopy

TPB – Triple Phase Boundary

TPD – Temperature Programmed Desorption

TPO – Temperature Programmed Oxidation

V_{th}- Theoretical Voltage

YSZ- $Y_xZr_{1-x}O_{2-\delta}$

Chapter 1. Introduction to Solid Oxide Fuel Cells

1.1 SOFC Background

Solid oxide fuel cells (SOFC) are a promising energy conversion technology that electrochemically converts fuels to electricity by using any oxidizable fuel including those as simple as hydrogen and hydrocarbons. [1–10] SOFCs can convert fuels to electricity with much higher efficiency than typical energy conversion technologies as they are not limited by Carnot thermodynamic principles. [4,5,11] Their high energy conversion efficiency and fuel flexibility make SOFCs an attractive energy conversion technology that can also integrate with current energy storage technologies and refueling infrastructure to move towards a decarbonized future. [11–13]

SOFCs consist of three main components: an air electrode or cathode, a fuel electrode or anode, and a gas-tight oxygen permeable membrane functioning as the electrolyte. SOFCs operate at a much higher temperature (T > 500 °C) compared to other fuel cell technologies like proton exchange membranes (PEM) or alkaline fuel cells which operate below 100 °C. [14,15] A higher temperature of operation allows for the use of much cheaper electrode catalysts than PEM fuel cells, which use platinum group metal catalysts for their anode and cathode. The electrodes in SOFCs are typically nickel on the anode, a cobalt oxide cathode, and a zirconia or ceria-based electrolyte. [12] The nickel and cobalt catalysts are much cheaper and more available as compared to the platinum group metal PGM catalysts of a PEM, and the oxide electrolyte allows for the use of any oxidizable fuel. A PEM fuel cell is limited to using

hydrogen fuel, which adds a much higher level of complexity because hydrogen storage and refueling infrastructure is not yet widely available. Cheap and available catalysts paired with the ability to leverage existing energy infrastructure make SOFCs the best clean, energy efficient conversion technology that can be integrated with the existing electrical grid.

1.2 SOFC Operating Principle

As stated previously, SOFCs consist of three major components: an anode, cathode, and electrolyte. Fuel is delivered to the anode side when air on the cathode side and the fuel-air environments are separated by a gas-tight oxygen ion conducting electrolyte, thus generating an electrochemical potential. This potential is shown below in the Nernst equation[16]:

$$V_{th} = \frac{RT}{nF} ln\left(\frac{P_{O_2}^{cathode}}{P_{O_2}^{anode}}\right) \quad [1.1]$$

The V_{th} is the theoretical Nernst potential generated at the specific temperature (T), depending on the charge of the ion (n) and the partial pressure of each respective electrode ($P_{O2}^{cathode}$, P_{O2}^{anode}). R and F are the ideal gas constant and Faraday constant, respectively. The voltage is typically ~1.1 V when operating on hydrogen and air at the anode and cathode respectively under SOFC operating temperatures (T = 500-800 °C) with a pure ionically conducting electrolyte. Some electrolytes, however, are not purely ionically conductive; they are mixed ionic electronic conducting (MIEC). The transference number (t_{O2-}) of a material quantifies its relative ionic to electronic conductivity as shown in the equation below:

$$t_{O2-} = \frac{\sigma_{ionic}}{(\sigma_{ionic} + \sigma_{electronic})} \quad [1.2]$$

In this equation, σ_{ionic} is the ionic conductivity of the material and $\sigma_{electronic}$ is the electronic conductivity of the material. Conventional high temperature SOFCs use $Y_{1-x}Zr_xO_{2-\delta}$ (YSZ) electrolytes, which have an oxygen transference number of ~1 compared to the lower temperature alternative $Gd_xCe_{1-x}O_{2-\delta}$ (GDC) which has an ionic transference number closer to ~0.8-0.9. [17] The lower transference number causes GDC electrolyte-based cells to have a lower voltage.

Each cell component undergoes its own half reaction that contributes to the overall reaction. Oxygen from the air is reduced in the cathode, then oxygen ions are transported across the oxygen-conducting electrolyte to oxidize the fuel on the anode side. Two electrons are generated as a result of that process and balance the charge of oxygen ions oxidizing the fuel on the anode. The equations below show the case of hydrogen operation. Equation 1.3 shows the hydrogen oxidation in the anode, Equation 1.4 shows the oxygen reduction in the cathode, and Equation 1.5 shows the overall reaction for hydrogen oxidation.

$$H_2 + O^{2-} \leftrightarrow H_2O + 2e^- \quad [1.3]$$

$$\frac{1}{2}O_2 + 2e^- \leftrightarrow O^{2-} \quad [1.4]$$

$$H_2 + \frac{1}{2}O_2 \leftrightarrow H_2O \quad [1.5]$$

Figure 1.1 depicts a simple diagram of a SOFC's operations, including the anode, cathode, and electrolyte. Each electrode requires their respective reaction to occur at a triple phase boundary (TPB) where there are three phases, gas phase fuel or air, an

electronic conductor to draw the produced electrons to the external circuit, and an ionic conductor to transport oxygen to the electrolyte. The TPB reaction requirement demonstrates that electrode materials have intrinsic requirements and are to be electronically conductive, ionically conductive, and active towards the specific electrode reaction.

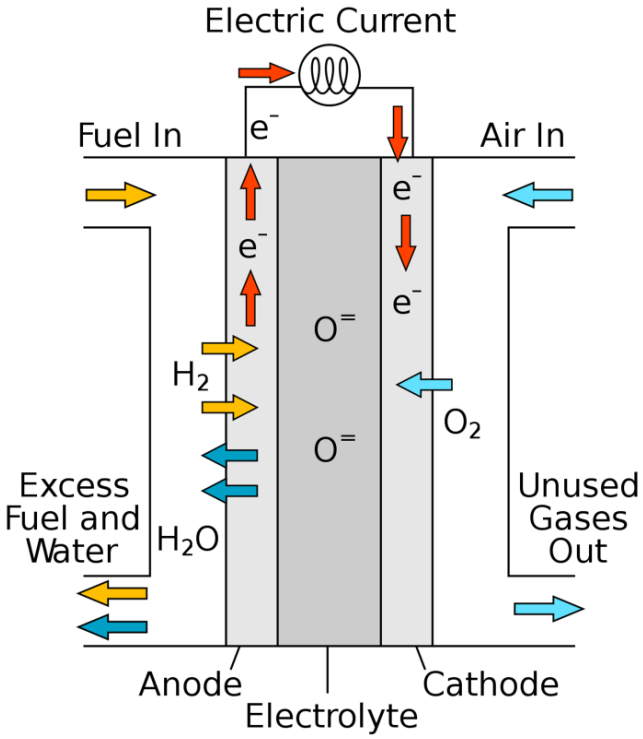

Figure 1.1 Solid Oxide Fuel Cell Operation[18]

1.3 SOFC Design, Materials, and Challenges

To minimize resistive losses in the SOFC, the SOFC is typically designed to be supported by the anode.[19] There is consensus that the cathode reaction and electrolyte losses contribute to the highest resistive losses in SOFCs. SOFC anodes are typically very conductive and nickel is a strong catalyst for hydrogen oxidation [20]. Traditional SOFC anodes are a composite of Ni and the electrolyte material $Gd_xCe_{1-x}O_{2-\delta}$ (GDC) or $Y_{1-x}Zr_xO_{2-\delta}$ (YSZ). Ni provides the mechanical support for the entire cell, electronic

conduction in the anode, and activity towards the anode reaction. The electrolyte material provides ionic conductivity of oxygen to the anode TPB. The electrolyte, as noted before, should be as thin as possible because its only function is to provide a gas-tight oxygen permeable membrane to transport oxygen ions. Electrolyte resistance losses are directly proportional to the thickness of the electrolyte, so it is critical to make the electrolyte as thin as possible without causing defects that would cause a drop in cell voltage. The SOFC cathode is also a thin layer and does not provide much mechanical strength because perovskites are very brittle and weak. Because the cathode is thought to be the rate limiting step in LT-SOFCs, it is also advantageous to reduce its thickness. Theses optimal configurations result in an anode that is about 500 μm thick, an electrolyte that is 10s of μm thick, and a cathode that is 10s of μm thick. A typical anode-supported SOFC configuration is shown in an SEM image below in Figure 1.2.

Currently SOFCs operate at very high temperatures (T > 700 °C) due to sluggish electrode kinetics, namely the oxygen reduction reaction (ORR) in the cathode that is very slow at low temperatures due to the energy needed to break the O=O double bond. SOFC cathode materials are typically based on a perovskite with ABO_3 structure, consisting of an alkaline earth metal on the A site (Sr or Ba), and a transition metal (Co, Fe, or Mn) on the B site of the perovskite.[21–23] As the alkaline earth metal is meant to be stable in air while the B site material is thought to provide the activity for the cathode reaction, materials like $La_xSr_{1-x}MnO_{3-\delta}$ (LSM), $La_xSr_{1-x}Fe_{1-y}Co_yO_{3-\delta}$ (LSCF), and $La_{1-x}Sr_xCoO_{3-\delta}$ (LSC) are often used for SOFC cathodes. LSM and LSCF are relatively active at higher temperatures (T > 700 °C) but have very little activity at lower

temperatures (T < 600 °C). These materials have issues operating at higher temperatures because there is a tradeoff with the stability of electrode components and activity towards electrode reactions. Degradation rates for these materials are too high at elevated temperatures (T > 700 °C) and stack components, namely chromate-based interconnects, are too expensive. [24–26] For these reasons, lowering the operating temperature of SOFCs is a critical barrier to commercialization.

Lower temperature operation also provides a unique set of challenges which are primarily focused on cathode activity but also includes other hurdles. Yttria stabilized zirconia, $Y_{1-x}Zr_xO_{2-\delta}$ (YSZ), electrolytes do not have sufficient ionic conductivity at lower temperatures. Cobaltite (LSCF, LSC) type cathodes, the state-of-the-art low temperature cathode, react with YSZ and lower its ionic transference number. This requires the use of $Gd_xCe_{1-x}O_{2-\delta}$ GDC barrier layers which add extra resistance to the cell and therefore lowers the efficiency. Among these issues, LSCF and LSM do not have sufficient activity to operate at lower temperatures as their area specific resistance is ~1-10 Ωcm^2 at 500 °C. [27] As a result of these issues, new materials must be designed to allow SOFCs to operate at lower temperatures.

If the SOFC operating temperature is reduced, the degradation mechanisms do not necessarily vanish but only slow down kinetically. While some intrinsic degradation mechanisms still exist at low temperatures, most can be mitigated. For example, strontium is contained in the majority of SOFC cathode materials, and, during operation, strontium segregates out of the lattice and forms SrO on the surface of the inactive cathode. Cathodes that contain cobalt also have the same segregation issue where cobalt leaves the cathode and reacts with the YSZ electrolyte, increasing the

electronic conduction in YSZ and decreasing the transference number. Also, because of the current high operating temperature, cathode particles coarsen during operation which decrease the TPB length. Other degradation mechanisms consist of contaminant gasses and material incompatibility of other cell components. Strontium-based cathodes react with ambient CO_2 in the air which forms strontium carbonate on the surface of the cathode. Strontium carbonate is an insulating phase that blocks active sites similar to SrO. [28,29]

The anode also presents degradation mechanisms that are problematic to SOFCs, including the redox instability of the anode. Traditional SOFC anodes are ceramic-metal composites in which nickel is mixed with the electrolyte material GDC or YSZ. Nickel provides electronic conductivity and activity towards the fuel reaction and the electrolyte material provides ionic conductivity to form the triple phase boundary at the Ni-electrolyte material interface. If the anode is put under an oxidizing condition and then a reducing condition, the thin electrolyte can crack due to the ~40% volume expansion and contraction between Ni and NiO. Ni also coarsens in the anode which reduces overall active sites. In the case of a ceramic anode, the elements in the ceramic suffer from the same exsolution/segregation mechanisms as the cathode.

Extrinsic degradation mechanisms on the anode are mainly caused by operation on hydrocarbon fuels. Ni is a strong enough catalyst to break the C-H bond, however if there is not oxygen present during the cleavage of the C-H bond, carbon does not react with O to form CO or CO_2 causing solid carbon, or coke, to accumulate on the surface of the anode. [30–32] The solid carbon on the surface of the anode is problematic for SOFCs operating on carbonaceous fuels because the accumulated carbon bonds to

the nickel and deactivates the anode. The use of proton conductors in the anode has shown promise in preventing coking in fuel cell anodes in either a SOFC or PCFC configuration.[10,33,34] The perceived mechanism is that the hydrocarbon chain does not cleave at the C-H bond. Rather, C-OH intermediates are formed, preventing the formation of solid carbon.[33] However, the landmark studies utilizing protonic ceramic fuel cells (PCFCs) for this method require fuel dilution with water by over 50% which in turn would decrease the volumetric energy density of a fuel and is not desirable for transportation applications.[33] Sulfur species are another contaminant that naturally occurs in natural gas and other hydrocarbon fuels. Sulfur will readily react with Ni in the anode and form NiS, which is inactive and prevents the necessary anode reactions.[35–37] In the case of a hydrocarbon fuel, the anode will coke further leading to a quick degradation and deactivation of the cell. Preliminary results show that sulfur tolerance can be improved with ceria infiltration on the surface of the anode.[38] Further work should be done to observe this effect over the lifetime of a SOFC operation.

The focus of this work is to increase electrode activity in both the anode and cathode to lower the operating temperature of SOFCs. The primary approaches used are the surface modification SOFC electrodes through solution infiltration (explained in Chapter 2), defect engineering of a porous functional layer to increase the oxygen ion transference number in GDC based electrolytes, solution infiltration of a universal cathode scaffold for cathodes with high activity at lower temperatures with mitigated degradation, and the operation of metal supported SOFCs (MS-SOFC) on alternative fuels to explore their potential application for transportation.

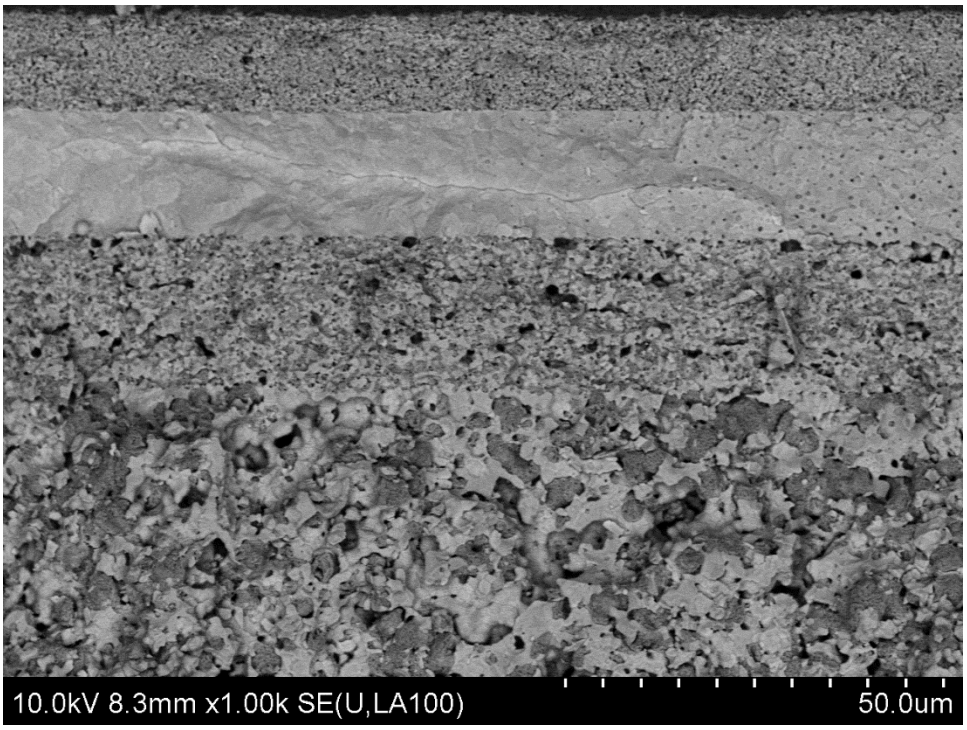

Figure 1.2 SEM of Anode Supported SOFC. SSC-GDC Cathode, GDC Electrolyte, Ni-GDC Anode Support and Functional Layer.

Chapter 2. Experimental Methods

2.1 Solid Oxide Fuel Cell Production

Current commercial SOFCs are either anode supported, or electrolyte supported. [15] These two configuration types require the use of ceramic processing to produce the anode, electrolyte, and cathode. Producing this ceramic or cermet supported device requires the use of roll-roll processing to scale up and deploy SOFCs on a commercial scale. Typical lab scale (cell size < 1") research uses non-scalable techniques to produce their SOFC materials for basic materials testing. This process consists of using a select amount of anode material, pressing it into a pellet and dip coating or slurry coating the electrolyte on the anode. The green anode + electrolyte pellet is then fired into a furnace to co-sinter the two layers together and form an anode-electrolyte "half-cell". The cathode is then screen printed on top of the dense electrolyte. This technique is not scalable to a commercial scale as pressing pellets is not necessarily a roll-roll process.

The most advantageous technique to scale up SOFCs for commercial production is called tape casting. Tape casting is a traditional ceramic processing method that allows for roll-roll processing. Tape casting consists of synthesizing a slurry of a specific cell component which consists of the ceramic powder, solvents, an organic binder, and a plasticizer. The organic binder binds the ceramic powder together while the plasticizer creates a composite of the ceramic and organic matrix. This slurry is deposited into a doctor blade which is on a conveyor belt type mechanism and the blade height is adjusted to control the thickness of the tape. The tape is then dried to

remove an additional solvent used in the slurry preparation procedure. The result is a long sheet of ductile, workable green-body ceramic. This process is then repeated for each layer used to produce each cell component. At this point the ceramic layers are then laminated together using a heated roll laminator. The heat from the roll laminator heats the organic binder and plasticizer to laminate the anode-electrolyte. The laminated green body half-cell is then cut to the desired shape and fired into a furnace at high temperature to de-bind the tape, remove the organics from the organic-ceramic matrix, and sinter the ceramic powder together resulting in a dense sintered half-cell. A diagram for the tape casting process can be seen below in Figure 2.1.[39]

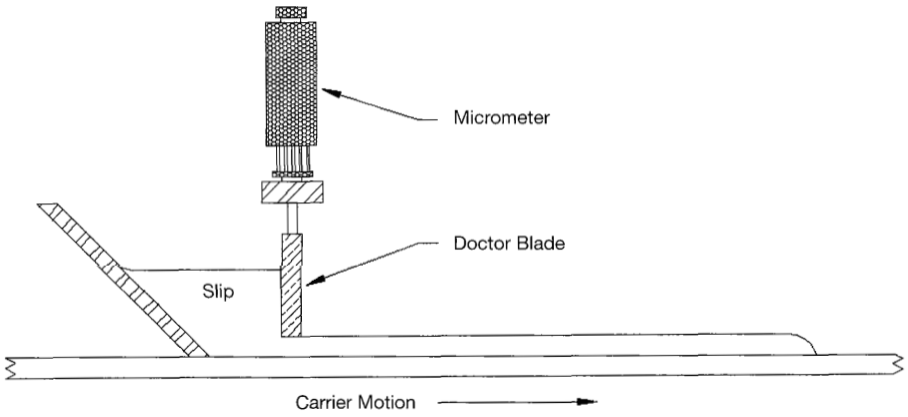

Figure 2.1 Tape Casting Method. Showing doctor blade, micrometers to control doctor blade height and slip in reservoir.

Cathode ink is prepared in a similar manner to that of a tape-casting slurry. The cathode ceramic is suspended in an organic ink vehicle solvent that is slightly more viscous than ethanol or water. The cathode ink is then screen printed on the electrolyte side of the anode-electrolyte half-cell and dried in a low temperature oven to remove the organic ink vehicle. The cell is then fired in a furnace, typically at a much lower temperature compared to the anode-electrolyte half-cell (T ~ 1000 °C vs T ~1500 °C),

resulting in an SOFC that is ready to be tested. The cell making procedure is shown in Figure 2.2 below starting with the ceramic powders showing each step required to make a cell.

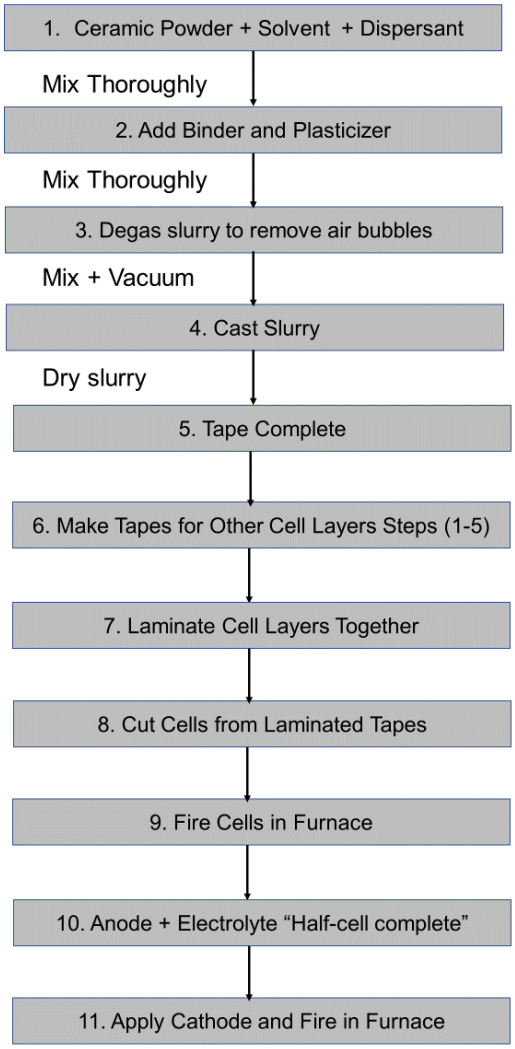

Figure 2.2 Cell Manufacturing Procedure. Beginning with ceramic powder and ending with cathode applied to Ni-GDC/GDC "half-cells".

Figure 1.2 from the previous chapter shows the SEM of this final sintered anode supported SOFC. Screen printing and tape casting are all roll-roll techniques that can be automated on a large scale as some commercial SOFC producers like Fuel Cell

Energy have shown. All of the cermet and ceramic full cells used in this work were produced by tape casting. Symmetric cells were produced by pressing GDC pellets (~1.5mm thick) and screen coating a cathode on the GDC.

2.2 Electrode Surface Modification

As stated previously, current SOFC electrodes do not have sufficient activity to operate at lower temperature. Synthesizing new electrodes for both the anode and cathode provide new challenges that existing electrodes do not face. For the case of an anode supported SOFC, a newly produced anode material must have a compatible shrinkage rate during sintering as well as a similar coefficient of thermal expansion (CTE), and a similar densification temperature to that of the electrolyte. The new anode material cannot react with the electrolyte as this can have detrimental effects to the defect chemistry of the electrolyte and lower the transference number. New SOFC cathode materials have similar requirements to that of the anode as they also need to have a similar coefficient of thermal expansion, lower sintering temperature, and no reaction with the electrolyte. A similar coefficient of thermal expansion is key so the cathode does not delaminate from the cell during operation.

Modifying the surface of existing SOFC electrodes is a great approach to introduce activity to electrodes and prevent degradation mechanisms. [22,23] Specifically, solution infiltration is the most promising technique to modify the surface of SOFC electrodes. Solution infiltration consists of dissolving metal salts into a solvent, depositing the solution onto the surface of the porous electrode, and thermally treating the infiltrated electrodes to form nanoparticles on the surface of the electrodes. The nanoparticles are active, can prevent degradation in the case of contaminant gasses, and

increase TPB length due to the high specific surface area of nanoparticles. The solution infiltration process can be seen in Figure 2.3. This process is repeated for a symmetric cell as needed to meet the desired nanoparticle loading requirements of the electrode.

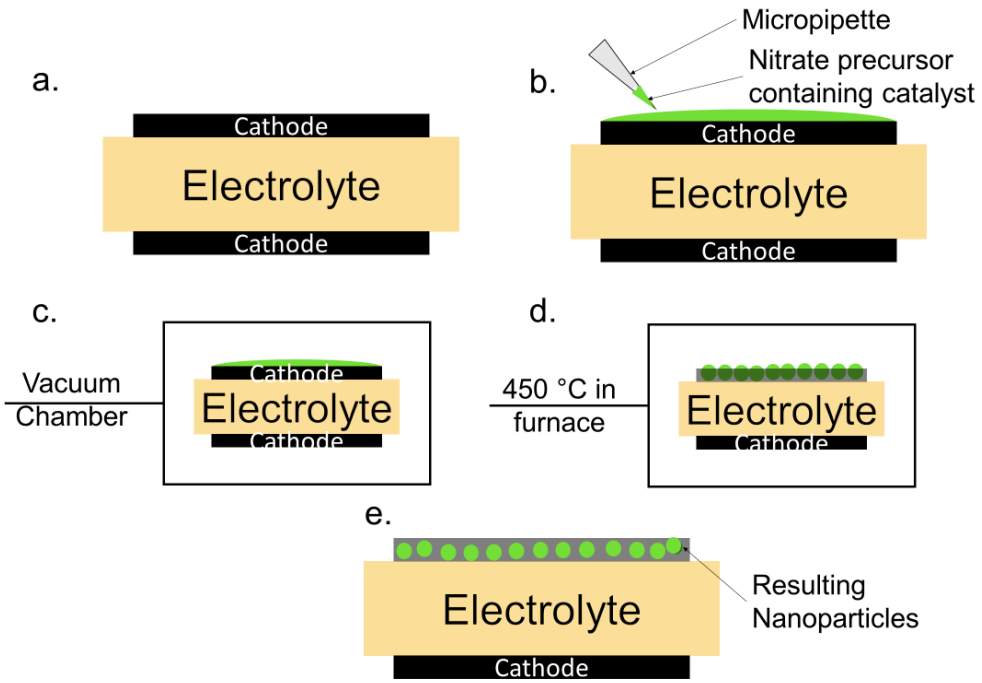

Figure 2.3 Electrode Modification via Solution Infiltration Cathode Symmetric Cell as an Example a. Starting cathode symmetric cell. **b.** Deposition of solution on the surface of the cathode. **c.** Infiltrated electrode is put under vacuum to wet solution into pores of electrode. **d.** Low temperature firing in the furnace to synthesize nanoparticles and remove organic solvent and nitrates. **e.** Final infiltrated cathode with nanoparticles on surface of the electrode. repeat steps **a.-e.** on other electrodes if it is a symmetric cell.

2.3 SOFC Material Characterization

Characterizing SOFC electrodes is accomplished by using a few critical techniques. The most fundamental electrochemical characterization for an electrode is performing electrochemical impedance spectroscopy (EIS) measurements on symmetric cells. Characterizing the full cell consists of measuring current-voltage behavior to understand how the cell voltage responds as a function of current, which is

called a galvanodynamic measurement. This is different from a symmetric cell as it probes all of the reactions at once compared to a symmetric cell where only the respective electrode measurement is probed. After the individual reactions are probed, the cell is put under operation by applying a constant current and measuring the voltage to understand how stable the full cell is and observe the changes in voltage over time. This is called a galvanostatic measurement. After the duration of the cell test, post-cell testing materials characterization is performed. These techniques are typically either surface analysis methods or electron microscopy images that help show how the microstructure changes overtime. Each characterization method will be explained in depth in its respective subsection

2.3.1 The Symmetric Cell Measurement and Electrochemical Impedance Spectroscopy

To isolate a specific cell half-reaction, symmetric cells are a good tool. Symmetric cells are the respective electrode, either anode or cathode, coated on both sides of an electrolyte pellet. An unmodified cathode symmetric cell is shown in Figure 2.3 a. as a visual aid. To evaluate the cathode performance in the symmetric cell configuration, EIS measurements are performed on the cell. EIS is a tool that probes charged species in a variety of fields, specifically for SOFCs. EIS probes respective half reactions in a symmetric cell and the overall redox reaction in a full cell.[40] EIS applies a time varied voltage signal at a fixed frequency and measures the current response and the result of E/I is impedance. This frequency is then varied, and a response is measured over a range of frequencies (10^{-1}-10^{6} Hz).[40] The response at different frequencies corresponds to reactions occurring in the electrode at different time constants. For example, the reactions occurring at high frequency (>10^{3} Hz) are

typically the transfer of charged species between electrode and electrolyte. For the case of cathode symmetric cells, the ORR occurs in the frequency range of 10^3-10^0 Hz. At frequencies below 10^0 Hz gas diffusion in the cathode microstructure is probed. Understanding the impedance response in each of these reaction regimes is critical in understanding the overall reaction regime. If there are significant impedance losses in the high frequency range, efforts may be made to increase the conductivity of the electrode material because charge transfer is dependent on conductivity. [41] If there are significant losses in the surface reaction regime, an ORR catalyst could be applied to the surface. If there are significant losses in the low frequency regime, porosity could be added to enable more effective gas diffusion through the microstructure.

In Figure 2.4, a Nyquist plot can be seen of an LSCF-GDC/GDC/LSCF-GDC symmetric cell. A Nyquist plot is the negative complex impedance response (-Z") vs the real impedance response (Z'). For a cathode symmetric cell, it is important to understand that the portion of impedance preceding the impedance arcs is designated as the electrolyte impedance. It is not of interest in this reaction measurement because the electrolyte does not contribute to the cathode reaction. The only portion of impedance under consideration in the symmetric cell measurement is the electrode impedance. In this case the pre-area corrected impedance is about 7 Ωcm^2. The area specific resistance (ASR) considers the overall impedance normalized to an area; the actual ASR is about 1 Ωcm^2 for this symmetric cell measured when considering the active area. In the case of a full cell, the total ASR, electrode ASR, and electrolyte ASR are considered. The electrolyte ASR is also known as the ohmic ASR as it is modeled by ohm's law V=IR and as a pure resistor in equivalent circuit modeling.

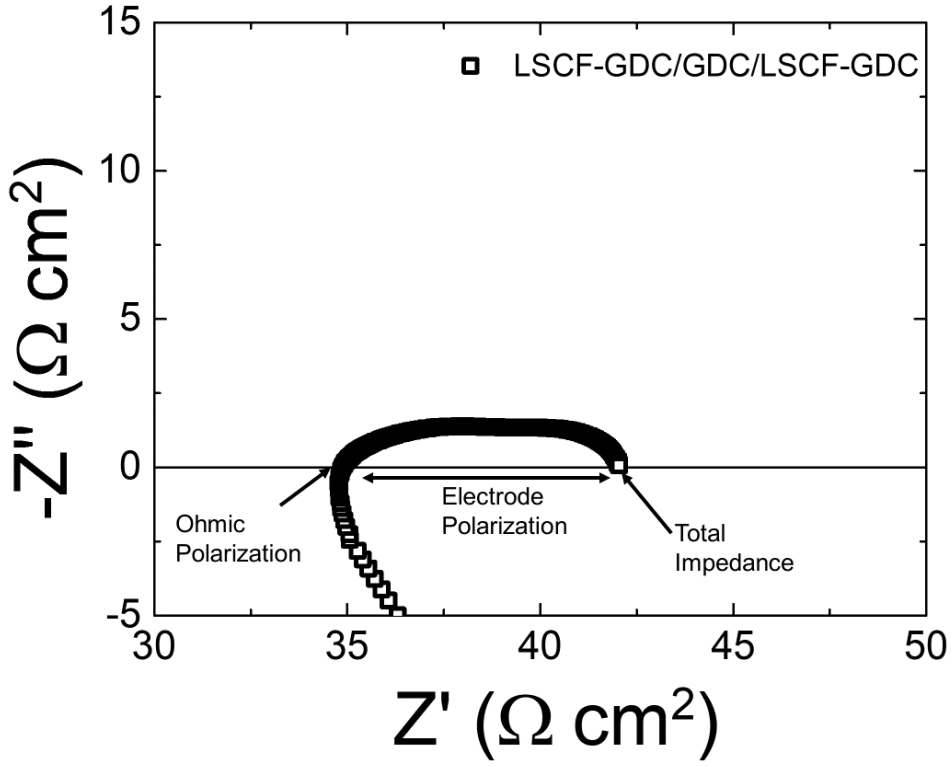

Figure 2.4 Nyquist Plot of LSCF-GDC/GDC/LSCF-GDC Symmetric Tested in Air at 650 °C.

To further understand electrode performance, the temperature of the testing environment and gas environment can be changed. Figure 2.4 shows the overall symmetric cell testing setup. The cell is sandwiched between two current collector meshes to ensure a strong electrical contact with the cell. The mesh is attached to leads that are wired back to the impedance analyzer. In this case the impedance analyzer is a Solartron (1470E cell test system) capable of testing eight cells simultaneously. There is a thermocouple wired back to the furnace that is used to heat the cell to the desired temperature. The gas delivery tube is fed directly next to the cell with an outlet on the other side of the reactor.

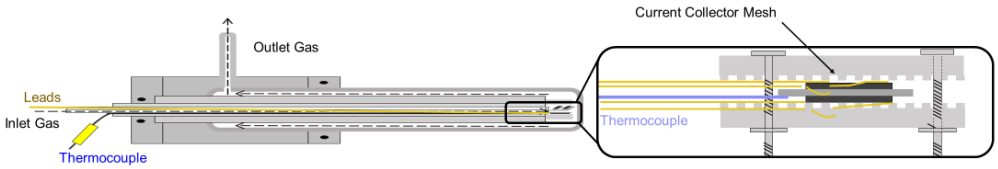

Figure 2.5 Symmetric Cell Testing Reactor. Ability to probe EIS in a range environment by switching gas in a sealed environment or changing temperature.

2.3.2 Distribution of Relaxation Times (DRT)

EIS is a power technique used to probe electrochemical reactions occurring at different time constants using complex and real impedance. EIS results are usually modeled by equivalent circuits which are subjective to the person reviewing the EIS result, thus leaving room for error. Distribution of relaxation times (DRT) analysis converts complex impedance data as a function of frequencies or time constants. [42,43] These time constants further elucidate impedance by showing the data as peaks as a function revealing the characteristic frequency or time constant for a physical process.

The theory of the DRT conversion is as follows. Impedance data is fit with a finite Voigt circuit shown in the equation below:

$$Z(\omega) = \sum_{k=1}^{N} \frac{R_k}{1 + i\omega\tau_k} \qquad [2.1]$$

In this equation Z(ω) is the impedance, with a series of N RC circuits that have a characteristic time constant of $\tau_k = R_k C_k$. R is the resistance and C is the capacitance in the Voigt circuit. A Voigt circuit is the impedance measurement model that models impedance data around R/C circuit elements. The Voigt circuit that is then modeled around the data points in an impedance set to fit a R_k/C_k and for each data point a time constant can be calculated. The R_k vs τ plot relatively follows a gaussian law in that all

of the fitted resistance points as a function of time constant sum to the total value of the real impedance for the given circuit.

$$\sum_{k=1}^{N} R_k \approx Z_{max} \quad [2.2]$$

These equations fit the data and can calculate the DRT for a simple model in which the impedance is known. There is a second scenario that can calculate the DRT for a given model system that parameters of the circuit are known. The infinite Voigt circuit models the DRT (G(τ)) as a continuous function instead of discrete variables as in the first scenario. The equation below shows the impedance of the infinite Voigt circuit below in equation 2.3:

$$Z(\omega) = \int_0^{\infty} \frac{G(\tau)}{1 + i\omega\tau} d\tau \quad [2.3]$$

This works for a scenario that the impedance Z(ω) is known and now the DRT (G(τ)) of the infinite Voigt circuit is:

$$G_{R/Q}(\tau) = \frac{R}{2\pi} \frac{sin(1-\alpha)\pi}{cosh\left(\alpha ln\left\{\frac{\tau}{\tau_{R/Q}}\right\}\right) - cos\big((1-\alpha)\pi\big)} \quad [2.4]$$

The challenge with using this equation is that from the impedance measurement the parameters α, Q, and R are unknown unless fitted. These parameters are also difficult to derive from a complex electrochemical system with multi-reaction steps. Each of these data sets could also have multiple arcs fit within the Voigt circuit. The DRTtools package developed by the Ciucci group uses a numerical method to solve for the DRT using the given impedance data. [43] This method gives the complex system a spectrum of peaks by calculating the DRT from the analytical method and is widely regarded in the field as the standard for computing the DRT from impedance data. Once the DRT

spectrum is calculated these peaks can be fit to derive a physical meaning. For example, the DRT could show a peak at the time constant of 10^{-3} s and this peak is thought to correspond to the surface reactions in an SOFC cathode if probing a symmetric cell. [44] The DRT can elucidate how the cathode surface reactions degrade over time if the DRT is computed for impedance spectra as a function of time and the peak with the time constant τ is evolved. DRT is a very powerful tool that can show a clear picture of how a specific reaction evolves given changing experimental conditions. In this work a modified python script was developed to use the functions in DRTtools to run the functions batch wise. However, the python script has a few differences that should be considered. First, the python script developed only considers a gaussian type peak for each peak, DRTtools has multiple shape peak settings. Second, the python script uses a different algorithm for its numerical integration and the integral is calculated using the alternating direction method of multipliers (ADMM). The MATLAB script calculates the integral by interior point convex algorithm. Mathematically both integrals are calculated to solve the DRT.[43] The python script shows the contribution due to the inductance whereas the DRTtools takes it out. These slight differences could contribute to marginal differences in the peak shape and size of the peaks in the DRT spectra.

An example of what information one can get from the Nyquist and DRT plot is shown below in Figure 2.6 for an SSC-GDC symmetric cell tested in air at 650 °C. The Nyquist is shown in A with labeled decade frequency points, while the corresponding DRT curve is shown in B. The frequency points in A are the inverse of the time constant calculated in B. The Nyquist plot reveals that there could be multiple arcs fit to the

impedance spectra. The apparent overall reaction characteristic frequency is 100 Hz where the most impedance losses are expected. However, this is a multistep reaction that is occurring and the DRT further deconvolutes the time constants of the specific peaks that contribute to the most impedance losses. The peak at 10^{-4} (s) corresponds to a 10^{4} (Hz) frequency which is not shown in the Nyquist as is it is in the ohmic regime not revealing relevant information for the electrode reaction. It may still be important to show for purposes relating the electrolyte-electrode charge transfer process.

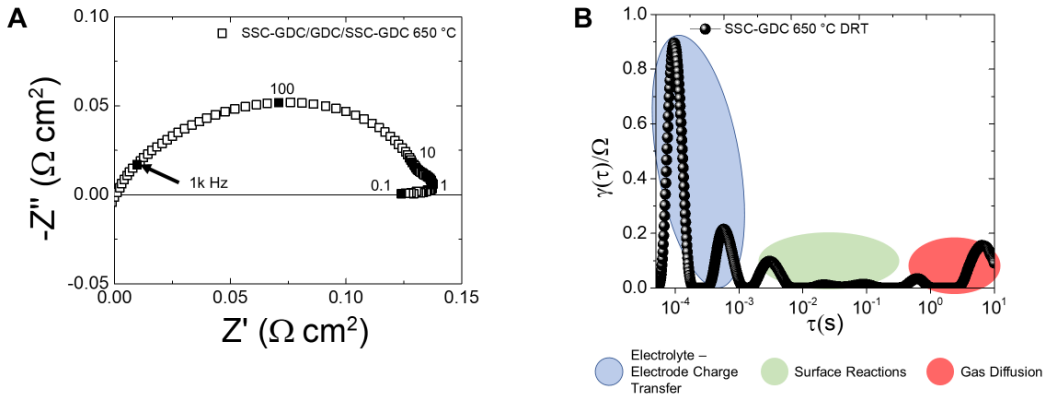

Figure 2.6 A. Nyquist Plot and B. Corresponding Calculated DRT Curve for SSC-GDC/GDC/SSC-GDC Symmetric Cell tested in air at 650 °C

2.3.3 Full Cell Testing on Button Cells

To further study SOFC electrodes, it is important to implement the modified electrodes on the full cell level to observe how the device behaves. Popular methods to test new electrodes are to implement them onto either electrolyte supported cells or onto conventional anode supported cells. Electrolyte supported cells are a good tool to screen alternative anodes as the mechanical properties, CTE, and electrical aging properties are not yet understood. Comparing a new anode material with the traditional anode material is facile as it consists of making an anode ink of the new anode and the conventional anode and comparing the performance on an electrolyte supported cell;

then the anode material could be characterized in depth. However, anode material studies are not the subject of this work and are only to be used as an example for how to study anodes. Studying new cathode materials can be done on either electrolyte or anode supported button cells. It is actually more efficient to study cathode materials on an anode supported button cell to see how the device would operate when all components are fully integrated. A button cell is a scaled down version of a full format SOFC, and is typically <2" in size. As the total power output of an SOFC is scaled linearly with total active area, it becomes wasteful to understand basic device operation on a cell much larger than that since performance is normalized to the overall active area in either case.

Characterizing the full cell requires the consideration of three key measurements. First EIS is performed to understand the total resistance or impedance of the cell, ranging from both electrodes in the case of the non-ohmic and ohmic polarization which is mainly due to the electrolyte. Impedance was covered in a previous section, so the same principles apply to full cell testing as they do to symmetric cells. The next measurement is the current-voltage, or iV behavior measurement, as explained above. The iV behavior is important to understand how the fuel cell reaction operates. The voltage behavior is governed by three dominant regimes: activation polarization, ohmic polarization, and concentration polarization. Activation polarization is the energy required to start the reaction or activation barrier, it is not typically seen in SOFC reactions and is more of a phenomenon seen in PEM fuel cells. Next is ohmic polarization which depends on the resistance of the cell, and responds as ohm's law, V=IR as there is more current drawn from the cell and the resistance stays

the same but the voltage continues to drop. Once the voltage drop in the fuel cell is nonlinear, the third polarization is concentration polarization. As the reaction occurs at a higher rate (e.g., more current) there become mass diffusion limitations in each electrode. Concentration polarization typically is not material property dependent and is more of a microstructural limitation in the electrodes although some results do claim it could have a material property dependence.[44] Measuring the iV behavior can be done by two measurements, either galvanodynamic which applies a current in a stepwise fashion and measures the voltage or potentiodynamic which applies a voltage and measures a current. Both methods can correctly measure the iV of a SOFC and were used in this work but did not produce discernible differences.

A sample iV and impedance curve can be seen below in Figure 2.7. The cell has an LSCF-GDC cathode (~20 μm thick), GDC electrolyte (~20 μm thick), Ni-GDC anode functional layer (~20 μm thick), and Ni-GDC anode support (500 μm thick). The power density curve is calculated from the iV curve as P=IV and is shown on the axis on the right for each described temperature. From these curves the OCV is about 0.8 V at each temperature which is lower than the theoretical voltage of about 1.1 V. The lower than theoretical OCV could be due to multiple factors, first the oxygen ion transference number of the GDC electrolyte is lower than 1, t_{O2-} ~ 0.8 in this temperature range. The equation for OCV as a function of transference number can be seen below where V_{th} is the theoretical OCV from equation 1.1 and t_{O2-} is the oxygen ion transference number from equation 1.2:

$$OCV = V_{th} t_{O_{2-}} \quad [2.5]$$

Second, the cell electrolyte could have pinholes that would allow small amounts of oxygen to transport to the anode side, thus lowering the pO_2 gradient across the cell and lowering the OCV. Third, OCV in MIEC electrolytes can be dependent on the oxygen activity of the cathode, driving up the local pO_2 at the cathode-electrolyte interface, a theory reported in literature. LSCF-GDC is not a highly active cathode in this temperature range so that could be evidence for the third fact, but more experiments would be required to further elucidate this mechanism.

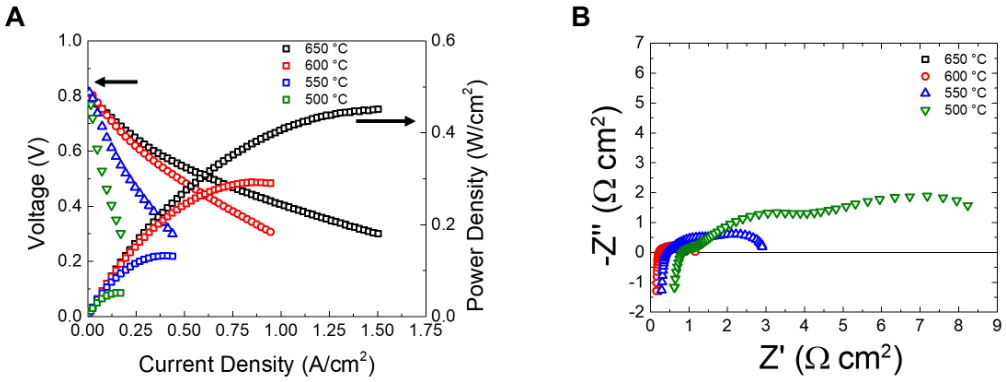

Figure 2.7 Current-Voltage and Impedance Behavior for LSCF-GDC/GDC/Ni-GDC Full Cell. A) iV curve for the described cell in 97% H_2/3% H_2O bubbled through water; the inverse parabolic curve corresponds to the axis on the right which is the power density. The semi-linear curves correspond to the voltage axis on the left. Galvanodynamic measurements were taken at 4 different temperatures of interest. **B**) Nyquist plot for the cell described above taken at 4 different temperatures.

The third and final measurement used to characterize an SOFC would be to see how the cell operates under an applied current or voltage. Two types of measurements could be used to study how the cell operates under current. The first measurement is a potentiostatic measurement, in which a constant voltage is applied to the cell, as well as either the reference or OCV, and the current is measured. The other measurement is a galvanostatic measurement, in which the cell is placed on a constant current and the

voltage is measured. The main difference between the two is that in a potentiostatic measurement the voltage is fixed and the goal is to see how fast the full cell reactions occur because the current quantifies how much electricity is generated. On the other hand, the galvanostatic measurement fixes the current, or the reaction rate, and observes the voltage because the current is directly related to the SOFC reaction. For the purposes of this work, the majority of the cells were operated under a galvanostatic measurement for 5 hours with iV and impedance behavior recorded in between runs. A sample voltage vs time curve can be seen below in Figure 2.8 for the LSCF-GDC/GDC/Ni-GDC cell described in Figure 2.7.

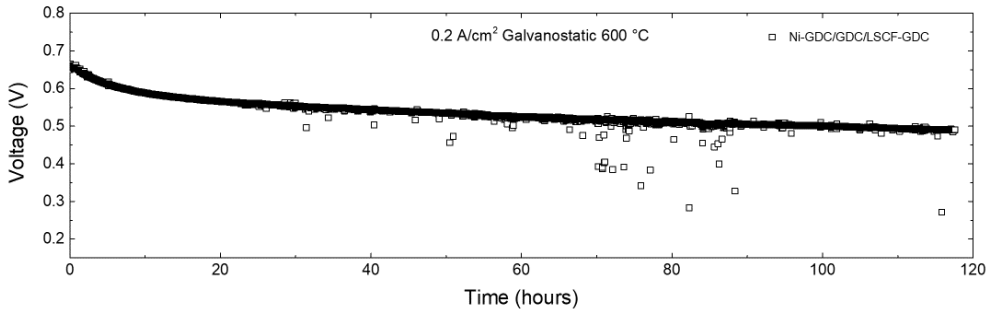

Figure 2.8 Voltage vs Time for an LSCF-GDC/GDC/Ni-GDC full cell operating on 97%H_2/3%H_2O under a galvanostatic hold.

The button cell test fixture consists of a few parts shown in the diagram of the text fixture in Figure 2.9. First, the cell is mounted to an open-ended single-bore alumina tube (Advalue tech) with one side for gas delivery and the other to mount the cell. Silver current collector paste (fuel cell materials), mesh (unique wire weaving company), and wires (Rio Grande) are then attached to each electrode of the cell and dried to establish a strong electrical contact. The current collector wires are then attached to external current collector wires attached to the exterior of the alumina tube. After the cell is secured to the test fixture, a 2-part ceramic seal is applied to the cell to

seal the anode gas from the cathode gas (Ceramabond, Aremco). The seal is then dried at room temperature in air before curing in the furnace. The cell is placed in the furnace and attached to current collector leads that are connected to the potentiostat/FRA (Solartron 1470E). The cell seal is then cured after heating in the furnace (Mellen, Carbolyte) to the desired operating temperature. The operating temperature is monitored by a thermocouple placed directly next to the cell and externally monitored with a thermocouple reader. All Ni-GDC anode supported cells were first taken to 650 °C and were flown N_2 as an inert gas to purge the system of oxygen before delivering hydrogen to the cell. The cell was then flown hydrogen from mass flow controllers (Unit Instruments/MKS) for 1-2 hours after a 5-minute mixture of H_2/N_2 to reduce the Ni in the Ni-GDC anode. After the anode has been reduced the cell, which is monitored by EIS, EIS and iV measurements was taken over a range of temperatures in 50 °C intervals. After the temperature sweeps are performed each cell is aged under its respective operating condition.

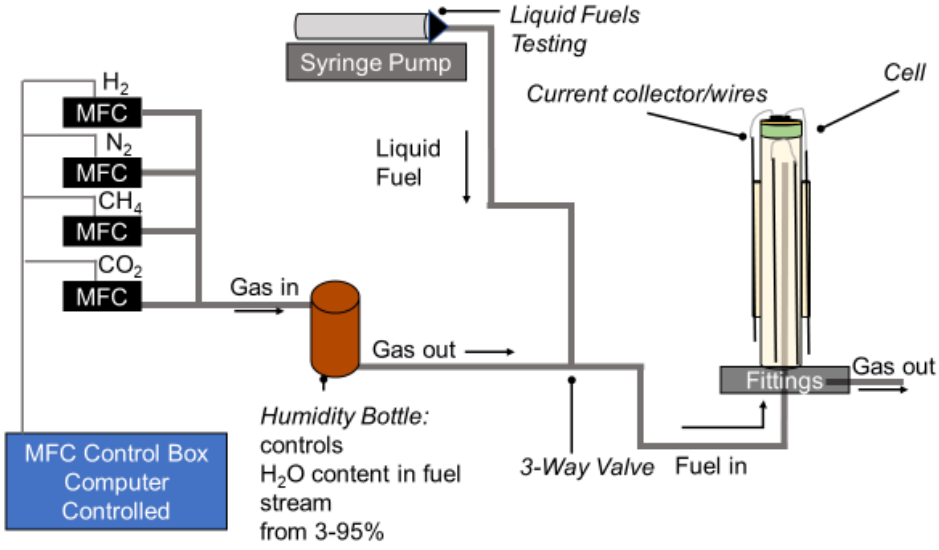

Figure 2.9 Button Cell Testing System. Mass flow controllers are controlled by a external microcontroller and python scripts to deliver gas through a humidity bottle that can control the steam content in the gas mixture. Syringe pump is used for the testing of liquid fuels. Swagelok fittings are attached to an alumina tube with an internal alumina tube placed ~5mm from the cell, feeding gas directly to the cell. External current collector wires are used to electrically connect to the Potentiostat/FRA.

Chapter 3. Enhancement of Low-Temperature Solid Oxide Fuel Cell Performance and Durability via Surface Chemistry Modification

3.1 Introduction

Surface modification (SM) of a prefabricated sintered ceramic scaffold is a promising strategy to enhance cathode activity. This post-decoration technique introduces additional electro-catalysts after the necessary high-temperature SOFC sintering process, thus avoiding high-temperature ceramic processing (1400~1500°C) issues such as thermal expansion mismatch, dopant segregation, side reactions, inter-diffusion, and coarsening. Among all surface modification methods, solution-based infiltration is one of the most attractive approaches because of its low-cost, simplicity, and scalability.[21,22,45,46] The dissolved cations in the liquid phase can easily penetrate the porous electrode scaffold and then form active electro-catalyst phases that homogeneously distribute in the cathode after calcination. In addition to catalytic activity, in some circumstances, surface modification has been shown to enhance the long-term electrode stability.[23] Thus, for SOFC cathodes, the ORR, durability, and mixed ionic electronic conductivity (MIEC) are considered to be the most important properties. Since MIEC is determined by the cathode bulk provided by the scaffold, gas-solid reactivity is much more sensitive to the surface chemistry/structure. Thus, surface modification is particularly important because the cathode surface chemistry determines the efficiency and stability of gas-solid reactions.[23,47,48]

Praseodymium (Pr) is a popular element for cathodes because of its multivalent character. The changes of Pr oxidation states are compensated by oxygen vacancy generation in $PrO_{2-\delta}$ where δ represents oxygen nonstoichiometry. These oxygen vacancies tend to arrange in different degrees of ordering, resulting in multiple super lattice phases.[41,49] PrO_x alone can function as cathode because of its electronic conductivity and catalytic activity.[50,51] Also, it is shown that the addition of Pr on cathodes, including LSCF, $La_{0.6}Ni_{0.4}FeO_3$, $PrNi_{0.5}Mn_{0.5}O_3$, and $SrTi_{0.3}Fe_{0.55}Co_{0.15}O_{3-\delta}$, improves the cathode performance.[10,52–54] Moreover, the cathodes that contain the element Pr are shown to be active towards the ORR kinetics. For instance, Pr in $PrBa_{0.5}Sr_{0.5}Co_{1.5}Fe_{0.5}O_{5+\delta}$ (PBSCF) is believed to facilitate oxygen activity.[10,52] Although Pr has been shown to improve the ORR kinetics by itself, the exact role of PrO_x as an additive, or in the compounds, is still unclear.

Here we demonstrate that adding multi-valent cations, particularly praseodymium, considerably modifies the cathode surface chemistry, and the performance and the durability are significantly enhanced once the surface is activated. $Sr_{0.5}Sm_{0.5}CoO_{3-\delta}$-$Gd_{0.1}Ce_{0.9}O_{2-\delta}$ (SSC-GDC) is selected as the cathode backbone for surface modification because it is a relatively stable and high-performing SOFC cathode, compared to other common cathodes, such as $La_{0.6}Sr_{0.4}Co_{0.2}Fe_{0.8}O_3$ (LSCF), $La_{0.8}Sr_{0.2}MnO_3$ (LSM), $Ba_{0.5}Sr_{0.5}Co_{0.8}Fe_{0.2}O_{3-\delta}$ (BSCF), and $PrBa_{0.5}Sr_{0.5}Co_{1.5}Fe_{0.5}O_{5+\delta}$ (PBSCF). By carefully selecting infiltrated electro-catalysts and tuning the calcination temperature, cathode performance can be enhanced without compromising durability. Using spatial resolved and *in situ* temperature programmed characterization, we elucidated the active phase at the PrO_x-SSC-GDC interface and determined the

synergistic effects of the PrO_x modified surface. We show that the modification of the cathode surface chemistry, after the high-temperature cell fabrication processes, can effectively enhance the gas-solid interaction activity and durability. We also demonstrated that such performance and durability enhancement due to this modification is valid not only to SSC cathodes but also to other cathodes such as LSCF (see Figure 3.9 and Figure 3.12).

3.2 Results and Discussion

Cathode electrochemical activity was determined using a symmetric cell configuration. We screened over a wide selection of infiltrates (Pr, Fe, Co, Cu, Ag, Dy, and Nd), and the electrochemical performance of these single element infiltrated SSC-GDC is shown in Figure 3.1 A. Out of these infiltrates, only Pr and Dy infiltrated cells lowered the impedance while other infiltrates increased the polarization impedance. Comparing results of Pr and Dy infiltrated cells, Pr showed the most reduction in polarization resistance by almost an order of magnitude. Nyquist plots of PrO_x modified SSC-GDC (Pr-SM) cathodes (circle open symbols) at 600, 550, and 500°C are shown in Figure 3.1 A-C, respectively, and the unmodified SSC-GDC (square open symbols) is shown for comparison. The presence of PrO_x significantly decreased electrode polarization loss from ~0.30 to 0.05 Ωcm^2, from 0.74 to 0.14 Ωcm^2, and from 1.97 to 0.44 Ωcm^2 at 600, 550, and 500 °C, respectively.

The electrochemical performance of a Pr-SM cathode as compared to other common cathodes is summarized in Arrhenius plot in Figure 3.1 D. Compared to the unmodified cell (square symbols), the Pr-SM cell (star symbols) reduce ASR by about one order of magnitude over all tested temperatures with changes in apparent activation

energy from 1.07 eV to 1.20 eV. The ASR of the Pr-SM is much lower than most reported cathodes and is comparable to the state of the art SOFC cathode, PBSCF. These results demonstrate that PrO_x surface modification significantly enhances the cathode electrochemical performance.

To determine the role of PrO_x on a cathode, distribution of relaxation time (DRT) analysis was used to deconvolute multiple cathode reaction processes. Figure 3.1 E shows the DRT results of both Pr-SM and unmodified (No SM) SSC-GDC cells at 600, 550, and 500 °C. The low time constant region, highlighted in dark blue, is typically attributed to the solid-solid transport between electrolyte and electrode.[47,55,56] The intermediate time constant region (green) and the low time constant region (purple) represents surface processes and gas diffusion, respectively.[55] For the unmodified cell (black symbols), the peaks in the surface exchange region show the highest intensity, suggesting that surface exchange processes contribute the most to impedance losses, which is also consistent with the rate limiting step of SSC, as suggested by Fukunaga et al..[57] For the Pr-SM cell (red), the peaks in the surface exchange region are significantly reduced, indicating that the presence of PrO_x on SSC-GDC significantly enhanced the surface exchange kinetics, possibly during the surface oxygen dissociative adsorption step.

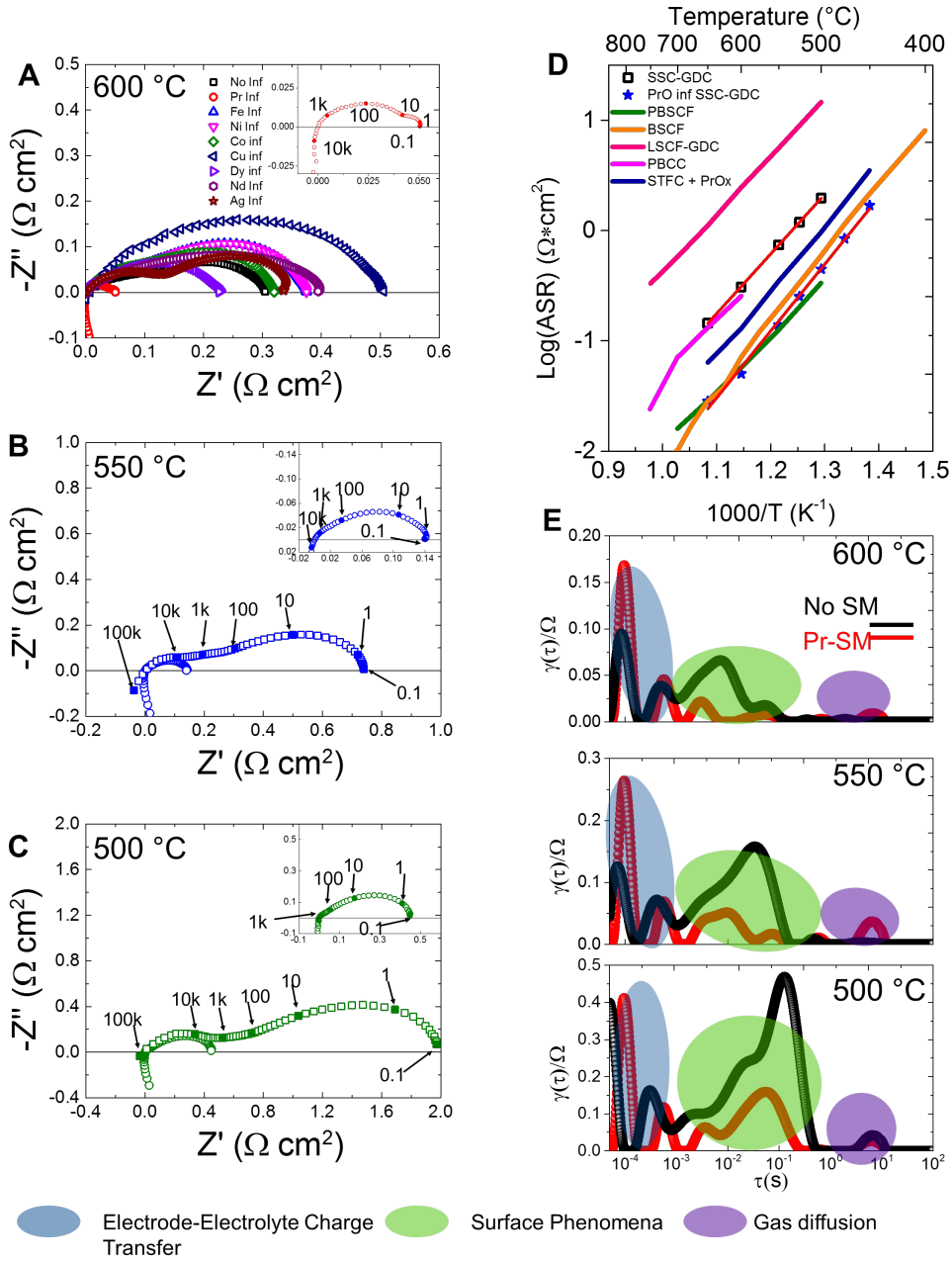

Figure 3.1 Electrochemical performance of modified cathodes. Nyquist plot of Pr SM and unmodified symmetric cells at (**A**) 600 °C with other cation infiltrates (Fe, Ni, Co, Cu, Dy, Nd, Ag), (**B**) 550, and (**C**) 500 °C with corresponding (**D**) Arrhenius plot and (**E**) DRT analysis. The decade frequencies are highlighted. The ASR of common cathodes are shown in Arrhenius plot for comparison: $La_{0.6}Sr_{0.4}Co_{0.2}Fe_{0.8}O_{3-\delta}$-GDC (LSCF-GDC), $PrBa_{0.5}Sr_{0.5}Co_{1.5}Fe_{0.5}O_{5+\delta}$ (PBSCF)[58], $Ba_{0.5}Sr_{0.5}Co_{0.8}Fe_{0.2}O_{3-\delta}$ (BSCF)[7], $PrBa_{0.8}Ca_{0.2}Co_2O_{5+\delta}$ (PBCC)[56], and $SrTi_{0.3}Fe_{0.55}Co_{0.15}O_{3-\delta}$ + PrO_x.[53]

The durability of the modified cathode was also determined using the symmetric cell configuration in synthetic air for over 2000 hours at 600 °C. Figure 3.2

A and B show Nyquist plots of the aging processes of the unmodified and Pr-SM SSC-GDC, respectively. After 2000 hours, the ASR of the unmodified SSC-GDC increases from 0.34 to 0.63 Ωcm^2 while that of Pr-SM starts at only 0.05 Ωcm^2 and increases to only 0.20 Ωcm^2. In both cases, the majority increase in ASR can be attributed to the low frequency arc, while the high frequency arc of the unmodified cell shows an additional degradation process.

The detailed changes can be better seen in the corresponding DRT analysis in Figure 3.2 C and D. The degradation of the unmodified cell happens in both electrode-electrolyte charge transfer region and surface reaction regions in Figure 3.2 C. In contrast, the degradation process for Pr-SM (Figure 3.2D) is only observed in the intermediate constant region, and the devastating degradation in electrode-electrolyte charge transfer region does not appear in the Pr-SM cathode even after 2000 hours of testing, suggesting that the SSC-GDC surface is stabilized by introducing PrO_x. Figure 3.2 E summarizes the ASR changes as a function of aging time. The unmodified SSC-GDC has a drastic increase in ASR over the first 100 hours from 0.30 to over 0.50 Ωcm^2. Pr-SM has a lower degradation rate at the first 100 hours, possibly due to the slight agglomeration of PrO_x nanoparticles that decreases the surface activity (see the increase in surface exchange region in Figure 3.2 D). After 1000 hours, this degradation process stops, and the ASR of Pr-SM, reaches a plateau with a low ASR of 0.2 Ωcm^2 even after 2000 hours of aging. SEM images of the aged cathodes are shown in Figure 3.2 E. The porosity of the SSC-GDC cathode and Pr-SM cathode is very similar, indicating that the microstructure is maintained and coarsening is not the predominant degradation issue in either case. This can easily be seen in the right inset of Figure 3.2

E where the small fuzzy particles are still on the order of nanometers (~10nm diameter) after 2000 hours of aging.

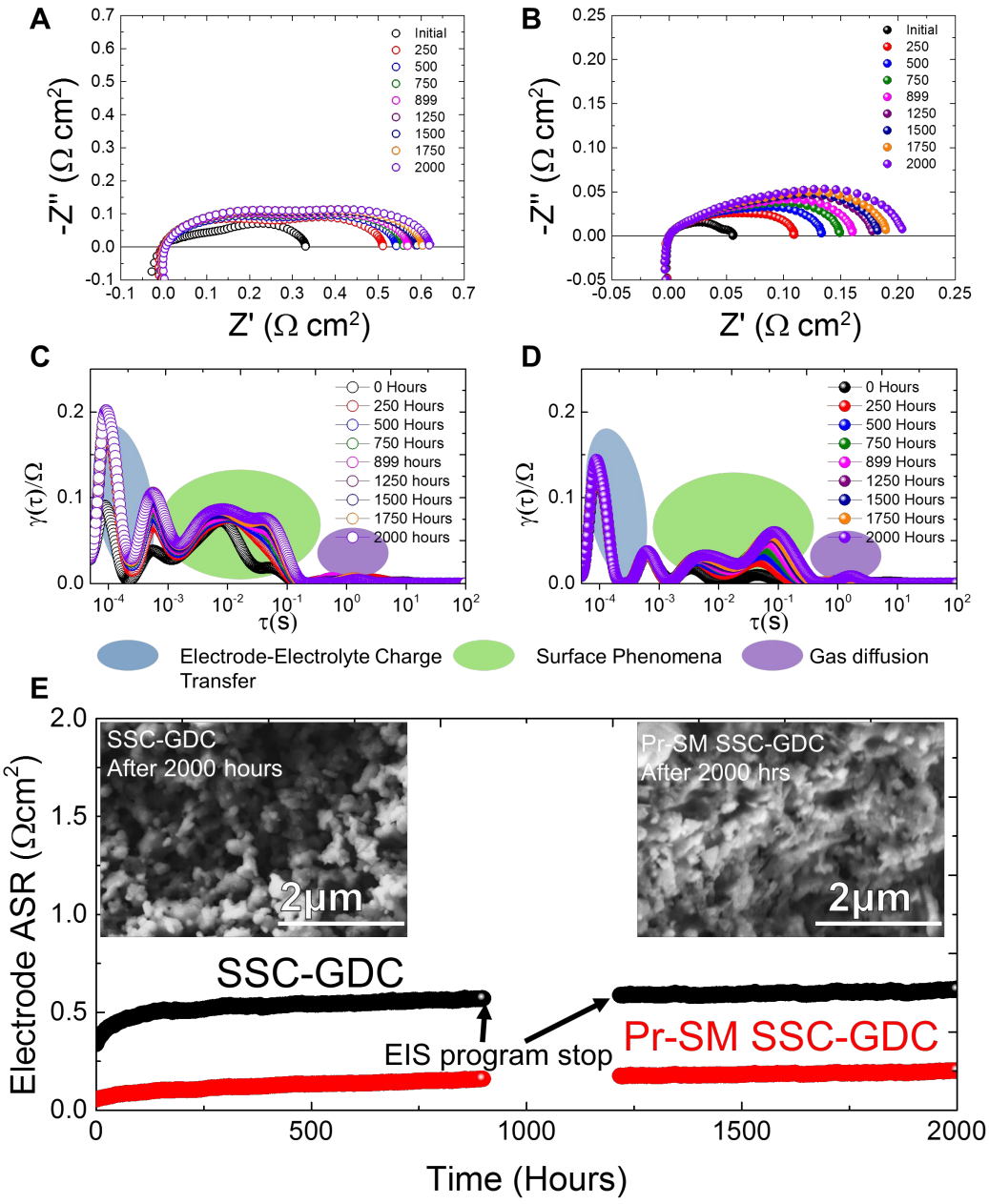

Figure 3.2 Nyquist plots of symmetric cell aging at 600 °C for (**A**) unmodified and (**B**) PrO_x surface modified SSC-GDC with the corresponding DRT plots elucidating the mechanism of degradation of (**C**) unmodified and (**D**) PrO_x surface modified SSC-GDC, respectively. (**E**) symmetric cell aging for 2000 hours for SSC-GDC (left) and PrO_x surface modified SSC-GDC (right) with corresponding post aging SEM images.

CO_2, an inevitable component in air, is known to preferably bond to the surface of perovskites and induce degradation mechanisms such as blocking effects (reversible process) and cation segregation (irreversible material decomposition). [27,29,59,60] To determine the CO_2 tolerance enhancement by surface modification, the impedance changes as a function of CO_2 partial pressure (pCO_2) as well as aging results with the presence of CO_2 were measured. Figure 3.3 A and B show the EIS results for CO_2 partial pressure (pCO_2) dependence at 600 °C with corresponding DRT analysis for Pr-SM and unmodified SSC-GDC (Figure 3 C and D). The presence of CO_2 strongly affects the ASR in both cases.

Using DRT, we further deconvoluted the effects of CO_2 on each electrode process. Corresponding DRT in Figure 3.3 C and D indicate that the surface phenomena and gas diffusion regimes contribute the most to energy loss both for modified and unmodified cells. In addition, the strong CO_2 dependence on impedance losses is also observed in this regime. This suggests that CO_2 actively participates in the surface exchange process as a result of competitive adsorption between CO_2 and O_2 molecules for the active sites.

To identify these short-term CO_2-O_2 competitive effects, the pCO_2 dependence on the dominant regime (surface reaction) was studied. The area of DRT peaks in this regime were integrated as they represent the total energy loss in this process, and the total changes as a function of pCO_2 are shown in the double logarithmic plot in Figure 3.3 E. The Pr modified cell had a lower impedance over the unmodified cell in all tested pCO_2, and a linear correlation is observed with a slope of 1/6 and 1/4 for the unmodified and modified cell, respectively. This change in slope indicates that the presence of PrO_x

alters the cathode surface, and at high pCO_2, CO_2 molecules prefer to occupy the active sites of the modified surface because of competitive adsorption. It also suggests that in the ambient air with ppm levels of CO_2, the CO_2 tolerance of Pr-SM cell is superior to the unmodified one, and the modified cell should be relatively stable in realistic working conditions.

The long-term CO_2 effects are summarized in Figure 3.3 F and G. The accelerated aging results with 1% CO_2 are shown in Nyquist plot (Figure 3.3 F). For the unmodified cell, the presence of CO_2 increases the impedance immediately, and only one hour of aging further increases the impedance from 0.75 to 1 $\Omega \cdot cm^2$. In contrast, the Pr modified cell does not show any significant degradation in the first several hours, suggesting that the Pr modified surface prevents the rapid CO_2 degradation observed on SSC-GDC. The long-term aging results are shown in Figure 3.3 G. For the unmodified SSC-GDC, the ASR saturates at a value of approximately 1 Ωcm^2 after initial degradation. Note that the degradation that occurs in the first hour for SSC-GDC is not seen in the Pr-SM SSC-GDC. Pr-SM SSC-GDC shows high stability in CO_2 and the ASR reaches a plateau value of 0.4 $\Omega \cdot cm^2$ at 600 °C. The long-term accelerated testing results demonstrate the CO_2 tolerance enhancement of Pr-SM SSC-GDC.

.....

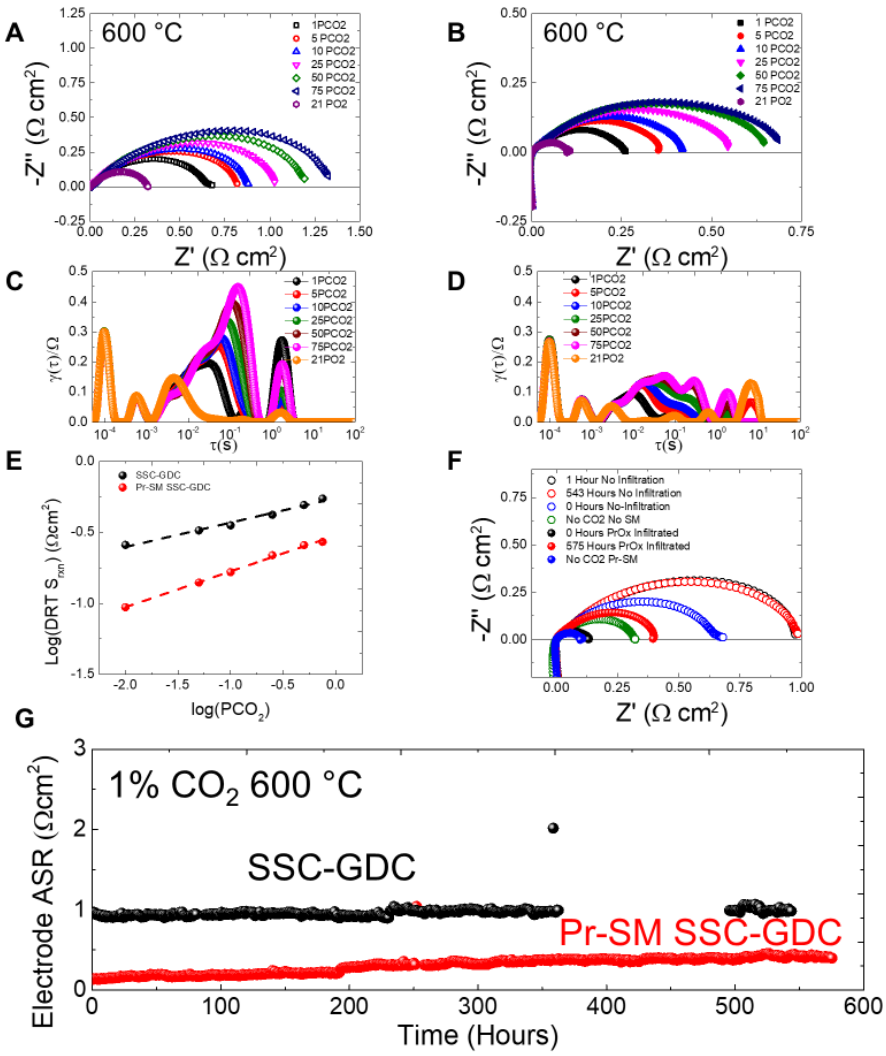

Figure 3.3 CO_2 Tolerance of SSC-GDC and Pr-SM SSC-GDC. Nyquist plots showing the CO_2 dependence on (**A**) SSC-GDC and (**B**) Pr-SM SSC-GDC, respectively. The pO_2 was fixed at 21 %, and the pCO_2 was controlled by changing the flow rate of CO_2 and N_2. Numbers in legend indicate percentage of CO_2 and "21 PO2" indicates 0% CO_2. DRT analysis of CO_2 dependence derived from the Nyquist plots of (**C**) SSC-GDC and (**D**) Pr-SM. (**E**) Double log plot of DRT curve area versus pCO_2. (**F**) Nyquist plots of SSC-GDC and Pr-SM during aging. (**G**) The long-term accelerated aging results in 1% CO_2 at 600 °C for over 500 hours.

To identify the activity of PrO_x, *in situ* temperature programmed experiments were conducted on PrO_x powders. Temperature programmed oxidation (TPO) of PrO_x infiltration solution is shown in Figure 3.4 A. In TPO, the dried powders were heated up to 650 °C in O_2 under a fixed ramp rate (30 °C/min), and the *m/z* signals of evolved

gas compounds were recorded using the downstream mass spectroscopy. CO (*m/z*=28) and CO_2 (*m/z*= 44) decompose at a lower temperature (100~500 °C), and NO (*m/z*=30) and NO_2 (*m/z*=46) show up at a higher temperature (350~650 °C). This TPO results suggest that the Pr nitrate solution completely decomposed around 650 °C. Figure 3.4 B shows TPD of PrO_x powders that was pretreated at 650 (black) or 800 (red) °C. Four main desorption peaks are observed as a result of the changes in Pr oxidation states, consistent with results from Takasu et al.[61] In addition, the pretreatment temperature directly changes the desorption peak temperature and intensity. The desorption peaks of the PrO_x pretreated at 650 °C shift to a lower temperature with higher intensity, suggesting that PrO_x has higher oxygen activity and contains a larger number of oxygen vacancies in the lattice than the PrO_x pretreated at 800 °C.

According to the Pr-O phase diagram, PrO_x has multiple phases with different oxygen vacancy ordered structures in the SOFC operating temperature regime, ranging from PrO_2 to PrO with numerous intermediate structures with varied Pr oxidation states, Pr^{2+}, Pr^{3+}, and Pr^{4+}. To determine the temperature effects on chemical states of PrO_x, *in situ* TEM was performed on PrO_x powders that were pretreated at 650 °C, the optimized temperature from the TPO results. The high-resolution transmission electron microscopy (HR-TEM) image of PrO_x at 800 °C is shown in Figure 3.4 C. The lattice fringe of the crystalline PrO_x can be clearly seen even at 800 °C. The electron diffraction patterns of PrO_x at 23 (room temperature), 400 and 800 °C are shown in Figure 3.4 D. PrO_x at different temperatures has a similar diffraction pattern with a slight change in spacing, suggesting that the lattice expands as the temperature increases. The increase in the numbers of diffraction spots at high temperatures is

caused by the temperature disturbance. The changes in PrO_x lattice constant are summarized in Figure 3.4 F. The PrO_x lattice expands over 2.5% from room temperature to 600 °C because the oxygen loss at high temperature is compensated by the changes in Pr oxidation states. This suggests that the active changes in oxygen states of Pr are responsible for the high activity of PrO_x.

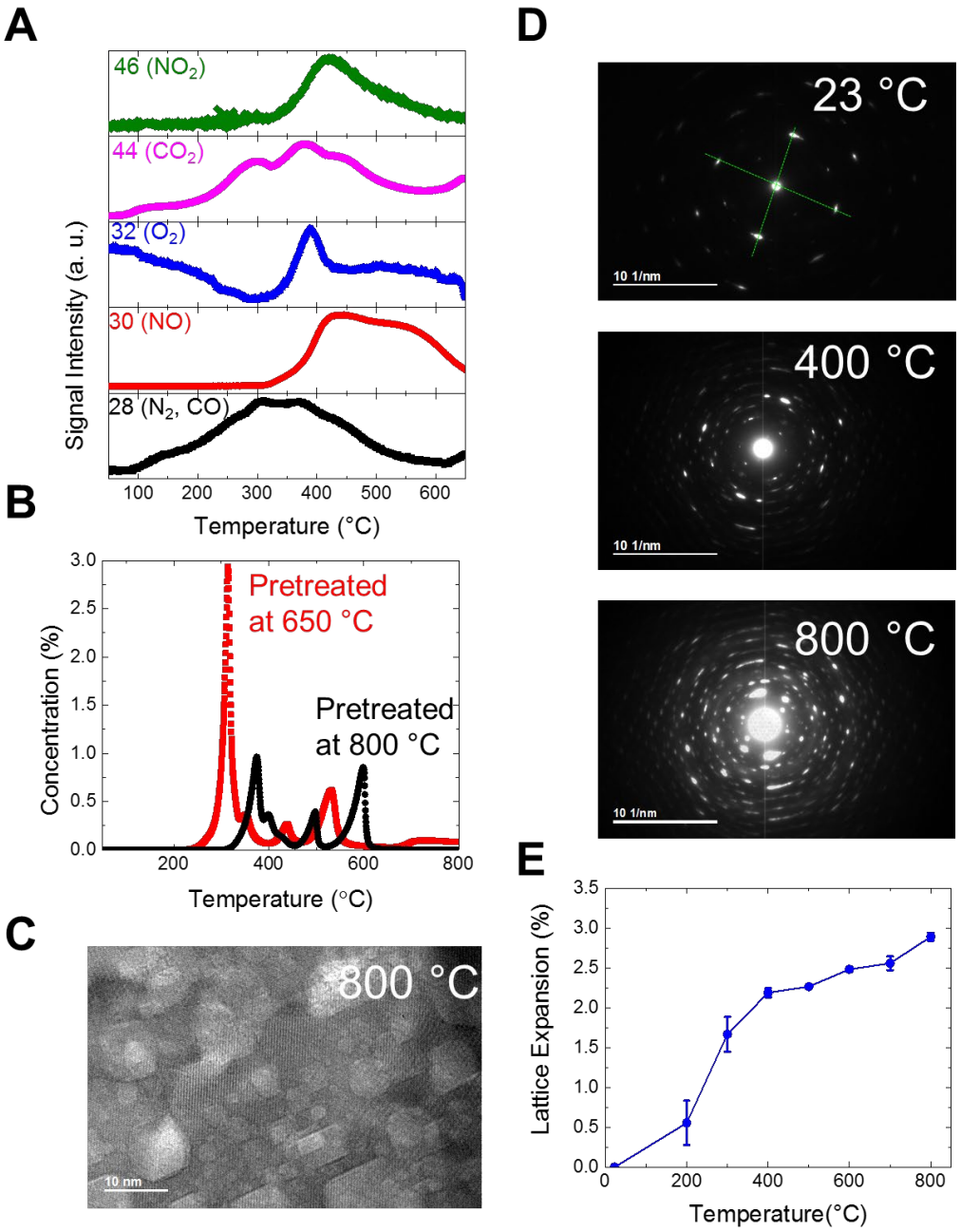

Figure 3.4 Temperature Dependence on *in-situ* Characterization of PrO_x Stoichiometry and Structure. (**A**) TPO of PrO_x infiltration nitrate solution. The *m/z* ratio of the mass spectroscopy signal and the corresponding compounds are labelled in the figure. (**B**) TPD of PrO_x that was pretreated at 650 °C (red) or 800 °C (black). (**C**) HR-TEM of PrO_x at 800 °C. (**D**) Electron diffraction patterns at 23 (room temperature), 400, and 800 °C, and (**E**) The average lattice constant changes of PrO_x as a function of temperature based on the temperature dependent electron diffraction patterns. Error bars are provided, and for some data points, the error bar is smaller than the symbol size.

The surface structure and chemistry at the PrO/GDC and SSC/GDC interface were studied using TEM, as shown in Figure 3.5 and Figure 3.6, respectively. High-resolution TEM (HR-TEM) image of PrO_x on GDC is shown in Figure 3.5 A. The PrO_x has an average particle size of 3~5 nm with crystalline structure. Figure 3.5 B shows high-angle annular dark-field (HAADF) of the PrO_x-GDC interface and the corresponding Energy-dispersive X-ray spectroscopy (EDS) elemental mapping. Red and green represent Pr and Ce, respectively, showing that PrO_x coverage on the GDC backbone.

The EELS line scan (green line in Figure 3.5 A) is shown in the contour plot in Figure 3.5 C where X is the energy loss, Y is the distance from the original point, and color map represents the intensity of peaks. The relative intensity changes in Pr M edge (~950 eV) and Ce M edge (~900eV) characteristic peaks can be seen across the PrO_x-GDC interface. At the interface, highlighted in the area in the white box, Pr signals drop and the Ce signals rise, and the detail spectra changes of each peak are shown in Figure 3.5 D. It seems that at the interface, a Pr-Ce-O solid solution phase is formed. In addition, the Pr M edge peaks shift as a function of the depth (see the black line and black dash line in Figure 3.5 D), suggesting that the oxidation states of Pr changes at the PrO_x/GDC interface.[62]

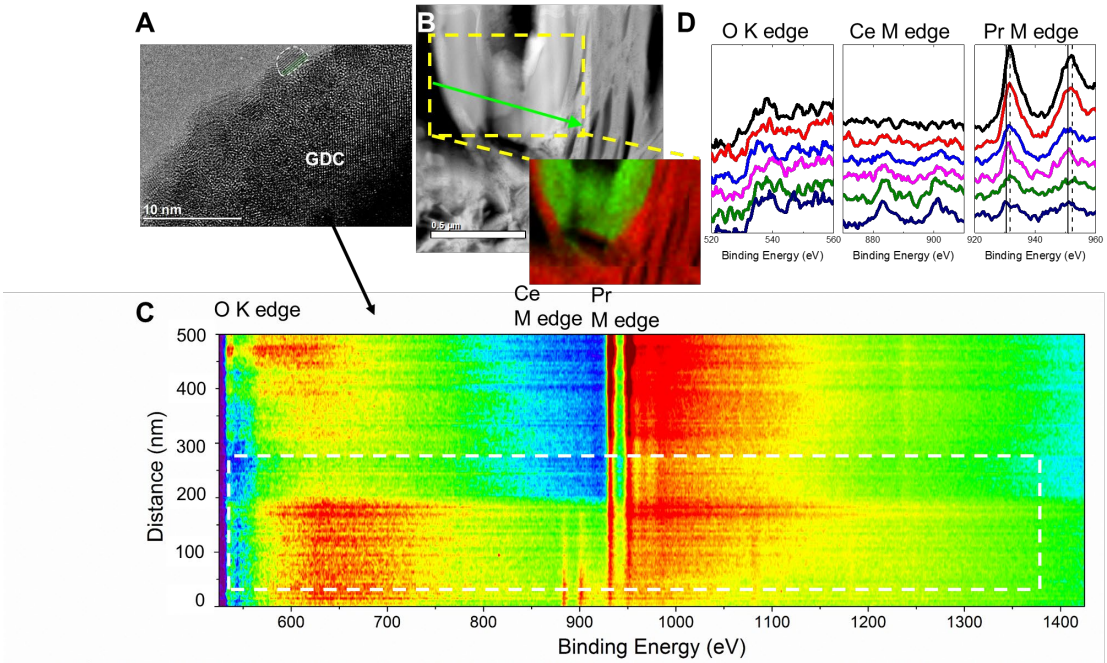

Figure 3.5 Surface Chemistry Analysis at the PrO_x-GDC Interfaces. (**A**) HAADF of PrO_x-GDC. (**B**). EDS color mapping where red represents Pr and green indicates Ce. (**C**) EELS spectra across PrO_x-GDC interfaces, and the corresponding (**D**) O K edge, Ce M edge, and Pr M edges at the region that highlighted in white dash lines.

Nanoscale PrO_x particles are observed all across the SSC surface, and HRTEM on the PrO_x-SSC interface is shown in Figure 3.6 A. HAADF and the corresponding elemental mapping using EELS (Sm, Co, and Pr) and EDS (Sr) are shown in Figure 3.6 B. EDS was used to determine the distribution of Sr because of the high energy loss energy of Sr L edge (~1900~2000 eV). The Sm, Co, and Sr signals can be seen inside the SSC particles, and Pr (red) covers the entire SSC surface. The EELS line scan across the PrO_x-SSC interface from the surface to the bulk is shown in Figure 3.6 C. Compared to PrO_x-GDC where distinguished Pr and Ce signals are exclusive to each other in each spectra, Pr signal coexists with Sm and Co signal at the PrO_x-SSC interface, suggesting that a solid-solution phase of Sm-Co-Pr (maybe also Sr) is formed. Those solid solution phases or PrO_x itself might be the active phase for the ORR enhancement and the main reason for the improvement in the long-term stability.

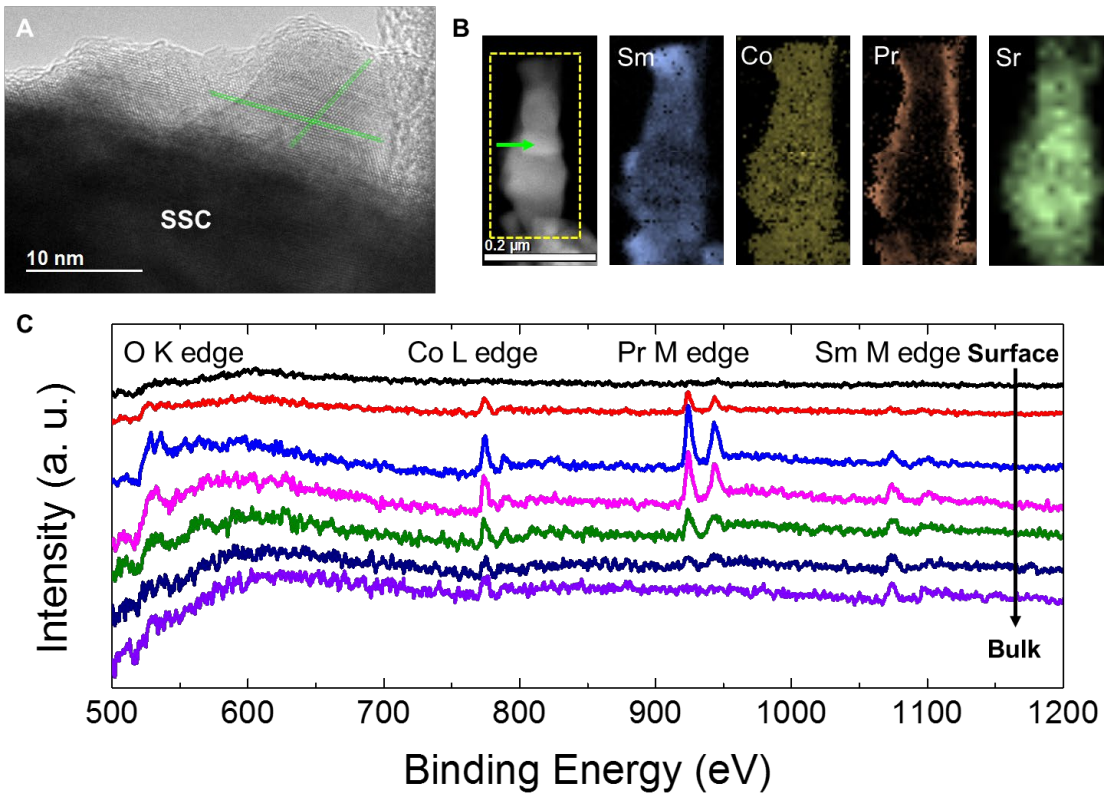

Figure 3.6 Surface Chemistry Analysis at the PrO_x-SSC interfaces. (**A**) HR-TEM on PrO_x-SSC. (**B**) HAADF and the corresponding elemental mapping using EELS (Sm, Co, and Pr) and EDS (Sr). (**C**) The EELS line scan across the green line in Figure (B).

The modified cathode was then integrated into a Ni-GDC anode supported SOFC with a 20 μm GDC electrolyte to determine the activity in a full cell level. iV characteristics of Pr-SM (closed symbols) and the unmodified cell (open symbols) are shown in Figure 3.7 A. A peak power density (PPD) of 0.4 W/cm^2 at 650 °C and 0.28 W/cm^2 at 600 °C for the unmodified SSC-GDC SOFC is shown by the open symbols, Figure 3.7 A. In contrast, the peak power density is 1.4 W/cm^2 at 650 °C and 1.1 W/cm^2 at 600 °C for the Pr-SM, more than triple that of the unmodified cell. The iV curve and EIS indicate that the rate-limiting steps of these SOFCs are the ohmic loss and the concentration polarization under high current density. Once the electrolyte thickness and the anode microstructure are optimized, the modified SOFC is expected to achieve

even higher performance at a lower temperature. SEM images highlight the cell architecture and cathode microstructure after 2000 hours of aging which are shown in Figure 3.7 C and D respectively. There appears to be no significant agglomeration of cathode particles in the cathode, or agglomeration of anode particles in the anode support layer.

The long-term aging results at 600 °C on these SOFCs are shown in Figure 3.7 E. The Pr-SM maintains a power density of over 150 mW/cm^2 under a constant current of 0.2 A/cm^2 for an operation time of about 2000 hours with high stability. The degradation rate of Pr-SM is less than 10^{-3} W/khrs, compared to $6*10^{-3}$ W/khrs for that of the unmodified one. Note that the performance of the unmodified one further drops off further drop off at ~700 hours, which does not show up in the Pr-SM cell. This result is in agreement with the symmetric cell result that shows the surface modification stabilizes SSC-GDC cathode, allowing for a longer lifetime operation.

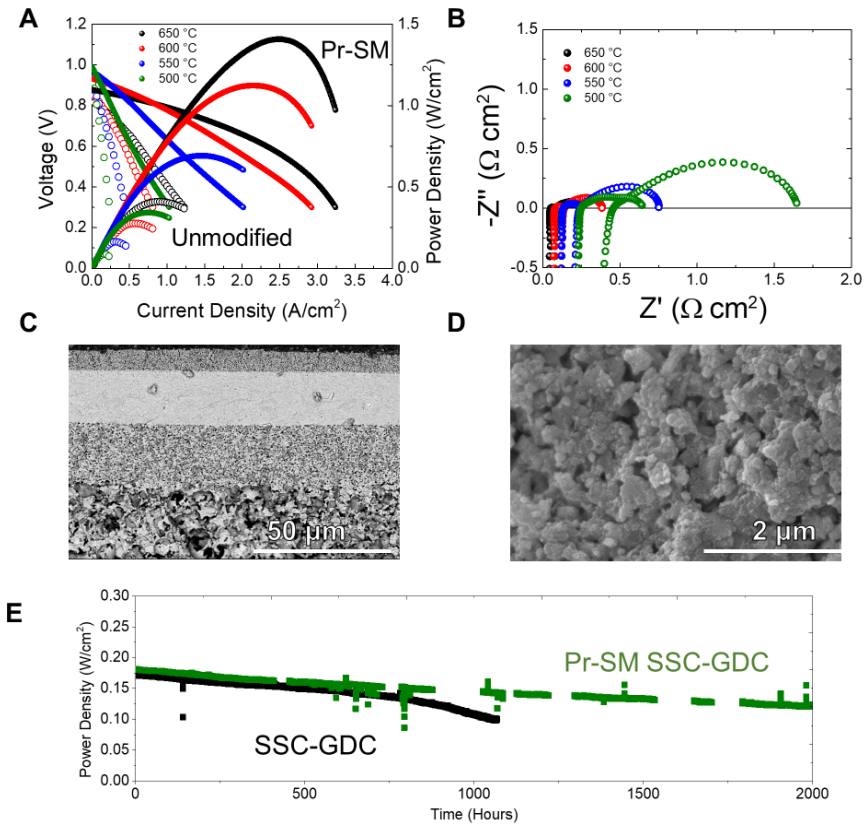

Figure 3.7 The Performance and Stability of PrO_x modified SOFCs. (**A**) iV curves for both SSC-GDC/GDC/Ni-GDC (open symbols) and Pr-SM SSC-GDC/GDC/Ni-GDC (closed symbols) (**B**) EIS for both SSC-GDC/GDC/Ni-GDC (open symbols) and Pr-SM SSC-GDC/GDC/Ni-GDC closed symbols. (**C**) Full Cell configuration. (**D**) Pr-SM SSC-GDC cathode with nanoparticles on the surface. (E) Power density of cells during galvanostatic aging at 600 °C with 0.2 A/cm^2 with H_2 as fuel.

The additional screened cathodes are shown in Figure 3.8 and Figure 3.9. The results at 600 °C were already provided in Figure 3.1, but these figures show each of the Nyquist plots for the selected infiltrates for the SSC-GDC cathode as well as LSCF-GDC and LSCF-GDC infiltrated with Pr. The LSCF experiment was performed to observe if the enhancement effect translates to other SOFC cathodes. The result is similar in that LSCF-GDC is enhanced with Pr SM by about an order of magnitude at each temperature. The other infiltrates on SSC-GDC did not seem to have the same

effect as Pr. Dy was the only other infiltrate that had an effect and the performance enhancement was marginal.

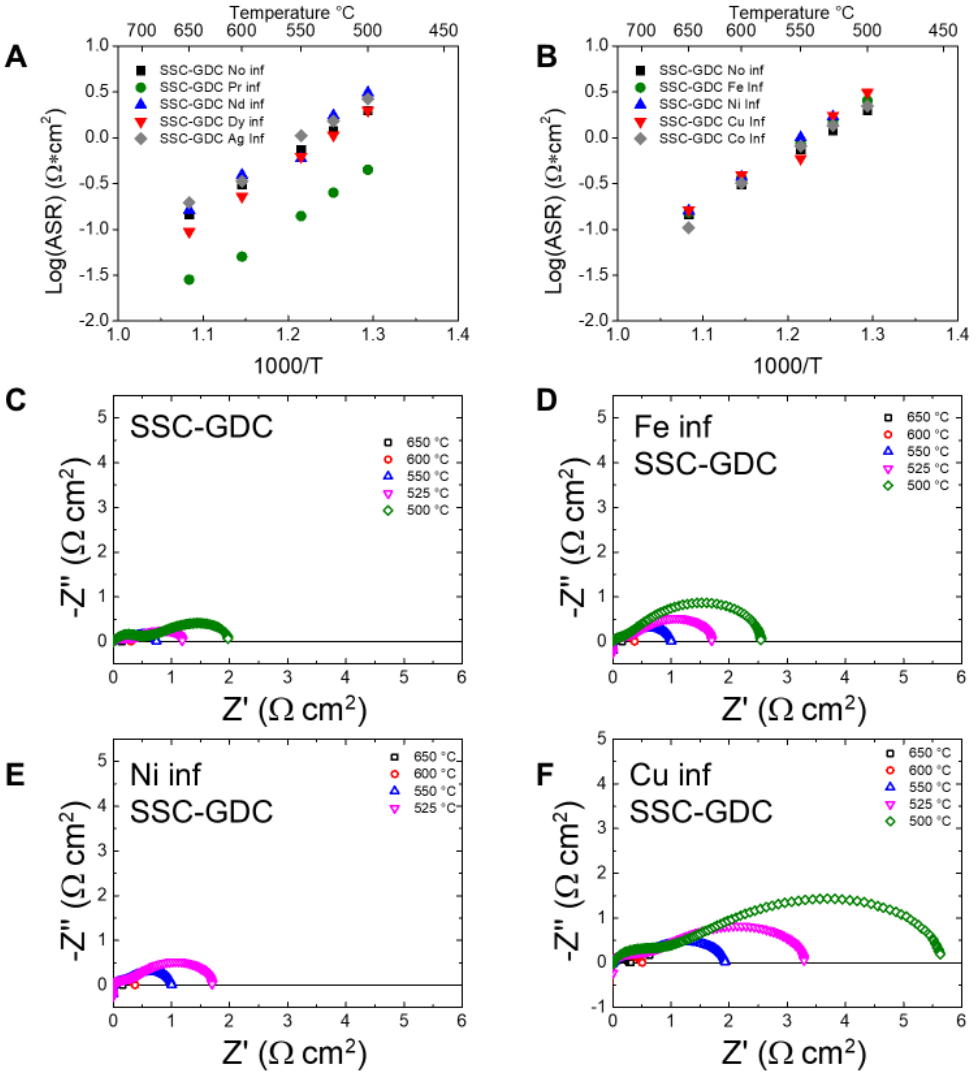

Figure 3.8 EIS of selected symmetric Cells with infiltrates. **A** Arrhenius plot of first set of SSC-GDC infiltrated symmetric cells. **B** Arrhenius plot of second set of SSC-GDC infiltrated symmetric cells. **C** SSC-GDC Symmetric cell Nyquist plot. **D** Fe infiltrated SSC-GDC symmetric cell Nyquist plot. **E** Ni infiltrated SSC-GDC Nyquist plot. **F** Cu infiltrated SSC-GDC Nyquist plot.

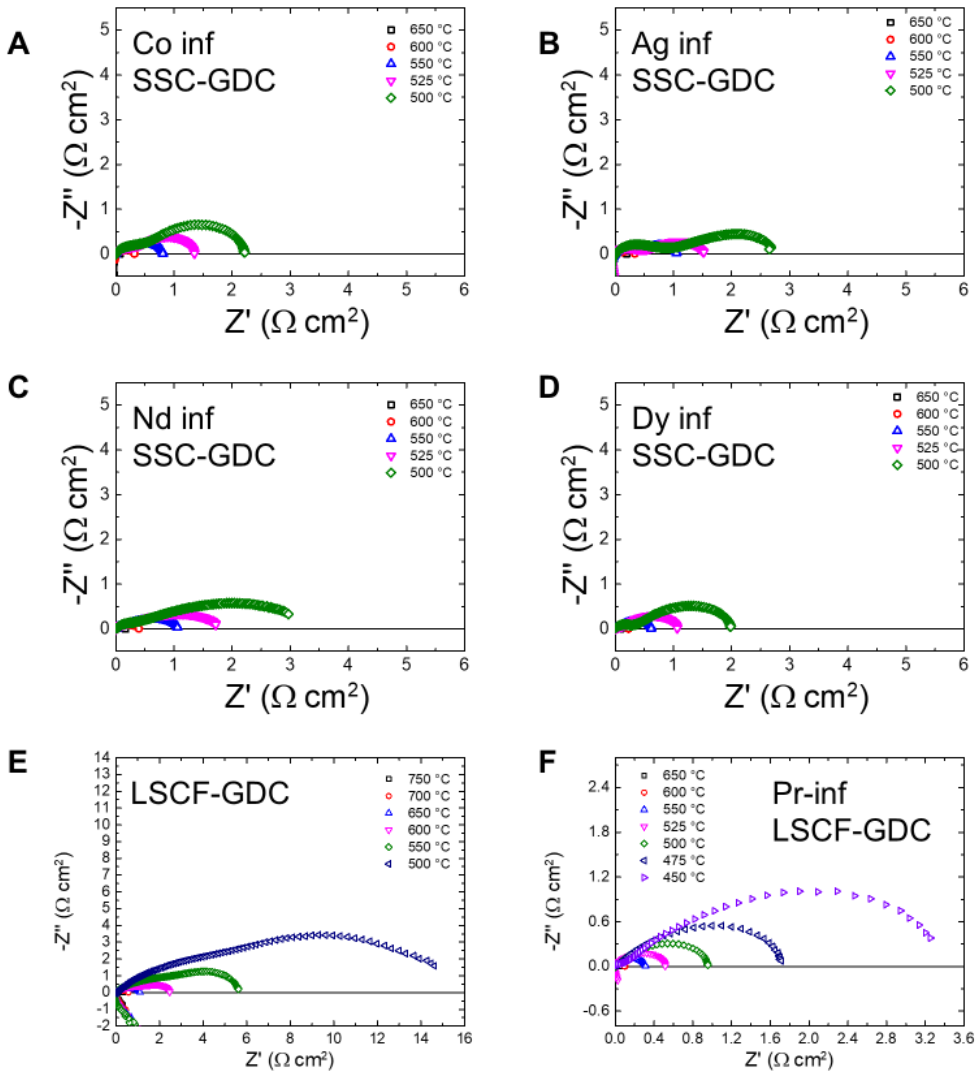

Figure 3.9 Nyquist plots of symmetric cells investigated continued. A Co infiltrated SSC-GDC symmetric cell Nyquist plot. **B** Ag infiltrated SSC-GDC symmetric cell Nyquist plot. **C** Nd infiltrated SSC-GDC Nyquist plot. **D** Dy infiltrated SSC-GDC Nyquist plot. **E** LSCF-GDC symmetric cell Nyquist plot. **F** Pr infiltrated LSCF-GDC Nyquist plot.

The aging effect for the screened infiltrates and cathode configurations is shown in Figure 3.10. Each symmetric cell was aged in air at 600 °C. The Pr infiltrated LSCF-GDC and SSC-GDC were the most stable configurations shown in Figure 3.10.

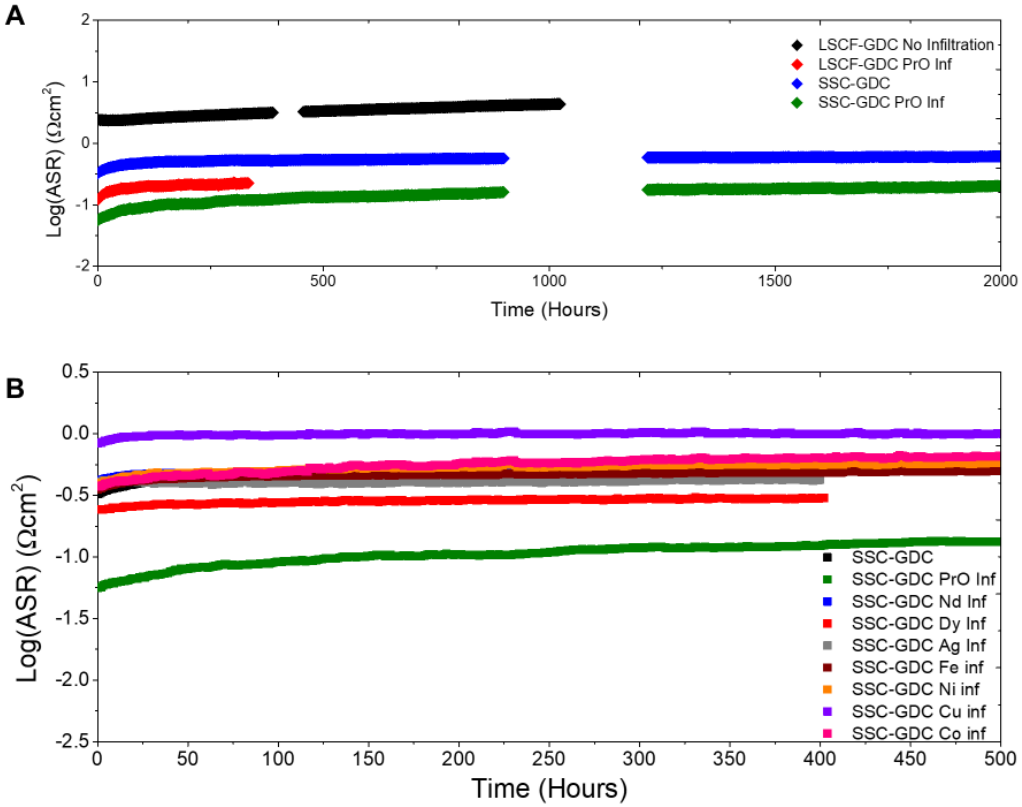

Figure 3.10 Aging of symmetric cells. A EIS aging at 600 °C of the electrode ASR for LSCF-GDC, SSC-GDC and Pr infiltrated SSC-GDC and LSCF-GDC symmetric cells. **B** Symmetric cell aging at 600 °C of the electrode ASR for SSC-GDC infiltrated symmetric cells.

The loading effect of Pr on LSCF-GDC symmetric cells is shown in Figure 3.11. One infiltration loading appears to have an effect in lowering the ASR of the LSCF-GDC cathode, three infiltration cycles appears to lower it even further, but five infiltration cycles actually increases the ASR. This could be for several reasons. First, the sample infiltrated with one infiltration may not have sufficient Pr to coat the entire surface of the cathode. Second, the five infiltration cycles amount could have too much infiltrate and clog the pores of the cathode, limiting the gas diffusion within the electrode. This outcome shows that three cycles of Pr infiltration is the optimal amount. The ASR at 500 °C for the three infiltrated symmetric cell configuration is about 10

Ωcm^2 for the baseline LSCF-GDC and is only 0.6 Ωcm^2 at 500 °C for the infiltrated case.

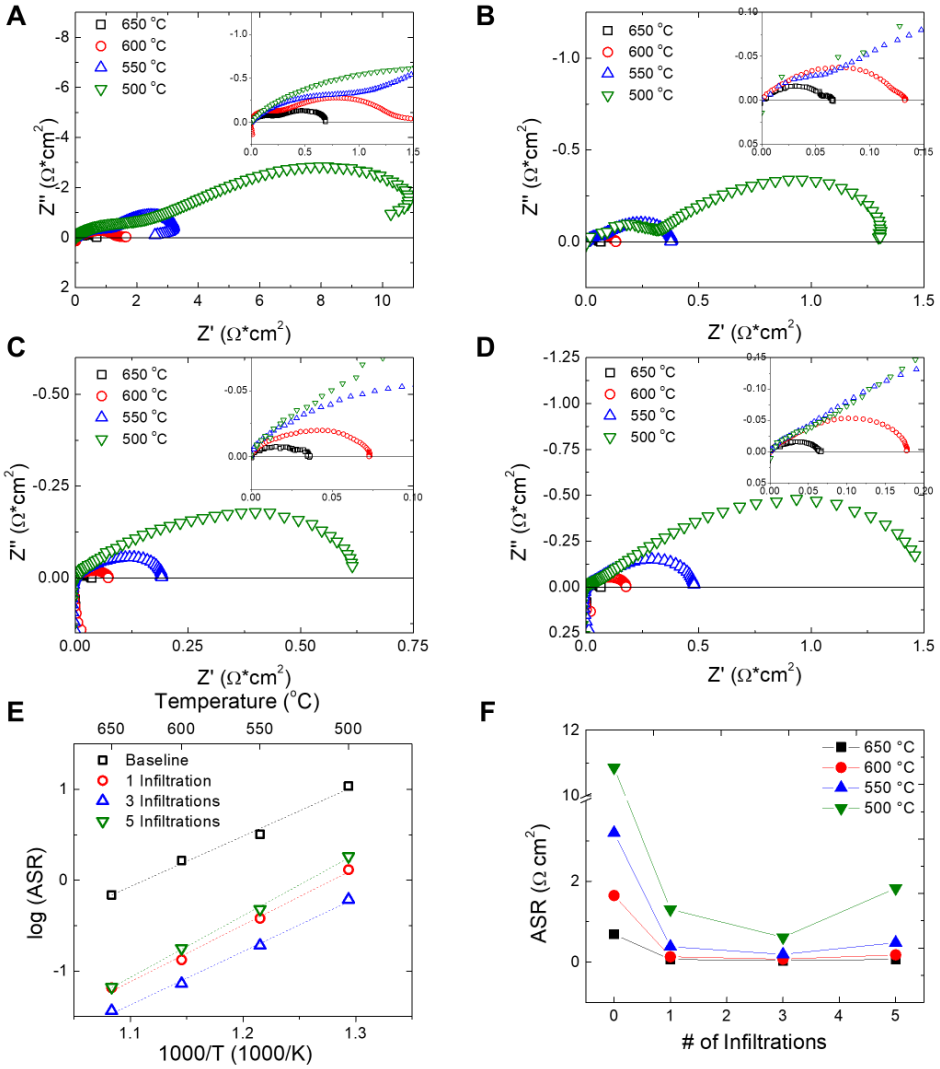

Figure 3.11 Infiltration loading effect on LSCF-GDC Symmetric Cells A No infiltration of Pr on LSCF-GDC **B** 1 infiltration loading cycle **C** 3 infiltration loading cycles **D** 5 infiltration loading cycles **E** Arrhenius plot showing all samples with their respective infiltration loading cycles **F** Isotherms of ASR vs #of infiltrations showing reverse volcano effect for the sample with 3 infiltrations.

The results for the infiltrated LSCF-GDC and reference LSCF-GDC full cell are shown in Figure 3.12. The PPD at 650 °C was about 0.5 W/cm^2 for the reference LSCF-GDC. The Pr SM LSCF-GDC showed a much higher PPD increase, just like in

the case of the Pr-SM SSC-GDC, as compared to the baseline SSC-GDC. The PPD of the Pr-SM LSCF-GDC was about 0.75 W/cm^2 at 650 °C as shown in Figure 3.12 A and B respectively for the LSCF-GDC and Pr-SM LSCF-GDC. The impedance results in Figure 3.12 C and D show that this improvement was due to a decrease in non-ohmic ASR in the infiltrated LSCF-GDC, which is consistent with the cathode symmetric cell results on LSCF-GDC. The OCV also received a slight bump at each temperature, which corresponded to about a 5% increase in OCV at each temperature in the Pr-SM LSCF-GDC as compared to the reference LSCF-GDC. This could be due to the increase in activity at the cathode-electrolyte interface which resulted in a higher local pO_2 and thus increases the pO_2 gradient the OCV.

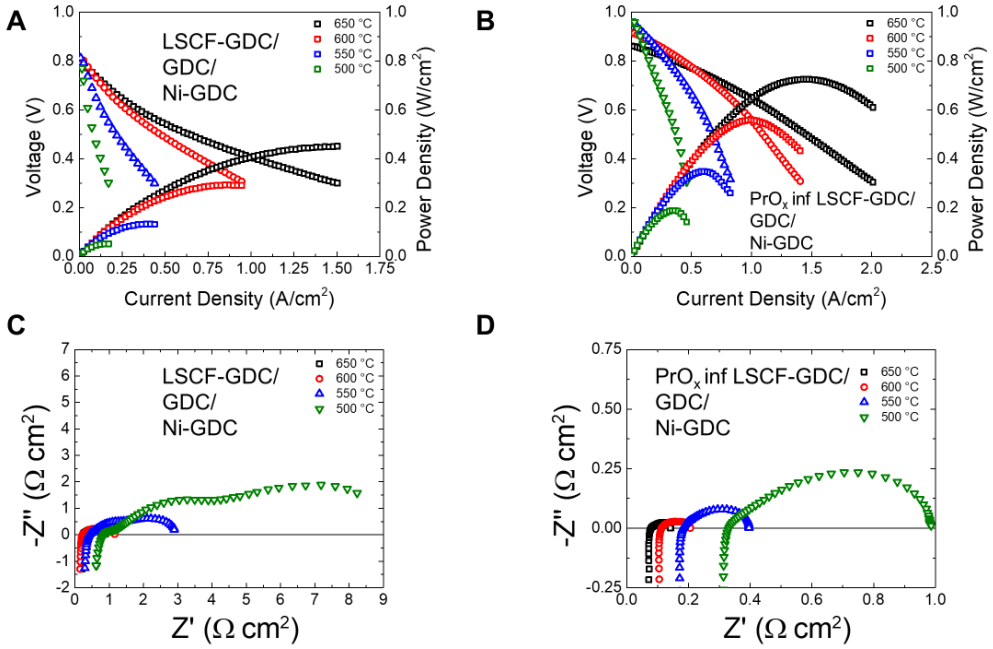

Figure 3.12 Pr SM LSCF-GDC Full Cell Results. A iV of LSCF-GDC/GDC/Ni-GDC results **B** Pr-SM LSCF-GDC/GDC/Ni-GDC iV results **C and D** LSCF-GDC and Pr-SM LSCF-GDC EIS results on a Ni-GDC/GDC cell.

3.3 Conclusion

We demonstrated that PrO_x is an active electro-catalyst that significantly enhances the ORR kinetics. As suggested by our *in situ* studies, the low-calcination temperature of PrO_x is the key to maintaining the highly active nanoscale phase with a high concentration of defects. The use of EIS, coupled with DRT, shows that the presence of PrO_x facilitates surface exchange processes and simultaneously prevents the degradation that occurs at the solid-solid interface. We showed that by slightly modifying the cathode surface, SOFC performance triples as compared to the pristine cell. In addition, this low temperature modification process has high durability for over 2000 hours. These results demonstrate the importance of surface chemistry modification on electrodes and shows a promising way to enhance cell performance and stability using a facile, simple, and cost-effective approach. Moreover, this approach reduces the cathode polarization loss over an order of magnitude and therefore can lower the operation temperature by over 100 °C.

3.4 Supplemental Experimental Not Discussed in Chapter 2

SEM was performed using a Hitatchi SU-70 with an X-ray Energy Dispersive spectrometer. Phase composition of the infiltrate powder was determined using a Bruker D8 powder X-Ray diffractometer with Cu K_α radiation. TEM on PrO_x powders was performed *in-situ* using a JEOL LaB_6 TEM with heating stage. TEM samples on the Pr-SM cell were prepared using Tescan GAIA FIB/SEM, and HR-TEM and EELS were done using the JEM 2100 FE-TEM. For TPD and TPO measurements, 0.1 g of

PrO_x powders were loaded into a micro-reactor. The reactor was placed at the center of the furnace and the inlet gas composition was controlled by mass flow controllers. The downstream of the reactor was connected to an Extrel quadrupole mass spectrometer (QMS), and the changes in m/z signals from QMS as a function of temperature were recorded. The powder samples were pretreated at 650 or 800 °C in 20 % of O_2 for two hours, and then cooled down to room temperature. The inlet gas was then switched to helium (20 SCCM) and TPD measurements were performed once the signals were stable.

Chapter 4. Mitigating Electronic Conduction in Ceria-based Electrolytes via External Structural Design

4.1 Introduction

Solid oxide electrochemical cells (SOCs) are set to be on the forefront of clean energy research to mitigate the effects of climate change.[4,5,11,14,15,63] SOCs can operate in both fuel cell and electrolysis mode (SOFC and SOEC) with high efficiency and provide flexibility in converting energy forms between chemical fuels and electricity.[4,5,10] Generally, a high temperature is required to thermally activate oxygen ion transportation and electrode reaction processes. Unfortunately, this high temperature also induces degradation issues so lowering the operating temperature is required to enable the commercialization. [4,12,63]

One main challenge of lowering the operating temperature is the significant ohmic loss that limits the performance. Among all solid electrolytes, doped ceria materials, such as $Ce_{1-x}Gd_xO_{2-\delta}$ (GDC) and $Ce_{1-x}Sm_xO_{2-\delta}$ (SDC), are more attractive options for low temperature applications than zirconia based electrolytes, $Zr_{1-x}Y_xO_{2-\delta}$ (YSZ), due to their superior oxygen ion conductivity (over orders of magnitude).[17,64] However, ceria-based electrolytes are mixed ionic and electronic conductors (MIEC) as cerium undergoes Ce^{4+}/Ce^{3+} redox couple under reducing conditions.[65,66] In turn, it causes the open circuit voltage (OCV, V_{OC}) of SOCs to be lower than theoretical, decreasing the efficiency of the device.[67] In addition, for SOECs where electricity is converted into chemical potentials, the electronic conduction in the electrolyte drastically lowers the Faradaic efficiency (FE) and makes it impractical for ceria-based

electrolytes to function in electrolysis mode.[66] The theoretical voltage (V_t) is determined by the chemical potential difference between two electrodes and can be expressed by the Nernst equation shown in equation 1.1.

The cell voltage can be calculated by using the apparent transference number of the cell electrolyte ($t_{O^{2-}}^{A}$) and V_t from equation 2.5 where $t_{O2-} = t_{O^{2-}}^{A}$. Note that $t_{O^{2-}}^{A}$ represents the apparent ratio of ionic conductivity in total conductivity. In the case of MIECs (e.g., doped ceria), because of the different degrees of $Ce^{4+/3+}$ redox states across the electrolyte, the total electronic conductivity in electrolyte is directly affected by thickness, gas environments, and operating conditions.[68] Although a thicker doped ceria layer can increase the apparent ionic conductivity ratio because cerium does not fully reduce, it also contributes to a higher ohmic loss, which severely penalizes the performance at low temperatures.[69–71] A typical 20 μm thin GDC electrolyte has only 80% of V_t at 500 ºC, which suggests that the efficiency can significantly increase once the leakage current is limited.[70–72]

One approach is to find new materials that have a high $t_{O^{2-}}$, but so far there is no single candidate that meets all criteria of low-temperature solid electrolytes. Another approach is to reduce the thickness of conventional YSZ electrolytes. To limit the ohmic loss < 0.1 Ωcm^2 at 500 °C, the dense, defect free, YSZ thin film needs to be < 1 μm,[73] which is very challenging using traditional, scalable ceramic processing techniques. The other approach is to modify the defect chemistry of the known electrolytes, such as introducing different dopants in ceria. For instance, $Pr_xCe_{1-x}O_{2-\delta}$ (PCO), x < 0.01 has been reported to have a high $t_{O^{2-}}$ is attainable, $t_{O2-} \approx 1$ in the high pO_2 regime. However, PCO displays a lower ionic conductivity than GDC

(approximately 2/3 σ_{ion}), and in the low pO_2 regime the $t_{O^{2-}} < 1$ is significantly less than that of GDC (~0.4 at 10^{-15}atm), making PCO an unsuitable electrolyte for low temperature SOFCs.[74] Despite various attempts to increase the intrinsic $t_{O^{2-}}$ of doped ceria, it doesn't prevent the nature of Ce^{4+} reduction, and the leakage current is the necessary sacrifice for using high oxygen conducting ceria-based electrolytes.

Here we address the leakage current issue in ceria-based electrolytes and demonstrate that the electronic conduction of ceria-based electrolytes is mitigated via the external structure design, reaching FE=93% for a 20 μm GDC at 500 ºC. We engineer a porous function layer (PFL) that allows the exposure of this ceria layer to high oxygen partial pressure (pO_2) and show that the intrinsic electron charge carrier density in this porous layer is significantly lower because of the gas-solid equilibrium of the PFL in air. In addition, by engineering the PFL with active dopants, the dopants in the PFL facilitate oxygen transport and show the synergistic effects to significantly enhance the cell performance. These two facts produce a system exhibiting a much higher OCV, lower area specific resistance (ASR), higher performance and increased durability, and cell operation >2000 hours with no performance losses.

4.2 Results and Discussion

For stoichiometric materials like doped ceria, dominant defects are controlled by the oxygen level x in $Ce(Gd)O_{2-x}$. These defects are the main charge carriers that determine the electronic and ionic conductivity. In reducing conditions, the reduction of Ce^{4+} to Ce^{3+} significantly increases the electronic conductivity. From the solid-state chemistry point of view, the electron charge carrier concentration, n, increases as the increase in x value to accommodate the formation of positively charged oxygen vacancies. In contrast, in high pO_2 regime, the high oxygen chemical potential maintains a low level of x, and thus limits the electronic conductivity of the doped ceria.

Figure 4.1 (A) and (B) show the schematics for the cases where a PFL is present or not, and the operating gas environments for cathode and anode of SOFCs are highlighted in light blue and green, respectively. In the case of PFL, Figure 4.1 (A), oxygen molecules can freely diffuse and a homogeneous stoichiometry of this porous layer is achieved. Thus, the entire PFL has a constant defect concentration as it is exposed to the same environment (i.e., pO_2=0.21atm). In contrast, for the case with only a dense electrolyte layer (DEL) in Figure 4.1 (B), the air environment only extends to the cathode/electrolyte interface.

The advantage of the PFL can be clearly seen in the plot of electron charge carrier density versus distance in Figure 4.1 (C). The area underneath the curve represents the total electron charge carriers in the electrolyte. Compared to the case with the presence of the PFL, the boundary condition that equilibrates the oxygen chemical potential with cathode gas environment is now pinned to the DEL/PFL interface from the cathode/electrolyte interface because of the porous nature of PFL.

This change significantly lowers the electron charge carrier density in the electrolyte layer, as shown using green lines. The ratio of ionic conductivity to electronic conductivity as a function of distance is shown using dashed lines. As electron charge carrier concentration and mobility in the PFL for electrons are limited through external structure, the apparent transference number, $t_{O2\text{-}}^{A}$, increases. This enhancement in the ionic/electronic conductivity ratio can significantly improve the efficiency of ceria-based electrolytes.

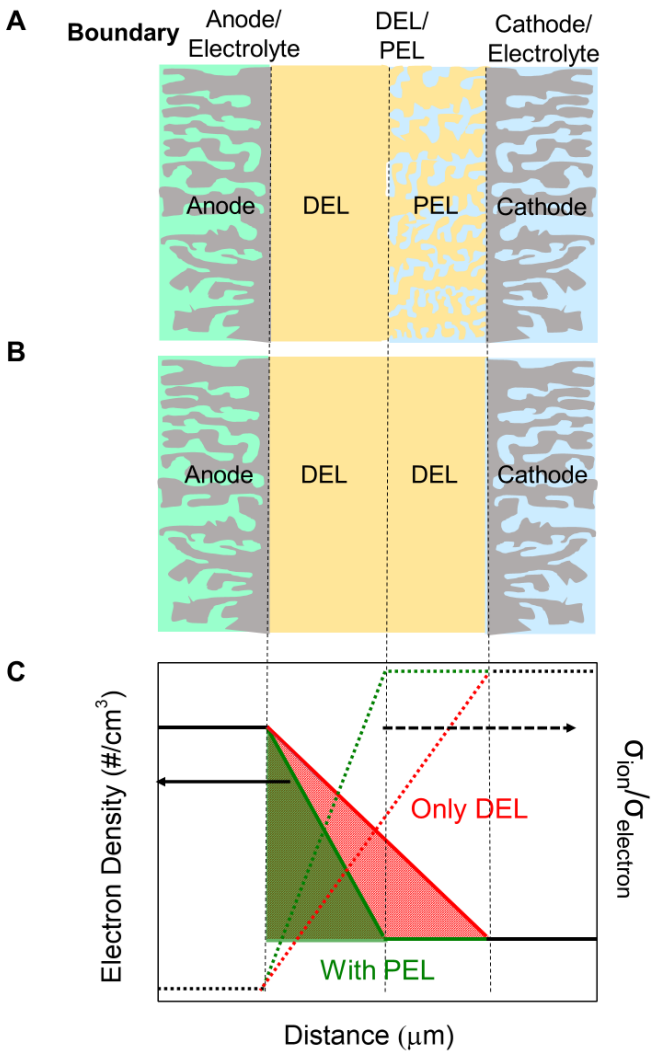

Figure 4.1 Electronic Conduction Mitigation via External Structure Design. Schematic drawing of the cell configuration of (A) with PFL and (B) without PFL. (C) The corresponding change in *electron* charge carrier density as a result of porous structure based on the simplified defect model.

To examine this concept, we used a typical SOFC configuration with conventional low-temperature electrode materials such as $Sr_{0.5}Sm_{0.5}CoO_{3-\delta}$–$Ce_{0.9}Gd_{0.1}O_{2-\delta}$ (SSC-GDC)/GDC/Ni-GDC and inserted a PFL, as shown in the cell architecture in Figure 4.2 (A). The scanning electron microscopy (SEM) image in Figure 4.2 (B), highlights the discrete layers of cathode, PFL, DEL and anode. The

microstructure of the Pr-GDC is also shown, detailing the porous nature of the Pr-GDC layer. Cell results shown in Figure 4.2 C highlight the impact of using only a 10μm thick DEL + 10 μm thick PFL vs that of a 20 μm DEL.

The PFL provides two positive effects to the cell, an increase in OCV and a decrease in impedance loss. The OCV increases from 0.91 to 0.98 V at 500 °C and from 0.88 to 0.95 V at 550 °C with an improvement of ~8%, as a result of defect engineering. When replacing 10 μm DEL with PFL, the ohmic ASR losses drop from 0.25 Ωcm^2 to 0.17 Ωcm^2 at 550 °C, as shown in electrochemical impedance spectroscopy (EIS) in Figure 4.2 D. The main reason for the ohmic difference is likely the higher electronic conductivity of 10 μm versus 20 μm DEL due to different levels of Ce reduction. In addition, the use of PFL decreases non-ohmic polarization in both tested temperatures. These factors lead to a large increase in peak power density (PPD) to 0.36 and 0.76 W/cm^2 at 500 and 550 °C, respectively.

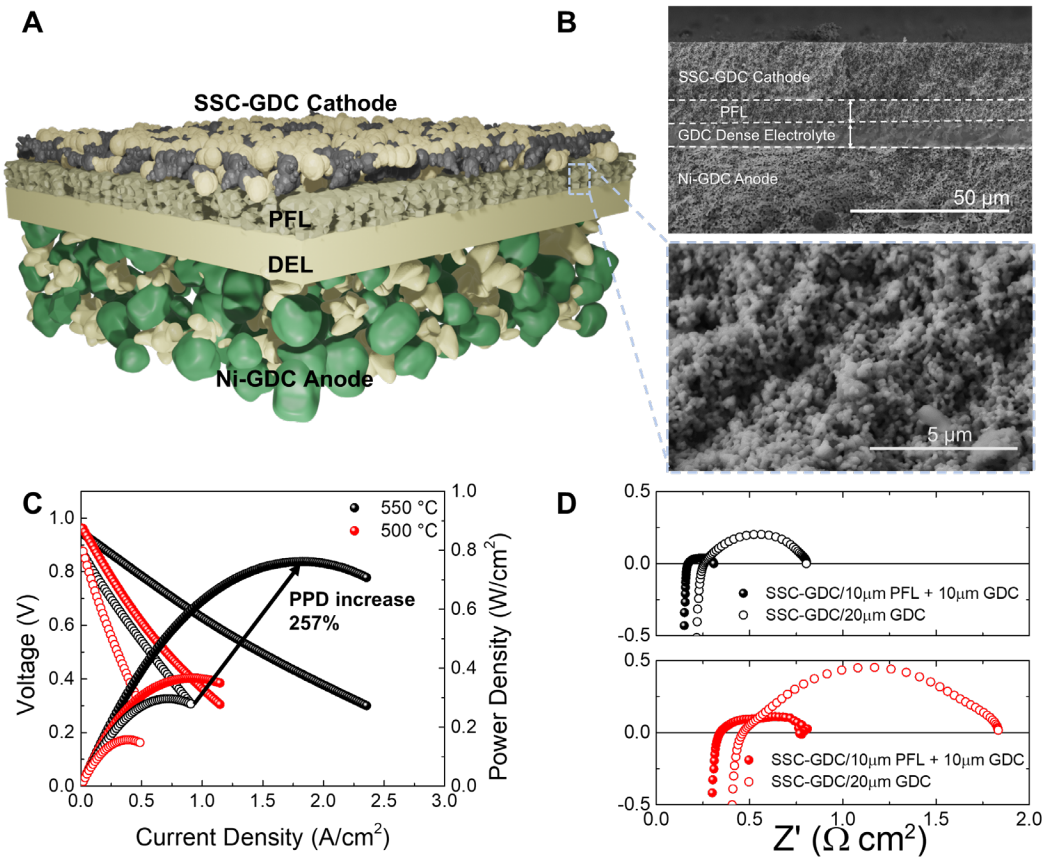

Figure 4.2 SOFC Design, Microstructure, and Electrochemical Performance. (A) The cell design with the PFL. (B) SEM image of the microstructure of the cell, 20 µm SSC-GDC cathode, 10 µm Pr-GDC PFL, 10 µm GDC electrolyte, 20 µm anode functional layer (AFL), and 500 µm Ni-GDC anode. The enlarged view of the PFL microstructure is also shown. (C) Current voltage (iV) behavior at 500, 550 °C (red and black, respectively) shown for the 20 µm GDC in open symbols and 10 µm DEL + 10 µm PFL (with 0.5 wt% PrO_{2-x}). (D) EIS spectra at both 500 and 550 °C, shown for the 20 µm DEL and 10 µm DEL + 10 µm PFL (open and closed symbols, respectively).

Chemical compositions of the cell are shown in Figure 4.3. Figure 4.3 A shows the electron dispersive spectroscopy (EDS) mapping of the elements in each solid oxide layer. A sharp interface between cathode and PFL can be clearly seen based on Co signal. Both PFL and DEL are ceria-based, and the concentration of Pr is too low to be detected using EDS. Further content of Pr in the Pr-GDC layer can be seen in Figure 4.3 B where time of flight secondary ion mass spectroscopy (ToF-SIMS) was performed. The y-axis represents the depth and the colormap is the signal intensity of

each element. Sr, Pr, and Ce are shown in this mapping where the Sr signal discretely exists only in the cathode. The sharp cathode/PFL interface indicates there are no interdiffusion issues. Pr appears in the PFL, and Ce appears in both the PFL and cathode because the use of a composite cathode.

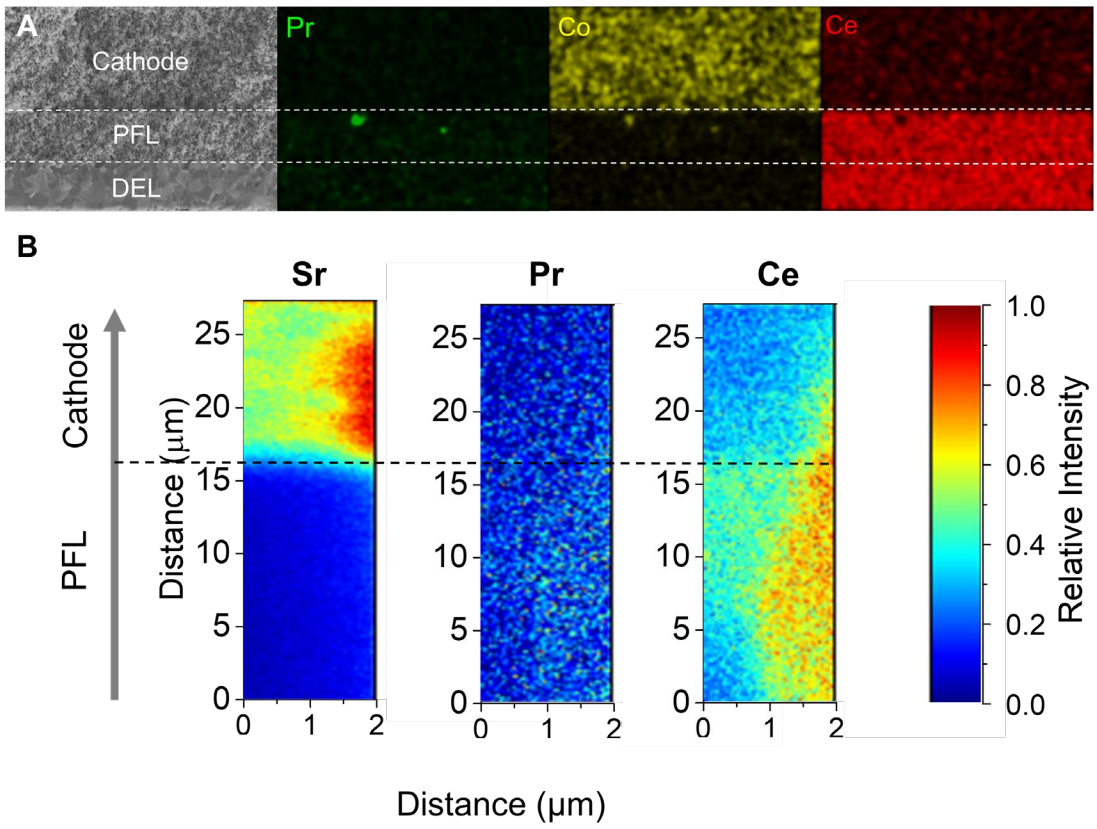

Figure 4.3 Chemical Analysis of the PFL. (A) SEM-EDS of the cathode, PFL, and electrolyte interface with constituent elements from each the cathode, electrolyte, and PFL. (**B)** ToF-SIMS of elemental mapping across the cathode/PFL interface. X-axis and Y-axis represent the planar and the depth profile. The colormap (arbitrary unit) represents the intensity of each element.

SOFCs with different DEL thicknesses and PFL concentrations were tested to understand the OCV enhancement mechanism of the PFL, and their OCVs are summarized in Figure 4.4. First, we demonstrated the effectiveness of the PEL on the OCV enhancement by depositing it on a 200 μm GDC supports, as shown in Figure 4.4

A. By doing so, the GDC thickness effect on the OCVs can be minimized. Due to the MIEC in GDC, the apparent ionic transference number, t_{O2-}^{A}, of GDC (black dots) reaches only 0.91 V at 500 °C. As temperature increases, oxygen nonstoichiometry, *x*, and electron defects are both thermally activate which leads to the further decrease in t_{O2-}^{A} to 0.85 V at 650 °C. With the PFL, t_{O2-}^{A} improves significantly, and the enhancement is much more effective at low temperatures.

Figure 4.4 D shows the PFL effect on thin GDC electrolytes with a thickness from 10 to 20 μm. The GDC baselines are shown in open symbols. The theoretical voltage, as well as the level of 95 and 90 % Faradaic efficiency (FE), are also shown. When the thickness of GDC decreases from 200 μm to 20 μm, the OCV drops over 10%, mainly because of the high electrochemical gradient (air/H_2@3%H_2O) across the thin electrolyte, 5.8 versus 58 mV/μm for 200 to 20 μm thick GDC, respectively. The high electrochemical potential forces the reduction of Ce 4+/3+ redox couple and increases electronic conductivity.

Compared to the 20 μm GDC baseline, the presence of PFL increases OCV at all temperatures. The drop in OCV for the 10 μm DEL case at 650 °C could be due to micro-pinholes. With the increase in DEL thickness, the OCV further increases and can reach 90% and 93% of theoretical value at 500 and 550 °C respectively. This external structure design enhances the OCV efficiency, as the OCV of the 20 μm thick GDC + 10 μm thick PFL is higher than that of the 200 μm thick GDC.

One important perspective is the trade-off between the OCV enhancement and its associated ohmic loss. Since the extrinsic structure design can minimize the electron conduction in GDC, we can minimize the thickness of the DEL to minimize ohmic loss

for oxygen transport. Figure 4.4 C shows the thickness effect of a 10 μm PFL (0.5wt%PrO_{2-x}-GDC) paired with varying DEL thicknesses. The ohmic ASR depends linearly on varying electrolyte thickness, with the lowest value in the 10 μm DEL sample. The OCV can achieve over 1 V with only ~0.3 Ωcm^2 at 500 °C. The OCV of the 15 μm DEL + 10 μm PFL maintains a high OCV comparable to the OCV of the 20 +10 μm configuration, without the ohmic losses of a 20 μm thick electrolyte, suggesting that over 15 μm, the DEL has minimum effect on the OCV increase but contributes to ohmic loss.

Figure 4.4 D shows the doping level effect on the OCV enhancement. Adding Pr as a homogenous dopant in PFL has minimal effects on the OCV enhancement, suggesting that the external porous structure is the key factor for the decrease in electronic conduction in GDC layers, and the chemical composition of the PFL is not the main cause. Nevertheless, the addition of Pr has a significant impact on electrochemical performance and will be discussed in the next section.

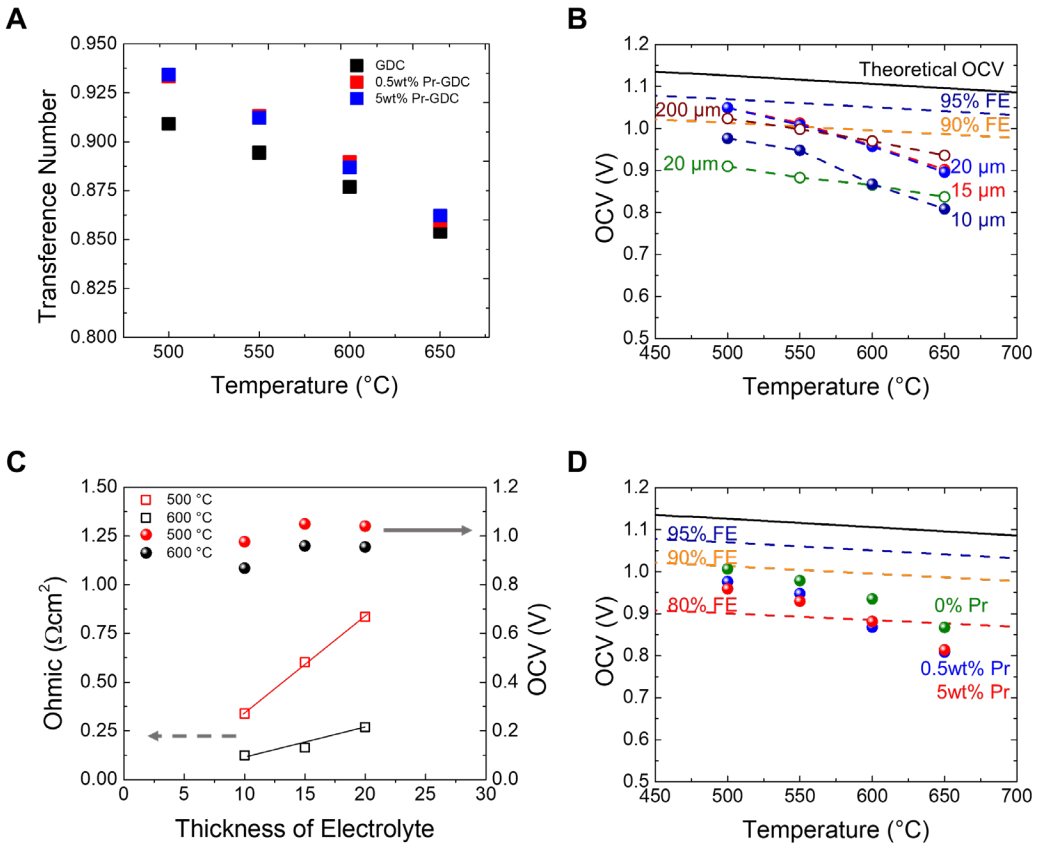

Figure 4.4 The OCV enhancement via the PFL. (A) Transference Number measurement on 10 µm PFL/200 µm GDC. (B) OCV Enhancement with PFL on 20 µm GDC with different PFL thicknesses. (C) Ohmic loss and OCV enhancement at 500 °C (red) and 600 °C (black) with varying GDC electrolyte thickness paired with 10 µm PFL (with 0.5wt%PrO_{2-x}). (D) OCV vs Temperature varying Pr doping level in 10 µm PFL, the thickness of the 5 wt% Pr sample is 15 µm.

The PFL effect on the electrochemical performance enhancement is determined using a symmetric cell configuration. Figure 4.5 A shows a Nyquist plot of SSC-GDC cathodes with or without the presence of the PFL. The addition of PFL reduces polarization impedance and the Pr concentration in the PFL plays a role in the overall cathode performance. The PFL with 0.5 wt% PrO_{2-x} has the lowest cathode ASR, 0.7 Ωcm^2, compared to 3.2 Ωcm^2 without PFL. A pure porous GDC layer reduces cathode

ASR, likely due to the increase in active area and the addition of multivalent Pr, and further enhances the electrochemical performance. The higher doping level of Pr (5 wt%) may act as a sintering aide as the microstructure shown in Figure 4.6 F appears to densify, thus decreasing the active area.

We further tested PFL/GDC symmetric cells (without SSC-GDC cathodes) to separately determine electrochemical activity of the PFL. An Arrhenius plot of cathode ASR in Figure 4.5 B displays that the PFL lacks sufficient cathode activity on its own, regardless of the Pr doping level, as the electrode polarization is 2-3 orders of magnitude higher than the cathode on top of the PFL configuration. The impact of Pr is further shown in the same plot; PFL acting as a cathode has an ASR that is orders of magnitude higher than conventional SSC-GDC cathodes (black dots), highlighting that GDC does not have sufficient cathode activity.

The distribution of relaxation times (DRT) analysis in Figure 4.5 C further elucidates how the PFL enhances cathode performance.[28,44,47,56,75,76] The specific region of interest in this case is the intermediate time constant region (10^{-3}-10^{0} (s)), as this region shows that SSC-GDC without a PFL (black curve) has the highest overall reaction losses in the region (time constant (τ)=10^{-3}- 10^{0}(sec)), which is typically attributed to the surface reaction.[47,56,77,78] With the addition of the PFL, the intensities of these peaks decrease, suggesting the PFL facilitates surface reaction steps, which is consistent with previous findings.[77]

Isothermal oxygen partial pressure (pO_2) dependent studies and the corresponding DRT analysis are shown in Figure 4.5 (D) and (E) to help determine the exact role of the PFL on the cathode performance. Double log plot of cathode ASR

versus log (pO_2) shows that by adding the PFL, the impedance is lowered at all pO_2's with a slope change from 1/4 to 1/6, indicating that the change of the rate-limiting-step on the surface reactions. [79,80] The DRT results deconvolute the impedance results to show that the PFL decreases the reaction losses in the surface reaction region ($\tau=10^{-3}$-10^{0}(s)).

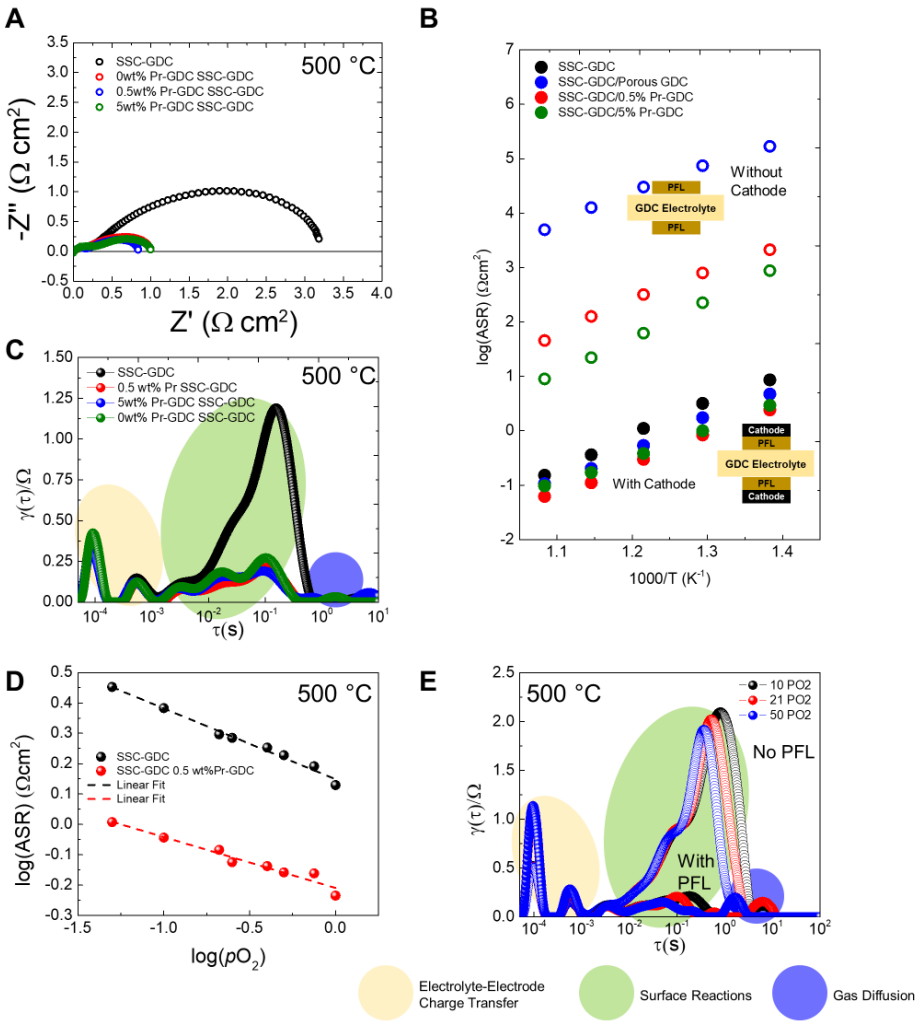

Figure 4.5 Electrochemical enhancement due to PFL layer composition. (A) Nyquist plots at 500 °C of SSC-GDC cathode symmetric cell with varying Pr doping level in the PFL. (B) Arrhenius behavior of SSC-GDC symmetric cells with or without the PFL. The colors correspond to the concentration of Pr in the Pr-GDC layer and the open symbols account for a situation where the PFL is tested on its own and closed

symbols show SSC-GDC on top of the PFL. (C) Corresponding DRT analysis in (A). (D) pO_2 dependent behavior comparing SSC-GDC with or without PFL at 500 °C and (E) corresponding DRT curves.

We further integrated our previous surface modification work with the PFL-based cells and have highlighted the durability and performance enhancements in Figure 4.6.[47,48] As shown in Figure 4.6 A, PFL-based SSC-GDC SOFC has a PPD of 0.35 W/cm^2 at 500 °C in H_2. With the Pr surface modification cathode (Pr-SM SSC-GDC), a PPD of 0.55 W/cm^2 is reached. This result shows higher performance than a benchmark study done with a similarly configured cell.[10] The iV result can be directly correlated to the cell impedance where the Pr-SM SSC-GDC/PFL cell has a total ASR of 0.3 Ωcm^2 at 500 °C whereas the SSC-GDC/PFL has a total ASR of 0.75 Ωcm^2 at 500 °C, as shown in Figure 4.6 B. The cathode surface modification significantly lowers the cell ASR.

Cells were aged at 500 °C and 550 °C under 0.2 A/cm^2 in H_2, and the terminal voltage and the corresponding cell ASR are shown in Figure 4.6 C and D, respectively. The SSC-GDC/PFL cell (black dots) shows high durability at 550 °C for over 800 hours and demonstrates that the porous design of the PFL can withhold its functionality even after long-term aging. Moreover, the Pr-SM cell further enhances performance and allows the cell to possess the same power density to operate at 50 °C lower temperature. The modified cell shows a PPD of 0.5 W/cm^2 at 500 °C with excellent stability for over 2000 hours of operation. The cell ASR of the Pr-SM SSC-GDC/GDC/Ni-GDC is shown in Figure 4.6 D, resolving the ohmic and non ohmic contributions. No major degradation presents over the course of 2000 hours of operation. It is noteworthy that the present work was all done using cost effective, feasible, and scalable ceramic

processing techniques such as tape casting and screen printing, which is in contrast to the techniques used by most high-performance/durability studies in the literature.

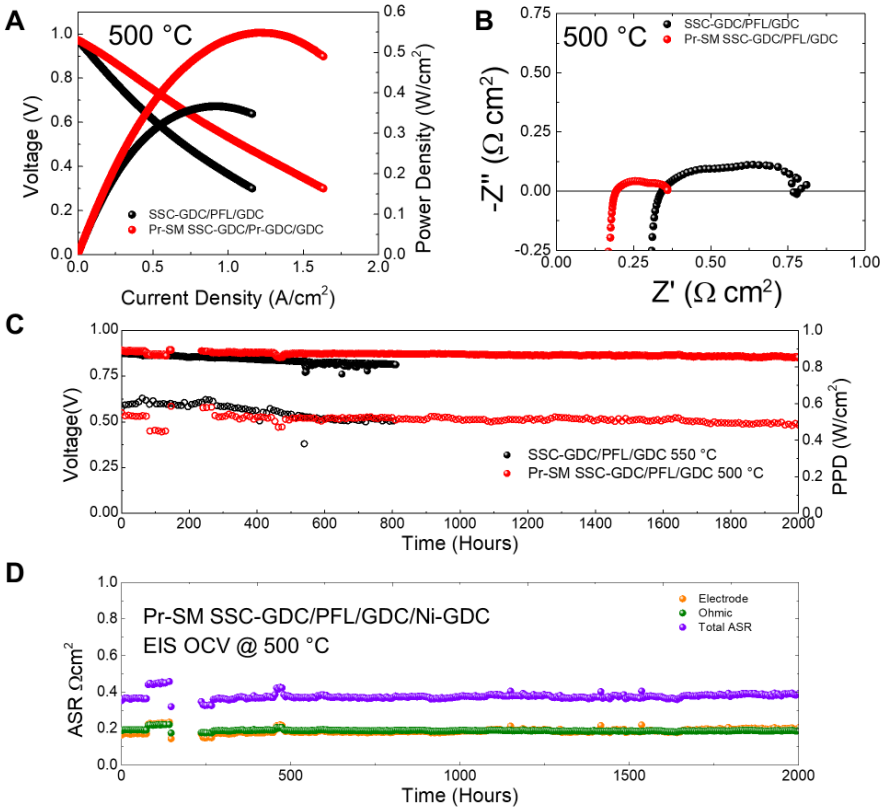

Figure 4.6 Performance and Stability of PFL-based SOFCs. (A) iV and (B) EIS of Pr-SM SSC-GDC and SSC-GDC/PFL/GDC/Ni-GDC at 500 °C. (C) SSC-GDC/PFL/GDC/Ni-GDC and Pr-SM SSC-GDC galvanostatic aging result highlighting PPD vs time (right) and (D) the corresponding ASR change for Pr-SM SSC-GDC/PFL configured cell. The incident at hour 100-200 was the result of a power incident.

The EIS results from Figure 4.5 are shown in their entirety in Figure 4.7 below. The best overall configuration is the SSC-GDC/PFL with a 0.5wt% Pr-GDC configuration. This could be due to one of two phenomena. First, the Pr in the PFL adds activity to the PFL and allows greater oxygen activity in the PFL layer. Second, the Pr in the PFL layer could densify the system, add conductivity, and reduce the interfacial resistance between the cathode and PFL due to a higher TPB length at the PFL-Cathode

interface. The DRT results show that for the time constant regime 10^{-3}-10^{0} (s), the surface reactions are enhanced as explained previously.

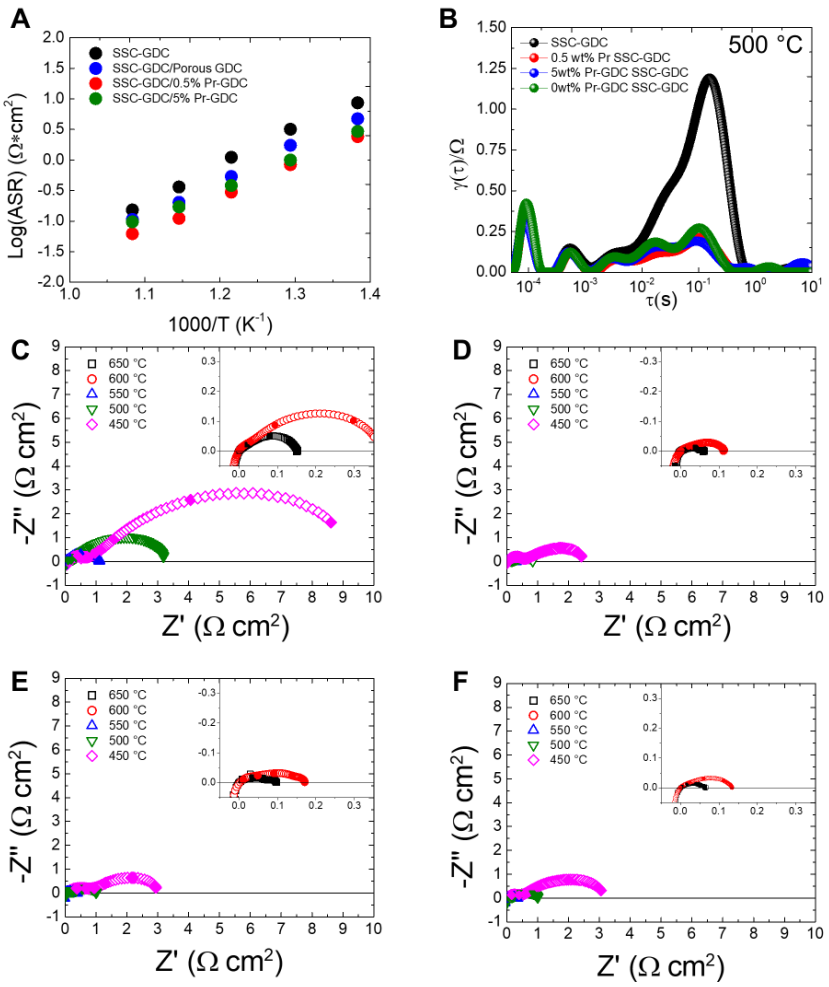

Figure 4.7 EIS of selected symmetric cells with different PFL compositions. A Arrhenius behavior of selected symmetric cells. **B** DRT of symmetric cells at 500 °C same figure as in main manuscript. **C** SSC-GDC symmetric cell. **D** SSC-GDC symmetric cell with 0.5wt% Pr-GDC PFL **E** SSC-GDC symmetric cell with 5 wt% Pr-GDC PFL **F** SSC-GDC symmetric cell with Porous GDC PFL.

To further understand the PFL effect on cathode performance, PFL/GDC/PFL symmetric cells were tested in air for their respective configurations. The results depicted in Figure 4.8 below show that the PFL without a cathode does not contain

sufficient activity to operate the cathode reaction. The electrode ASR ranges from 10-100000 Ωcm^2 for the respective PFL symmetric cell configuration, which is insufficient to operate a fuel cell with meaningful power generation. The DRT results for the PFL symmetric cells do not indicate what specific mechanism prevents the cathode reaction activity.

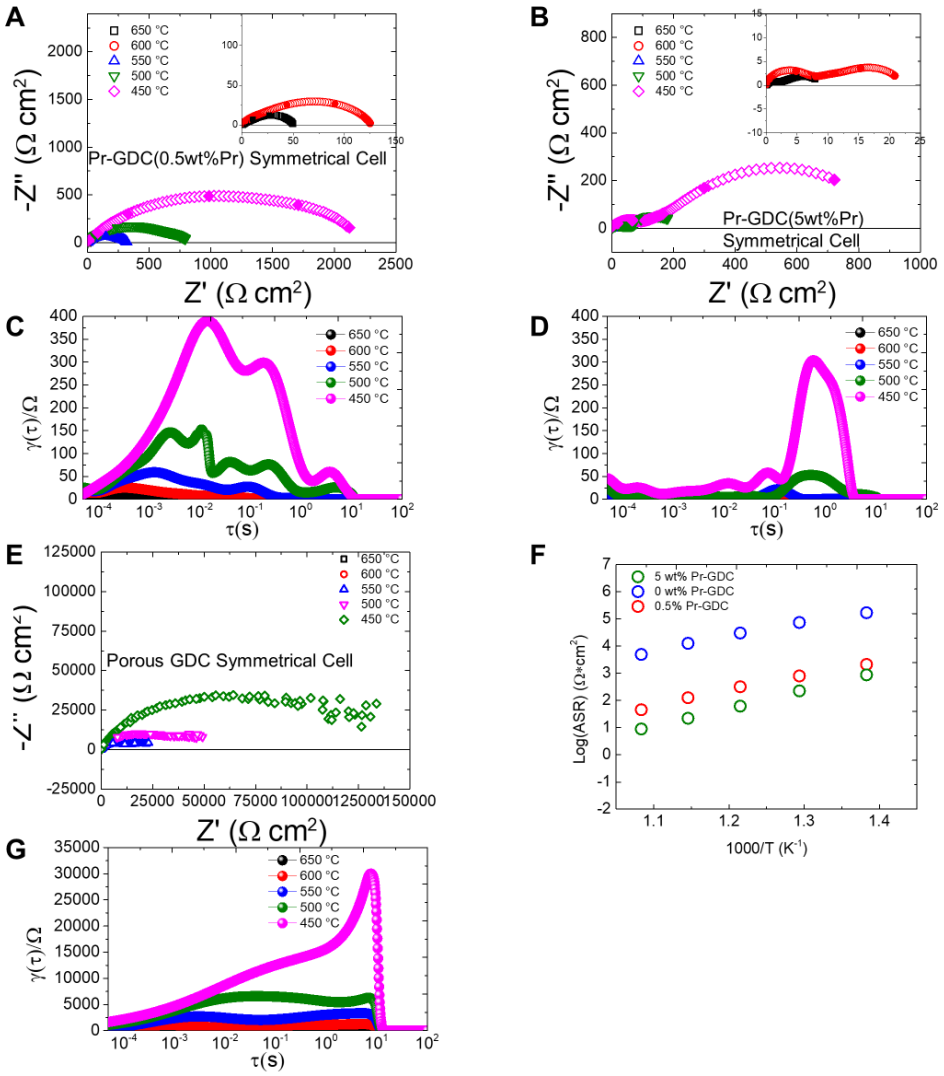

Figure 4.8 Nyquist plots and DRT continued, standalone PFL no cathode: A 0.5wt% Pr-GDC PFL symmetric cell. **B** 5 wt% Pr-GDC PFL symmetric cell. **C** DRT of PFL EIS shown in **A**. **D** DRT of PFL EIS shown in **B**. **E** porous GDC PFL symmetric cell. **F** Arrhenius plot of PFLs with varying composition of Pr. **G** DRT of PFL EIS shown in **E.**

The fully integrated cells depicted in Figure 4.9 help demonstrate the DEL thickness effect on cell performance. The cell configuration with a DEL of 10 μm shows quite high performance at all respective temperatures. At 600 °C, a PPD of 1.3 W/cm^2 is attainable with a PFL containing 0.5 wt% Pr-GDC. This is most likely due to the high activity of the SSC-GDC/PFL configuration seen in the symmetric cells. However, at high current densities, concentration polarization persists which could be shorting due to the internal leakage current of the GDC or microstructural effects in the electrodes. The flow rate was doubled on each electrode to observe if it was microstructural limitations, but the flow rate had little effect.

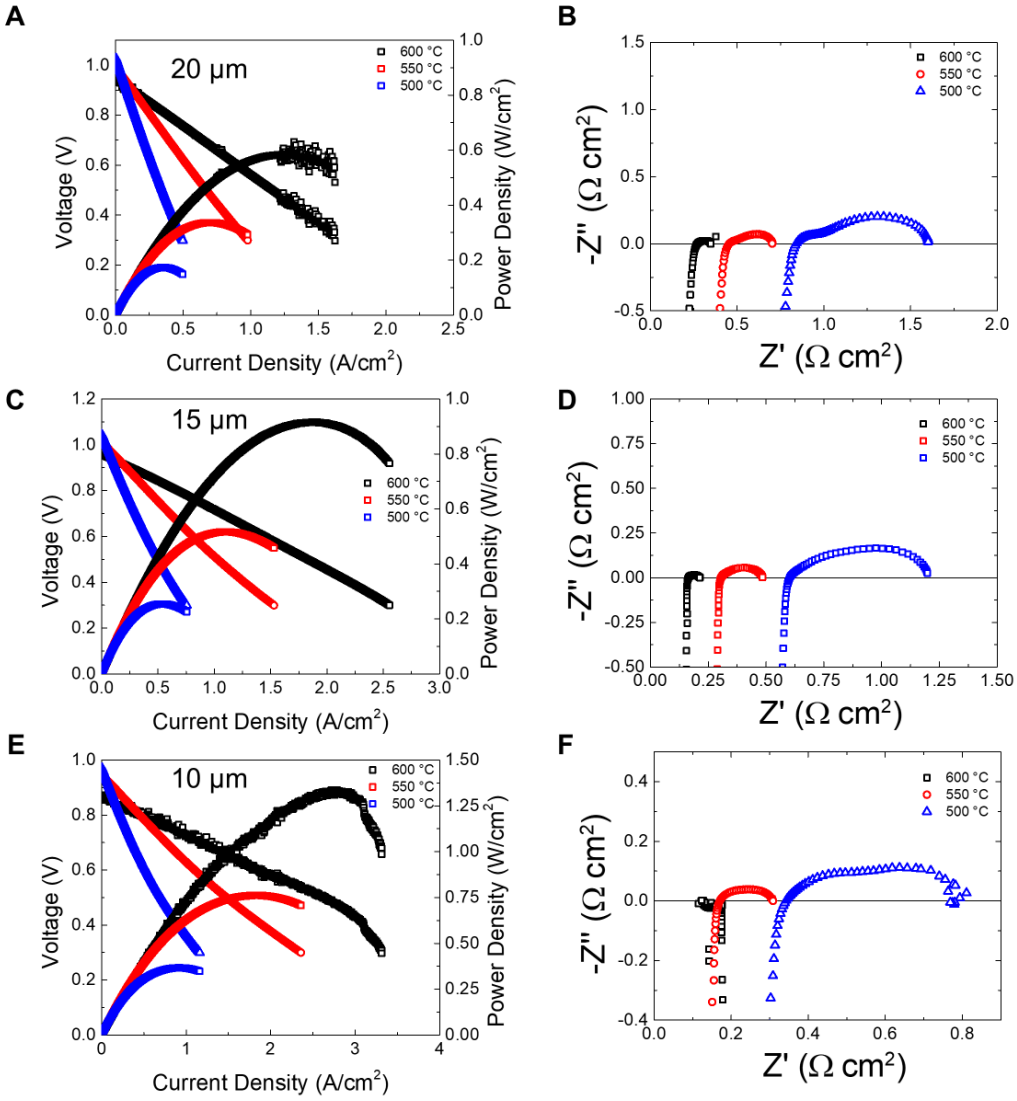

Figure 4.9 Cell Behavior IV and Impedance with varying DEL. A Temperature dependent iV of 20 µm thick DEL with 10 µm thick 0.5wt% Pr-GDC PFL **B** corresponding temperature dependence of cell shown in **A**. **C** and **D** Respective iV and EIS of 15 µm thick DEL with 10 µm thick 0.5 wt% PFL. **E** and **F** Respective iV and EIS of 10 µm thick DEL with 10 µm thick 0.5 wt% PFL.

The composition of the PFL was varied to understand its effect on OCV and performance in the full cell. The summary of the results is depicted above in Figure 4.4, showing that 0 wt% Pr, or porous GDC, has the highest overall OCV but slightly lower activity that 0.5 wt% Pr-GDC. Each tested cell at each temperature is shown in Figure 4.10 to fully understand the performance of each PFL composition. The specific

application could dictate which PFL to use. If a high faradaic efficiency SOEC is the desired application, it may be advantageous to use the PFL with 0 wt% Pr. However, if the cell is to purely operate as a SOFC, then the 0.5 wt% Pr configured PFL is the optimal choice because it has lower ASR losses when operating as an SOFC. 10 μm thick DEL configured cells were chosen to minimize the ohmic ASR of the Ni-GDC/GDC cells. Each composition of PFL was applied to the sample and tested with the configuration of Ni-GDC/GDC/PFL/SSC-GDC. The performance at 600 °C for each cell is about 1 W/cm^2, 1.3 W/cm^2, and 0.5 W/cm^2 for the 0 wt%, 0.5 wt%, and 5 wt% Pr-GDC respectively. The ohmic losses for each configuration are about 0.1-0.15 Ωcm^2 at 600 °C. However, the non-ohmic loss is about 0.1, 0.1 and 0.2 Ωcm^2 respectively at 600 °C. The 0.5 wt% Pr-GDC configuration was tested twice to verify the result shown in Figure 4.9 and Figure 4.10. Microstructural differences between each of the PFLs could cause the activity differences between the different compositions.

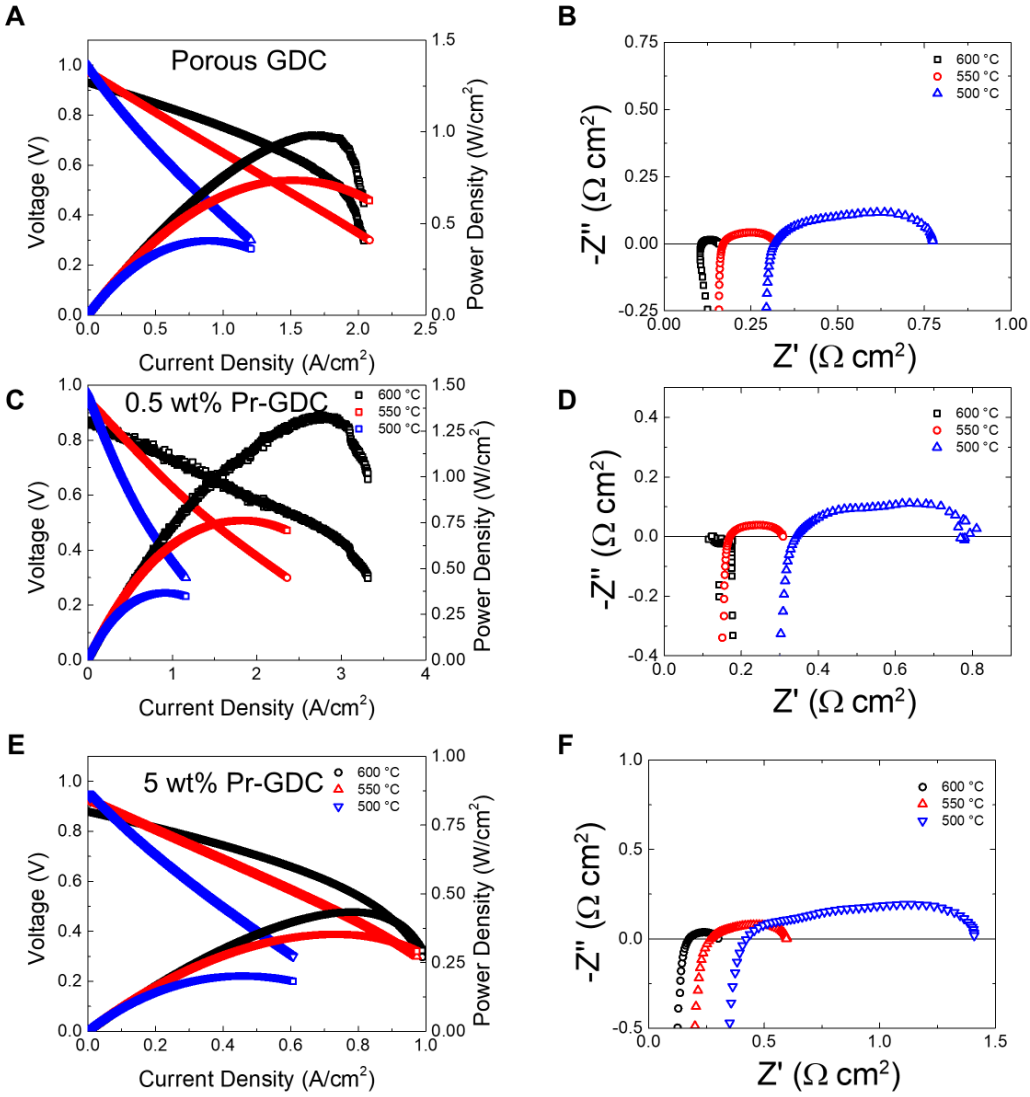

Figure 4.10 Cell Behavior IV and Impedance with varying PFL Composition A Temperature dependent iV of 20 µm thick DEL with 10 µm thick Porous GDC PFL **B** corresponding temperature dependence of cell shown in **A**. **C** and **D** Respective iV and EIS of 10 µm thick DEL with 10 µm thick 0.5 wt% PFL. **E** and **F** Respective iV and EIS of 10 µm thick DEL with 15 µm thick 5 wt% Pr-GDC PFL.

The microstructure for each of the configured cells for both the DEL and composition of the PFL study is depicted in Figure 4.11. A, B, and C show the DEL variation with a 0.5 wt% Pr-GDC PFL, and D, E, and F show the microstructural variation of the PFL on a Ni-GDC/GDC pristine cell. The microstructure of the different PFL compositions reveals that the 5 wt% Pr-GDC densifies compared to the

0.5 wt% and 0 wt % Pr-GDC. The densification could result in a decrease in cathode-PFL TPB length compared to the other two compositions and thus a lower activity. This result is supported by the high non-ohmic ASR of the 5 wt% Pr-GDC PFL compared to the 0 at 0.5 wt% Pr-GDC PFLs.

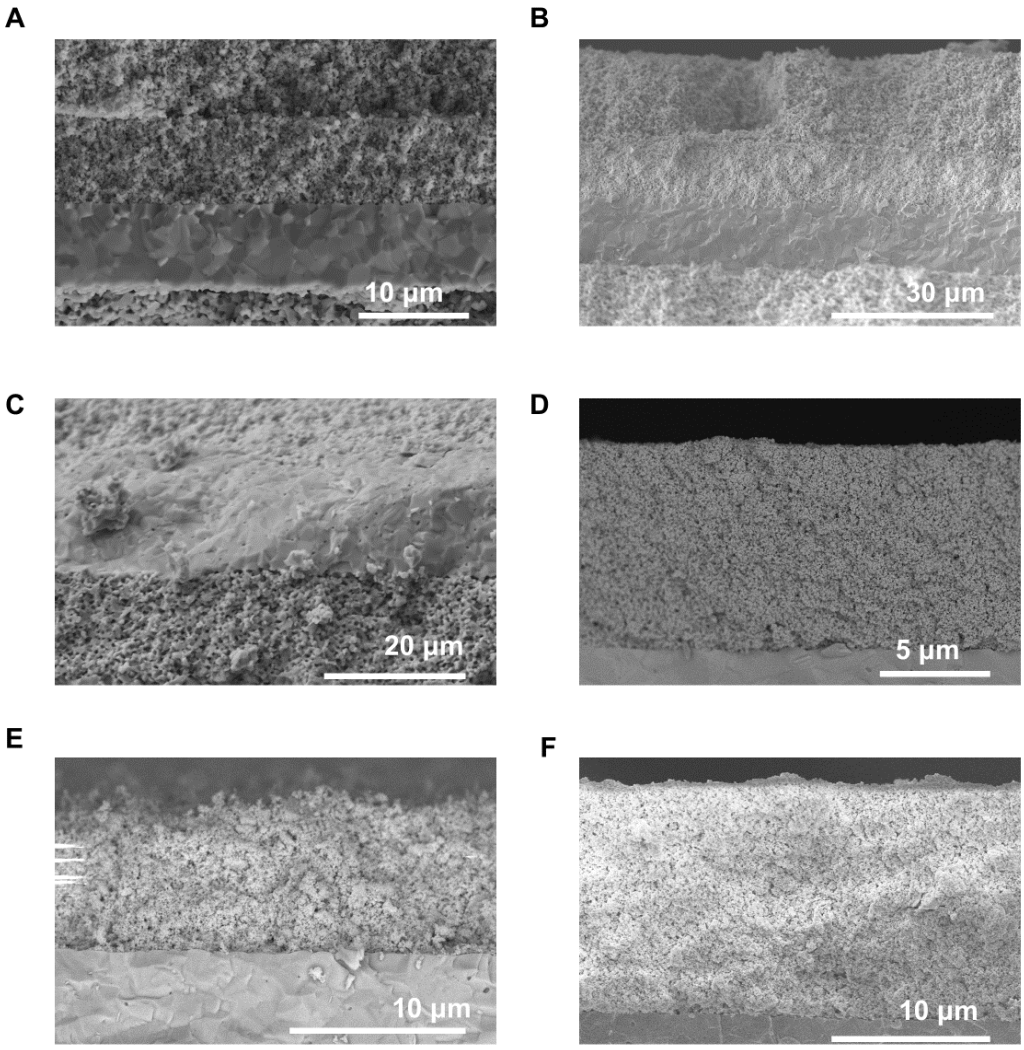

Figure 4.11 SEM images of Different Cells varying Electrolyte thickness and PFL Composition. A ~10 µm thick DEL 10 µm thick 0.5 wt% Pr-GDC PFL **B** ~ 15 µm thick DEL 10 µm thick PFL 0.5wt% Pr-GDC PFL **C** 20 µm thick DEL cell 10 µm thick 0.5 wt% Pr PFL. **D** 10 µm thick, porous GDC PFL **E** 10 µm thick, porous 0.5 wt% Pr-GDC PFL **F** 15 µm thick 5 wt% Pr-GDC PFL. **D**, **E**, **F** were coated on untested Ni-GDC/GDC cells for SEM images in the same procedure used for all cells tested in the study.

Symmetric cells were also aged to understand the durability of the PFL configured cathode system. Symmetric cells were aged at both 500 °C and 600 °C in air and the results are shown in Figure 4.12. The symmetric cells aged at both 500 °C and 600 °C containing the 0.5wt% Pr-GDC PFL appear to be the most stable. The total ASR is 0.9 and 0.2 Ωcm^2 for the majority of each test at 500 °C and 600 °C respectively. Pr infiltration on the SSC-GDC/PFL structure appears to further add activity and stabilize the system as the electrode ASR is 0.15 Ωcm^2 for the duration of the test. The breaks in the graph are due to communication issues with the solartron program.

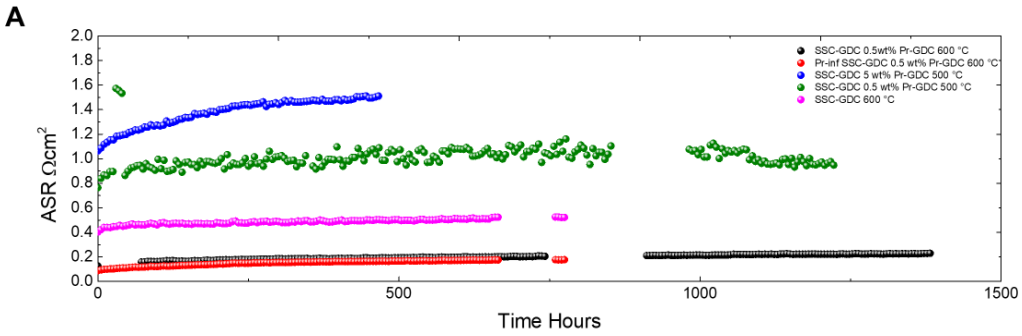

Figure 4.12 Aging of symmetric cells with different cathode and PFL compositions.

All cells used in this study are shown in Figure 4.13 below. Table 4.1 shows the key for the cells shown in Figure 4.13 by corresponding the cell number from the table, the respective aging condition, and the studied parameter. Figure 4.13 A shows the overall galvanostatic aging at 0.2 A/cm^2 for each cell tested. Figure 4.13 B shows the PPD vs time for the cells aged in the study. The cell configuration of Pr SM SSC-GDC/PFL/GDC/Ni-GDC showed remarkable performance as explained earlier and was aged for over 2000 hours. The Pr infiltration adds additional activity to the cathode, allowing the cell to operate at a 50 °C lower temperature. In Figure 4.13 C, the electrode ASR for each cell configuration is shown and highlights the cells with Pr infiltration

that have the lowest electrode ASR as explained in Chapter 3. The stability of each of the cells is to be noted as none of the cells experienced major degradation within the first 100 hours as cells shown in Chapter 3 at 600 °C. This could be due to the PFL preventing decomposition of the cathode at the electrolyte-cathode interface because of the higher pO_2 at the PFL-cathode interface. As the cathode in a traditional configuration experiences a much lower relative pO_2 compared to the cathode-PFL configuration, the perovskite cathode could be a driving force for cation segregation in the cathode. The ohmic ASR for each aged cell is shown in Figure 4.13 D. The ohmic ASR does not appear to increase in any of the cells tested in this study. This could also indicate a lack of cation segregation as cation segregation typically produces SrO in the cathode which is considered to be insulating.

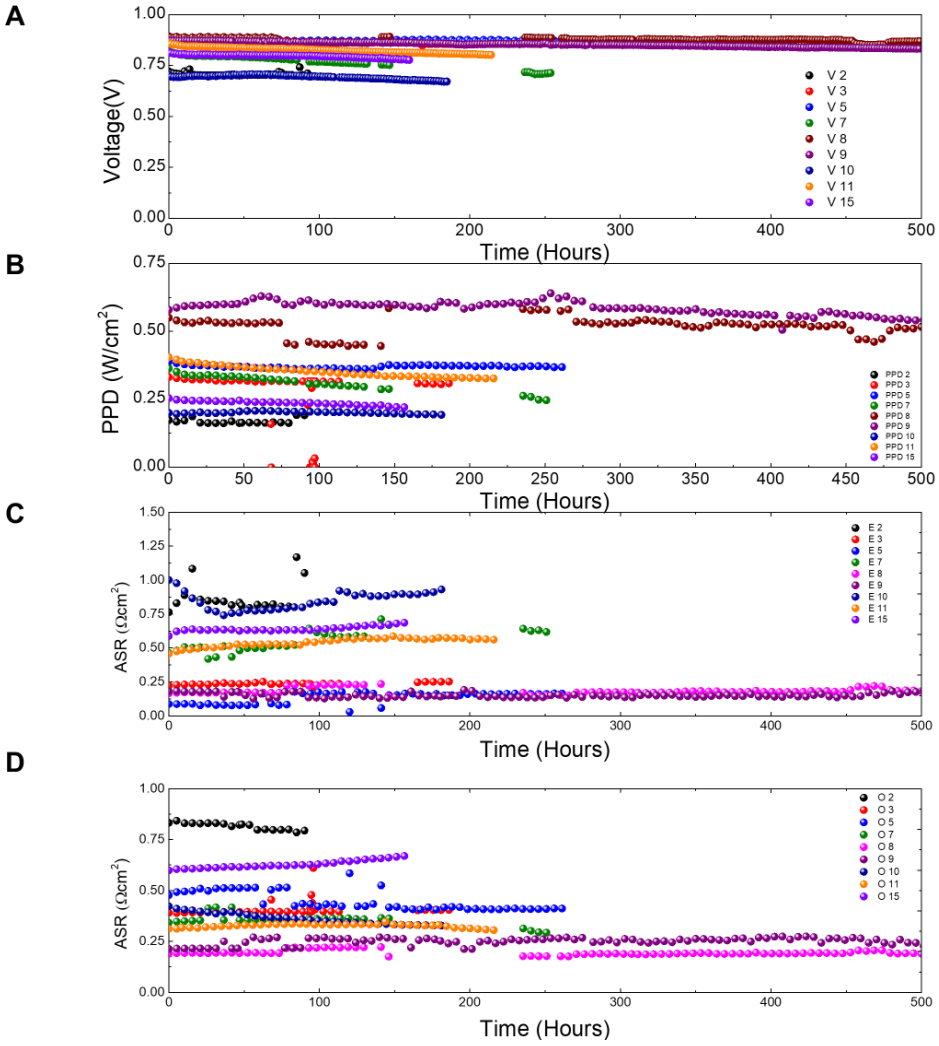

Figure 4.13 aging of all cells used in this study see Table 4.1 for configuration of cells. A Galvanostatic aging at 0.2 A/cm^2. **B** Peak power density from iV behavior taken every 5 hours. **C** Electrode ASR from EIS taken at OCV every 5 hours. **D** Ohmic ASR from EIS taken at OCV every 5 hours.

Table 4.1 Key for aging data in Figure 4.13

Parameter Studying	Cell #	DEL (µm)	PFL Thickness (µm) /Composition	Cathode	Aging Temp
DEL thickness	2	20	10 (0.5wt% Pr-GDC)	SSC-GDC	500 °C
DEL thickness	7	10	10 (0.5wt% Pr-GDC)	SSC-GDC	500 °C
DEL thickness	9	10	10 (0.5wt% Pr-GDC)	SSC-GDC	550 °C
DEL thickness	15	15	10 (0.5wt% Pr-GDC)	SSC-GDC	500 °C
DEL Thickness and Cathode SM	3	20	10 (0.5wt% Pr-GDC)	Pr-SM SSC-GDC	500 °C

DEL Thickness and Cathode SM	5	15	10 (0.5wt% Pr-GDC)	Pr-SM SSC-GDC	500 °C
DEL Thickness and Cathode SM	8	10	10 (0.5wt% Pr-GDC)	Pr-SM SSC-GDC	500 °C
PFL Composition	7	10	10 (0.5wt% Pr-GDC)	SSC-GDC	500 °C
PFL Composition	10	10	15 (5 wt% Pr-GDC)	SSC-GDC	500 °C
PFL Composition	11	10	10 (Porous GDC 0wt% Pr)	SSC-GDC	500 °C

4.3 Conclusion

We address the critical electronic conduction issue in ceria-based low-temperature electrolyte by engineering associated defects through external structure design. The porous design of the PFL pins the oxygen chemical potential at the PFL-DEL interface to equilibrate with air, pO_2=0.21atm and, therefore, limits Ce reduction. Based on this concept, we report high performance LT-SOFCs over 0.55 W/cm^2 at 500 °C with over 2000 hours of durability with negligible performance losses using all scalable ceramic fabrication techniques. This PFL layer drastically increases efficiency as well as cathode activity, allowing SOFCs to operate at a much lower temperature. This work demonstrates how fundamental defect engineering can significantly impact a SOFC at a device level and sheds lights on the future of low-temperature electrochemical cell design.

4.4 Supporting Experimental not Discussed in Chapter 2

PFL layers were made by the same process as the cathode ink, Pr_6O_{11} powder (Sigma Aldrich), and GDC (Fuel Cell Materials). PFL or SSC-GDC cathode ink was then deposited onto the Ni-GDC/GDC half-cells using a screen-printing method using a 0.31cm^2 active area cathode. The cathode and PFL were then cofired at 950 °C for

two hours. Electrolyte supported cells were used to complete the transference number measurement study and tape cast GDC supports (200-300 μm) were sintered at 1450 °C for four hours. Ni-GDC (48% NiO- 52% GDC) ink, made using the same method as the cathode ink, were applied to the cell and sintered at 1200 °C for two hours. SSC-GDC/PFL was applied to the opposite side and sintered at 950 °C for two hours. Hitatchi SU-70 with X-ray Energy Dispersive spectrometer was used to acquire SEM images and EDX spectra. TESCAN XEIA FIB-SEM was used to gather ToF-SIMS data from the PFL-Electrolyte support.

Chapter 5. Scaffold Infiltrated Cathode for Low-Temperature Solid Oxide Fuel Cells

5.1 Introduction

Electrocatalyst infiltration is a common approach to enhance cathode activity and introduces active electrocatalysts on an existing cathode surface, i.e. $La_{1-x}Sr_xCo_{1-y}Fe_yO_{3-\delta}$ (LSCF), $La_{1-x}Sr_xMnO_{3-\delta}$ (LSM), or $Sm_{0.5}Sr_{0.5}CoO_{3-\delta}$ (SSC) among others.[48,52,81–83] Although this approach improves performance, stability is still a concern because of the effect of adding multiple elements. In addition, since the infiltration is the main provider of catalytic activity, the use of scarce cathode elements as backbone support is a waste of material.[21,23,48,52,54,81] Specifically, cobalt, a necessary element for state-of-the-art cathodes, is toxic, expensive, and scarce due to its widespread use in batteries.[84]

Another approach is infiltrating electrocatalysts onto a scaffold of electrolyte materials, namely $Ce_{1-x}Gd_xO_{2-\delta}$ (GDC), $Ce_{1-x}Sm_xO_{2-\delta}$ (SDC), or $Zr_{1-x}Y_xO_{2-\delta}$ (YSZ).[81,82,85] This approach seems to be promising as it limits the material waste and simplifies cathode compositions, but issues remain as the electrolyte scaffolds lack the electronic conductivity necessary to facilitate the electrochemical reactions and rely on the connectivity of the infiltrates to establish continuous electronic conducting pathway.

Here we demonstrate that by solely infiltrating multiphase electrocatalysts in mixed ionic electronic conducting (MIEC) doped ceria scaffold, a low cathode area specific resistance (ASR, $< 0.25\ \Omega cm^2$) and high peak power density (PPD $> 1\ W/cm^2$)

on a full cell level are achieved at 550 °C. We engineered a MIEC scaffold with enhanced electronic conductivity and a conductive network of active nanoparticles to function as the electrocatalyst. The combination of the scaffold and nanoparticle approach allows for operation temperatures below 550 °C, and demonstrates the high stability of this cell design for over 500 hours.

5.2 Results and Discussion

Our approach is facile and scalable because it uses traditional ceramic processing techniques and minimizes the amount of high temperature processing steps (T > 1000 °C). First, only one high temperature sintering step is used to sinter the Ni-GDC anode-supported GDC electrolyte half-cells that are produced by roll-roll processing techniques (Figure 5.1 A). Then, the cathode scaffold is produced by a scalable method such as blade coating and is sintered below 1000 °C (Figure 5.1 B). The electrocatalysts are deposited into the scaffold to form the final produced cell in Figure 5.1 C.

Based on the previous work from Chapters 3 and 4, the Pr-Sr-Co (PSC) type was selected for the specific electrocatalysts.[48] Results of symmetric cell testing of a PSC mixture on GDC scaffolds are shown in Figure 5.1 D-G. The Nyquist plot at 550 °C in Figure 5.1 D shows the optimal scaffold firing temperature of 950 °C for the GDC scaffold as the cathode ASR is 0.25 Ωcm^2, which is about a 50~75% decrease compared to the scaffolds fired at higher temperatures. The scaffold sintering temperature effects are summarized in Figure 5.1 E, which shows a reverse volcano behavior with the lowest ASR at 950 °C. Below 950 °C, the poor sinterability leads to a higher ASR

while above 950 °C, the ASR increases, which could be due to the densification of the scaffold, reducing the TPB length.

To further elucidate the perceived mechanism for the infiltrated scaffold (black) versus conventional composite (red), distribution of relaxation time (DRT) analysis was performed in Figure 5.1 E.[43] The major peaks are labeled P1-P3. P1 and P2 contribute to the majority of the losses in the infiltrated case because of its limited electronic conduction pathway. P3, typically attributed to the surface exchange reactions, is where the PSC infiltrated scaffold shows the most significant improvement in losses compared to the SSC-GDC cell with a reduction of 98% in peak intensity.[28,47,56,86] Figure 5.1 G shows the schematic of a two-step oxygen transport mechanism based on the DRT results. In composite cathodes, the dissociative adsorption of oxygen (Step 1) occurs on the cathode surface but requires a long transport distance (Step 2), which limits the number of active sites.[78] In contrast, in the infiltrated case, the nanoscale electrocatalysts provide a larger number of active sites for oxygen surface exchange as well as a shorter diffusion length between the nanoscale PSC and nearby GDC scaffold, leading to the magnitude of reduction in associated energy losses, which is clearly shown in the change in P3 in DRT analysis.

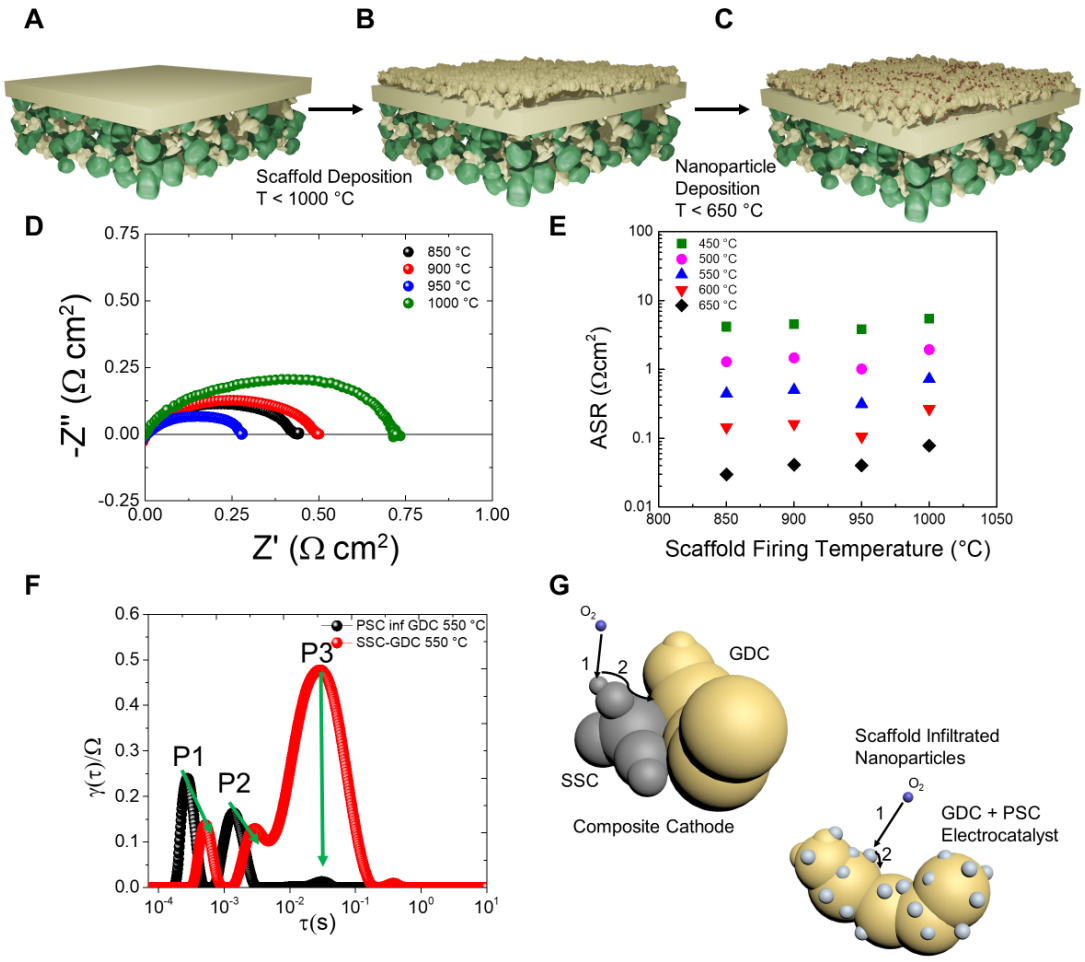

Figure 5.1 Scaffold Infiltrated SOFC Design, manufacturing, and Analysis. A Ni-GDC half-cell sintered at 1450 °C produced by tape-casting and roll lamination. **B** Ceria-based scaffold deposited and sintered to half-cell at 950 °C. **C** Final cell design with electrocatalyst infiltration T < 650 °C. **D** Nyquist plot at 550 °C of Pr-Sr-Co (PSC) infiltrated symmetric cells for all scaffold sintering temperatures screened. **E** ASR vs scaffold sintering temperature. **F** DRT comparing traditional SSC-GDC composite cathode (red) and PSC infiltrated GDC (black). **G** Proposed mechanism of improvement between traditional composite cathode and the scaffold infiltrated cathode.

The effect of scaffold temperature is shown in detail below in Figure 5.2 (Nyquist) and Figure 5.3 (DRT) and highlights that the 950 °C scaffold sintering temperature has the lowest losses in the intermediate time constant regime (10^{-3}-10^{0}) compared to the other sintering temperatures. The scaffolds sintered at 850 °C and 900

°C have similar losses in the low time constant regime or peaks 1 and 2 from Figure 5.1. The intermediate time constant regime reveals that the peak losses are actually slightly larger than the scaffold sintered at 950 °C, which could be due to a poor contact between the scaffold and GDC electrolyte because of the low sintering temperature. The scaffold sintered at 1000 °C has high losses in the intermediate time constant regime as which could be due to the densification of the scaffold-limiting TPB length.

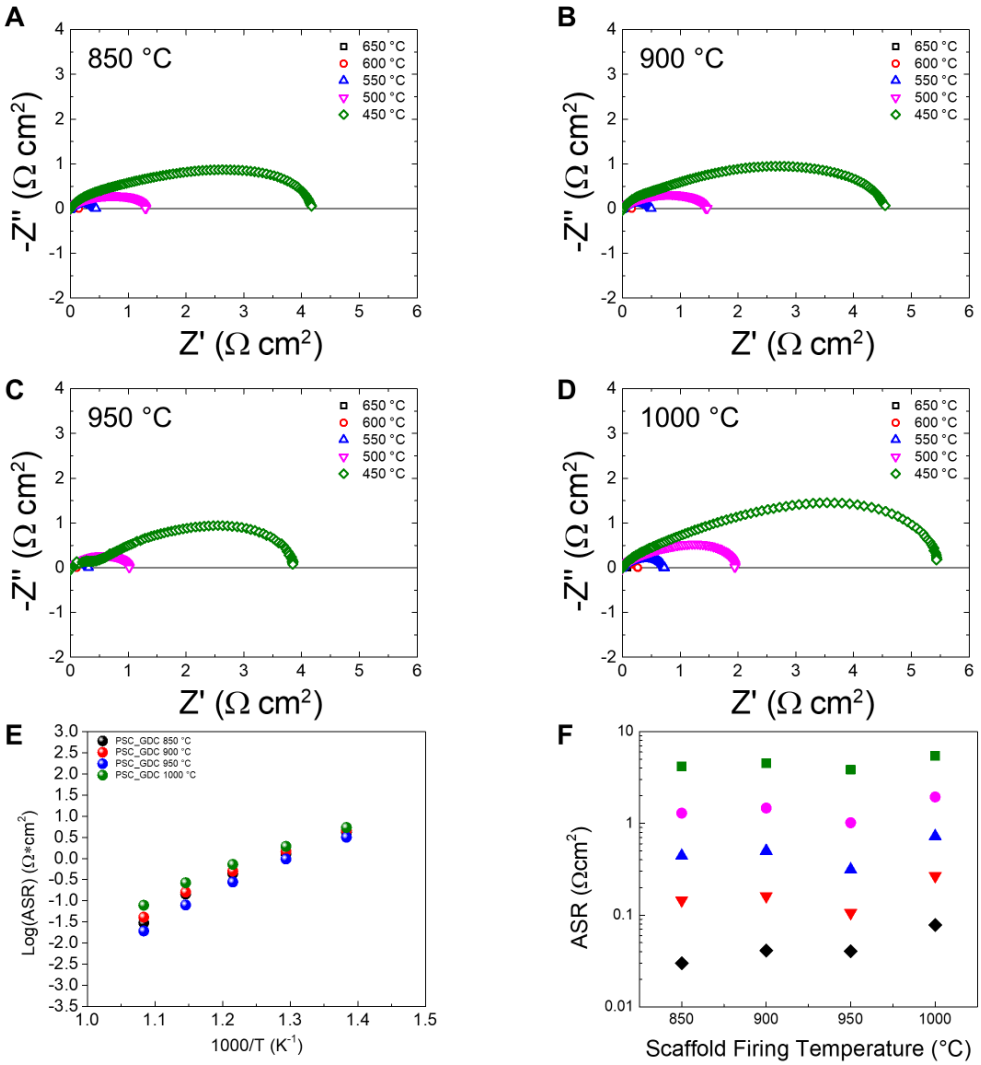

Figure 5.2 EIS of PSC infiltrated GDC, GDC Scaffold Sintering Effect. PSC infiltrated GDC scaffold symmetric cell, GDC scaffold sintered at **A** 850 °C, **B** 900 °C, **C** 950 °C, and **D** 1000 °C. **E** Arrhenius plot of area specific resistance (ASR) of all

cells in sintering scaffold temperature dependence from 450 °C- 650 °C in 50 °C intervals. **F** ASR vs scaffold sintering temperature, color is the same as the Nyquist plots in the keys for **A-D.**

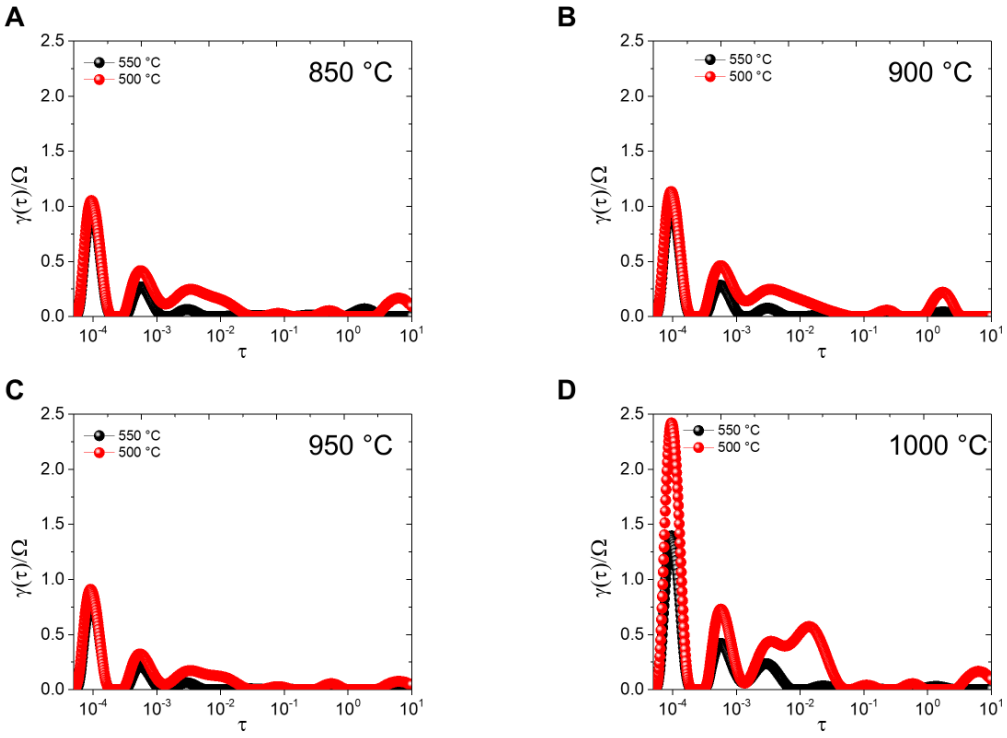

Figure 5.3 DRT of Symmetric Cells at 550 °C and 500 °C. DRT of symmetric cell shown in Figure 5.2 A. All DRTs correspond to their respective symmetric cell from Figure 5.2.

Effect of MIEC GDC scaffolds is demonstrated in Figure 5.4, as different ceria-based scaffolds as well as different PSC loadings are integrated into full cells. Current-voltage (iV) and EIS at 550 °C are shown in Figure 5.4 A and B, respectively. For the pure GDC scaffold, the polarization resistance is only 0.25 Ωcm^2, but the low electronic conductivity of cathode leads to a high ohmic ASR of 1.25 Ωcm^2, limiting the PPD to only 175 mW/cm^2. The apparent ohmic losses due to the GDC scaffold at 550 °C are

approximately ~1 Ωcm^2. Comparing previous results, a 20 μm dense GDC electrolyte typically contributes ~0.2 Ωcm^2 at 550 °C as ohmic ASR.

With the increase in Pr_6O_{11} doping levels in GDC scaffold and PSC electrocatalysts loading, the cell performance drastically improves. The effect of Pr and Sm doping in GDC scaffold on ohmic ASR is summarized in Figure 5.4 C. As the Pr/Sm loading increases, the ohmic ASR of full cells (20 μm GDC) decreases, suggesting the electronic conduction of doped GDC increases. For the case of 0.5 wt% Pr_6O_{11} doping level, the ohmic ASR decreases from 1.25 Ωcm^2 to 1.1 Ωcm^2 and further decreases to 0.5 Ωcm^2 with 5 wt% Pr_6O_{11}. Comparing the three cycle PSC 5Pr-GDC scaffold to the 5-5-90 Pr-Sm-GDC scaffold, the ohmic ASR is 0.3 and 0.24 Ωcm^2 at 550 °C respectively. The 5Pr-GDC cell has a slightly higher peak power density compared to the 5-5-90 Pr-Sm-GDC cell, suggesting that the higher Pr doping level may work as a sintering aid, causing scaffold densification and changing the microstructure. These results suggest the doping in GDC scaffold can vary the MIEC, leading to a lower ohmic ASR and a higher performance.

The infiltration loading effect is summarized in Figure 5.4 D. The electrode ASR (black) decreases once the loading increases as a result of increasing active sites. In addition, the ohmic ASR decreases from 0.5 Ωcm^2 to 0.25 Ωcm^2 with increasing infiltration loading, one cycle vs three cycles, likely due to the increase in connectivity of surface conductive PSC electrocatalyst or the doping of infiltrates in the scaffold. The decrease in ohmic ASR aides in the increase of PPD from 0.22 W/cm^2 with one infiltration cycle of PSC to 0.5 W/cm^2 at 550 °C with three infiltration cycles. The PSC begins to agglomerate once loading is over three infiltration cycles (Figure 5.16).

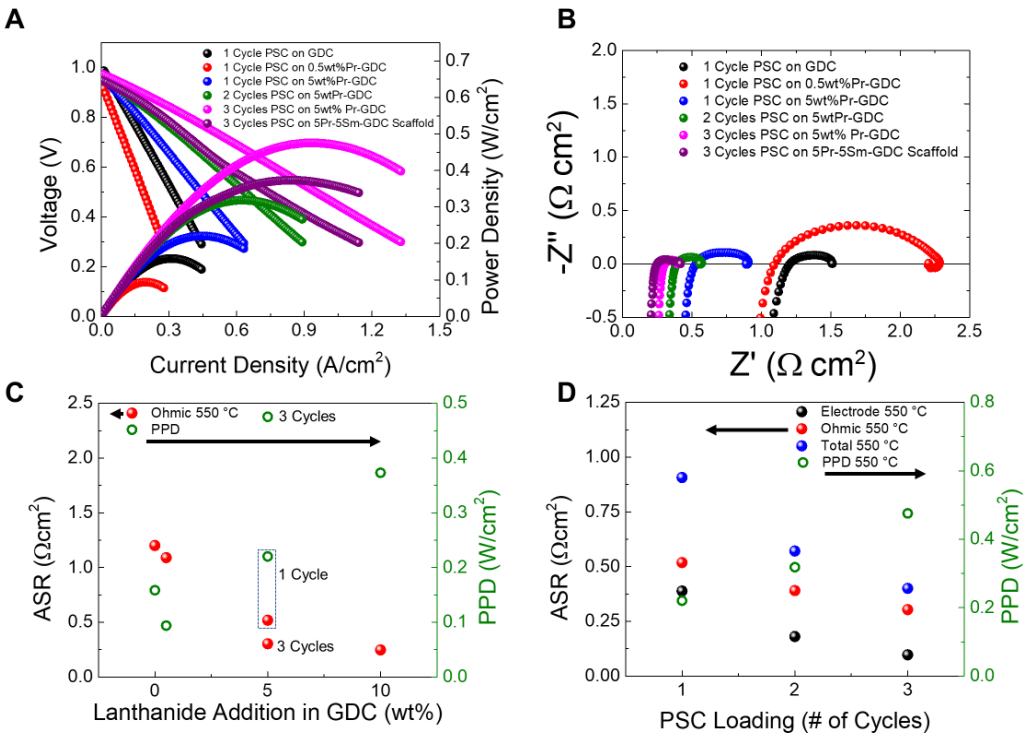

Figure 5.4 MIEC Scaffold Effect on SOFC Performance. A iV plot of scaffold optimization with varied scaffold composition and loading at 550 °C in 97% H_2/3% H_2O and air, and **B** EIS spectra. **C** Summary of ASR (closed circles, left axis) and PPD (open green circles, right axis) for the composition loading of Pr in the Pr-GDC cathode scaffold with 1 cycle of PSC loading. Note that there are 2 data sets for the 5Pr-GDC scaffold as the loading cycle study was performed on that composition. The 10 wt% in **C** has 3 cycles of PSC infiltration where others have 1 cycle of PSC infiltration unless noted. **D** Summary of ASR (closed circles, left axis) and PPD (open green circles, right axis) at 550 °C based on PSC loading of 5wt% Pr-GDC cathode scaffold. The fully integrated cell consists of a porous GDC scaffold infiltrated with PSC ~20μm, a dense 20 μm GDC electrolyte, a 20 μm Ni-GDC anode functional layer (AFL), and a 500 μm Ni-GDC anode support.

Pr-Co-based infiltrates are used in this study because previously, we demonstrated their high activity.[28,46,52,56,86] Different infiltrates were screened based on different targeted Pr-Co based phases (Figure 5.17). The high temperature X-ray diffraction (HT-XRD) was performed on PSC pretreated at 650 °C to identify active phases at different temperatures, as shown in Figure 5.5 A. There are no significant phase changes while heating up the powders from room temperature to 650 °C. With

an initial 1:1:2 ratio of Pr, Sm, and Co metal cations, multiple phases, including $PrO_{2-\delta}$. Co_3O_4, and $SrCoO_{3-\delta}$, are co-existing once calcined, and apparently the majority phase is $PrO_{2-\delta}$. [87–89] These multiple phases lead to the low ASR in Figure 5.1 and Figure 5.4. Our results suggest that the co-existing of these multiple phases is the key for high electrochemical performance.

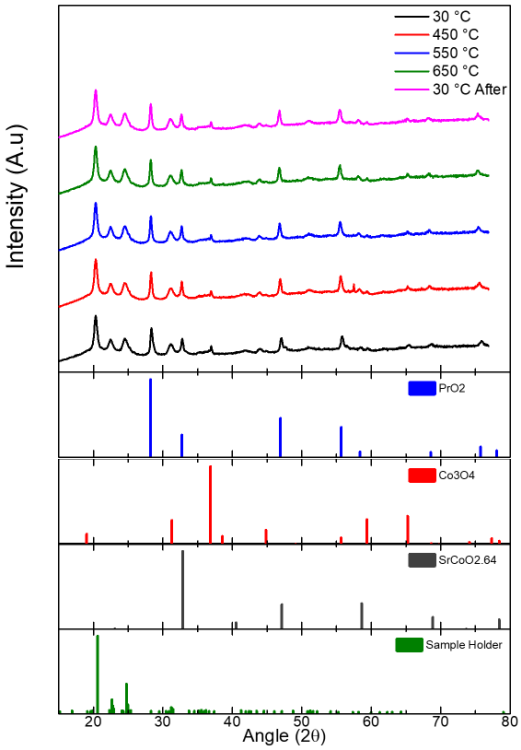

Figure 5.5 *in situ* characterization of PSC electrocatalysts. HT-XRD from room temperature to 650 500 °C. Diffraction patterns of PrO_2, Co_3O_4, $SrCoO_{2.64}$, and the sample holder is also shown.

The result of the high performing PSC 5-5-90 Pr-Sm-GDC is shown in Figure 5.6 and the detail of scaffold porosity optimization is shown in Figure 5.15. The increase in porosity provides larger electrocatalysts/scaffold interfaces and resolves the mass transfer limitation. As shown in iV curves, Figure 5.6 A, for the 20 μm GDC configured cell (black), the PPD is 0.85 W/cm^2 at 550 °C and the 10 μm cell (red)

shows a remarkable PPD of 1 W/cm^2 at 550 °C and 0.6 W/cm^2 at 500 °C. The cell impedance in Figure 5.6 B shows that the polarization impedance is only ~ 0.07 Ωcm^2 and the ohmic part is considered the major loss of the cell in both cases: 0.15 Ωcm^2 to 0.09 Ωcm^2 in the 20 μm vs 10 μm thick configuration respectively.

The microstructure of the aged 20 μm cell can be seen in Figure 5.6 C, and the infiltrates are on the order of 50-100nm after 500 hours of aging. The PSC electrocatalysts have high activity and durability, with nanoscale state preserved after 500 hours at 550 °C, which can be attributed to the deposition temperature. In this study, PSC nanoparticles only goes to T=650 °C whereas other groups have utilized much higher temperatures T > 800 °C.[25,26,90,91] Lee et al. showed that high temperature synthesized (800-1300 °C) $Pr_{0.4}Sr_{0.6}CoO_{3-\delta}$ onto a LSCF-SDC scaffold produces a cathode ASR of 0.15 Ωcm^2 at 750 °C. [83] In contrast, in this study, a multiple PrO_x, CoO_x, and $SrCoO_{3-\delta}$ phase mixture shows a low ASR of 0.25 Ωcm^2 at 550 °C with high durability.

The aging results of the 20 μm cell in Figure 5.6 C and D show that the majority of the performance drop occurs in the first 50 hours, likely because of the slight coarsening of PSC nanoparticle as the size grows from ~20nm to 100-200nm after 500 hours (SEMs in Figure 5.6 C and Figure 5.16 A). However, the long-term galvanostatic testing reveals very little degradation with the cell voltage decreasing from 0.9V to 0.8V over the 500-hour long test. PSC coarsening appears to be the main degradation mechanism as the overall electrode ASR changes from 0.07 Ωcm^2 (t = 0 hrs) to 0.11 Ωcm^2 (t= 50 hrs) and stabilizes to t= 500 hours Figure 5.6 D. The ohmic ASR observes the same trend and is likely the result of the loss in electronic connection because of

particle agglomeration. Note that the primary electronically conductive pathway for electrons is through the surface connectivity of the PSC infiltrates.

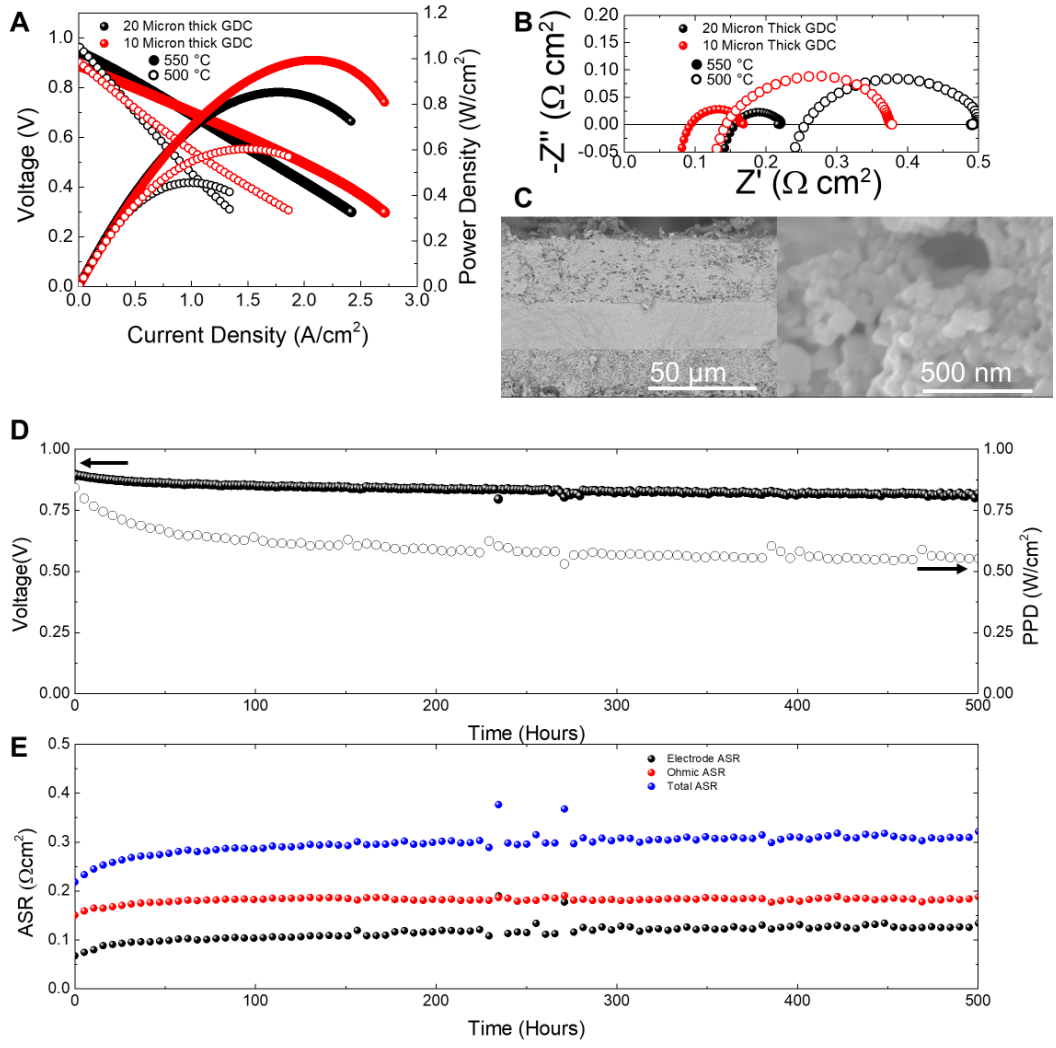

Figure 5.6 Performance and Durability of Infiltrated SOFCs. A iV curves for PSC-Pr-Sm-GDC cathode-scaffold configured cells with Ni-GDC anode and different GDC electrolyte thicknesses (10 µm, red, versus 20 µm, black) tested in H_2 at 550 °C (closed circles) and 500 °C (open circles), **B** corresponding EIS spectra. **C** SEMs of full cell and the cathode enlarged view showing the configuration of the scaffold/GDC (20µm) /Ni-GDC cell after 500 hours aging at 550 °C. **D** Long-term stability of the 20 µm electrolyte configured cell, showing galvanostatic at 550 °C (0.2A/cm^2) (left axis, closed circles) and PPD derived from iV curves (right axis, open circles). **E** Deconvoluted ohmic and electrode ASR vs time for the 20 µm GDC configured cell. The 10 µm GDC cell contains 15 wt% PMMA in the Pr-Sm-GDC scaffold and the 20 µm GDC cell contains 5 wt% PMMA in the Pr-Sm-GDC scaffold.

The performance of the loaded effect on GDC scaffold symmetric cells is shown in Figure 5.7 below. The symmetric cell results are not actually in agreement with the full cell results which could be due to the fact that the ohmic ASR is not considered in the symmetric cell measurement, only the electrode ASR is. The full cell results reveal that the scaffold does have an ohmic contribution to it but that is difficult to deconvolute on a symmetric cell level due to the thickness of the pellet compared to the scaffold (1500 μm vs 20 μm). However, the symmetric cell results do indicate that there is a saturation point of PSC loading in the GDC which appears to be about three infiltration loading cycles and the overall intermediate time constant regime appears to increase. This could be due to the oversaturation of the scaffold which would then limit the overall amount of reaction sites and gas diffusion, which could be explained by the slight peak at the high time constant regime (10^0-10^1) in the sample with 18 μL of PSC.

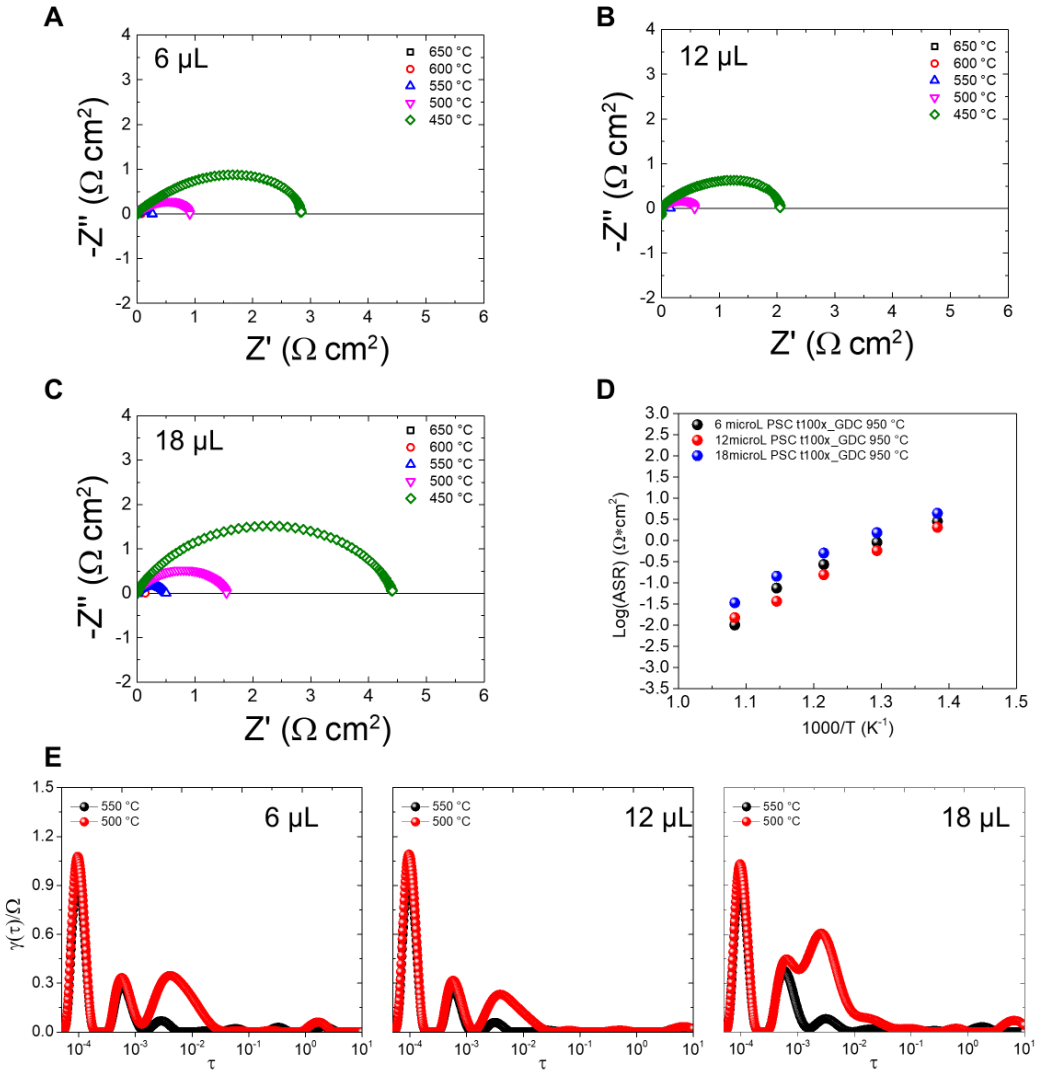

Figure 5.7 Nyquist plots and DRT PSC Loading Effect. PSC infiltrated GDC symmetric cell with **A** 6 µL, **B** 12 µL, and **C** 18 µL of PSC. **D** Arrhenius behavior of the PSC loading effect. **E** DRT corresponding to each loading composition. 1 Cycle is 6 µL.

This true infiltrate loading effect is shown in full detail in Figure 5.8 (iV) and Figure 5.9 (EIS) below on a full cell as a supplement to the summary of parameters shown in Figure 5.4. The increase in total loading reduces the ASR of the cell. This could be due to a greater connection of conductive PSC nanoparticles since the ohmic ASR seems to be significantly reduced in the 5Pr-GDC scaffold infiltrated with more

PSC. The ohmic ASR is close to 1 Ωcm^2 at 500 °C for the sample infiltrated with only 6 µL of PSC, while the sample infiltrated with 18 µL of PSC has an ohmic ASR of 0.5 Ωcm^2. This seems to also be the case at 650 °C where there is a ~50% reduction in ASR for the case of 18 µL of PSC infiltrate compared to only 6 µL. The iV results also indicate this effect because the PPD is roughly doubled at every temperature. The summary of the loading effect is seen in Figure 5.8 D.

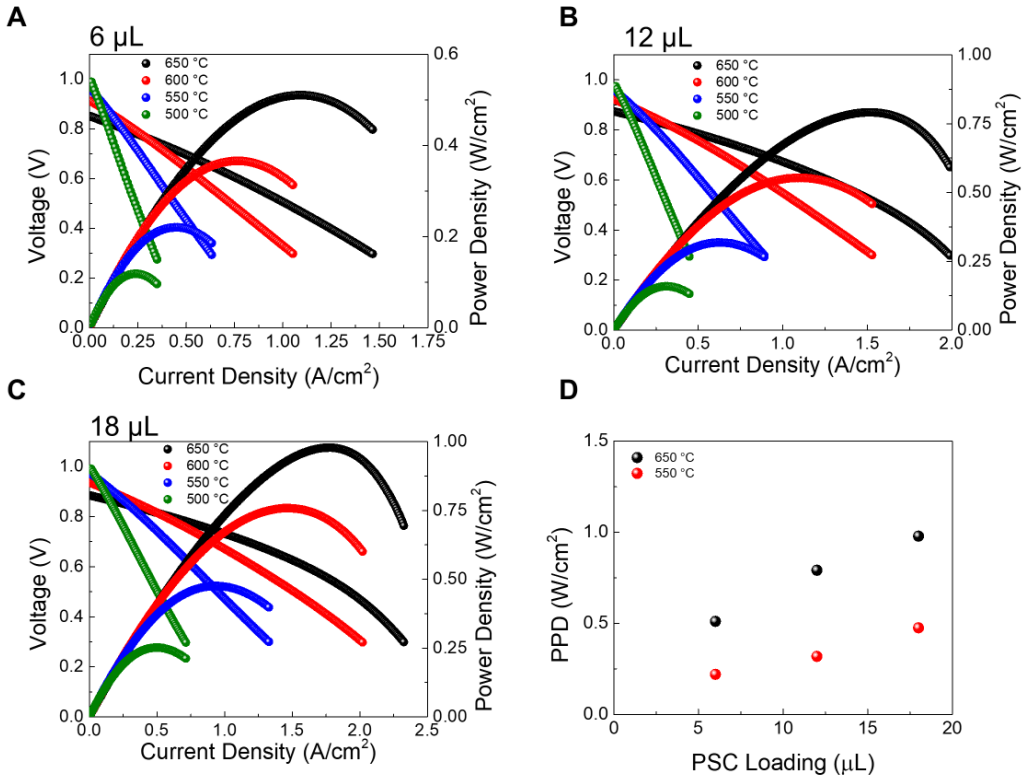

Figure 5.8 Cell Behavior iV and Impedance with Varying Infiltration Loading. A Temperature dependent iV of 5Pr-GDC scaffold infiltrated with 6 µL of PSC **B** 12 µL of PSC **C** 18 µL of PSC. **D** Summary of PPD vs PSC loading of 5Pr-GDC scaffold infiltrated Ni-GDC/GDC/5Pr-GDC full cells.

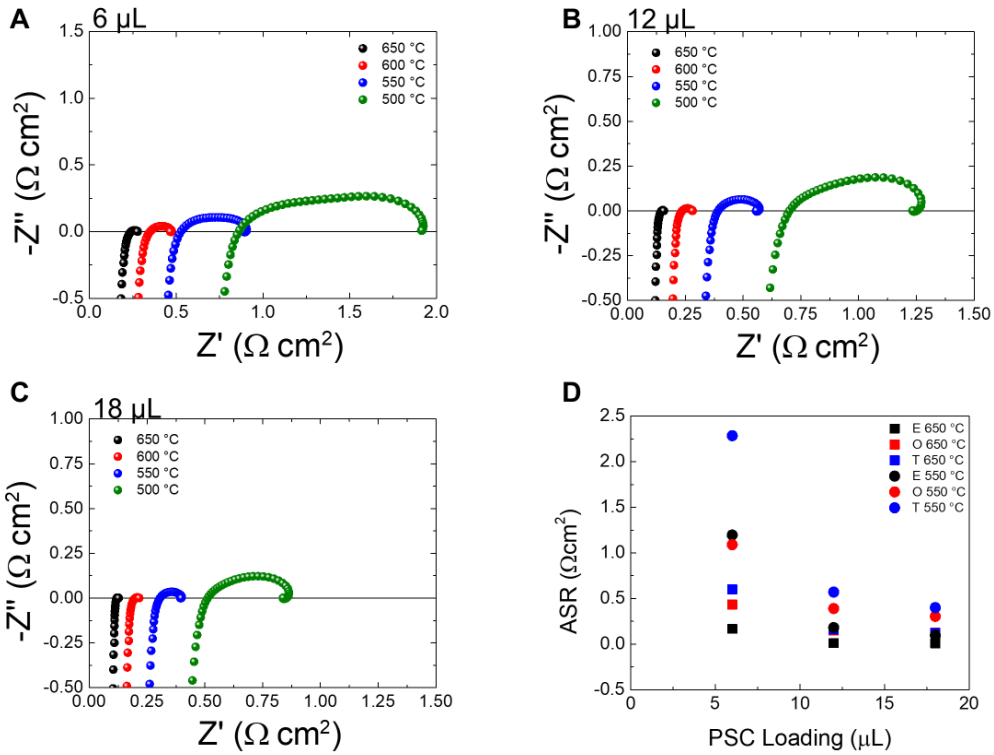

Figure 5.9 EIS with Varying Loading Concentration of PSC on 5Pr-GDC Scaffolds. Nyquist of **A** 6 µL, **B** 12 µL, and **C** 18 µL PSC. **D** ASR Summary of ohmic, non-ohmic and total ASR for each of the cells at 550 °C and 650 °C, highlighting decreasing ohmic ASR with increasing PSC loading.

In addition, the full comprehensive results of the effect of Pr in the Pr-GDC scaffold are shown in Figure 5.10 (IV) and Figure 5.11 (EIS) below with increasing Pr-GDC leading to a decrease in ohmic ASR as stated previously. The 5Pr-GDC scaffold seems to lower the total ASR when further compared to the 0.5Pr-GDC or the GDC. This is likely due to an increase in conductivity of the scaffold as explained previously. The scaffolds were infiltrated with 6 µL of PSC as the loading study was performed after the scaffold study. The total PPD increased from about 0.4 W/cm^2 to about 0.5 W/cm^2 at 650 °C for the GDC vs 5Pr-GDC.

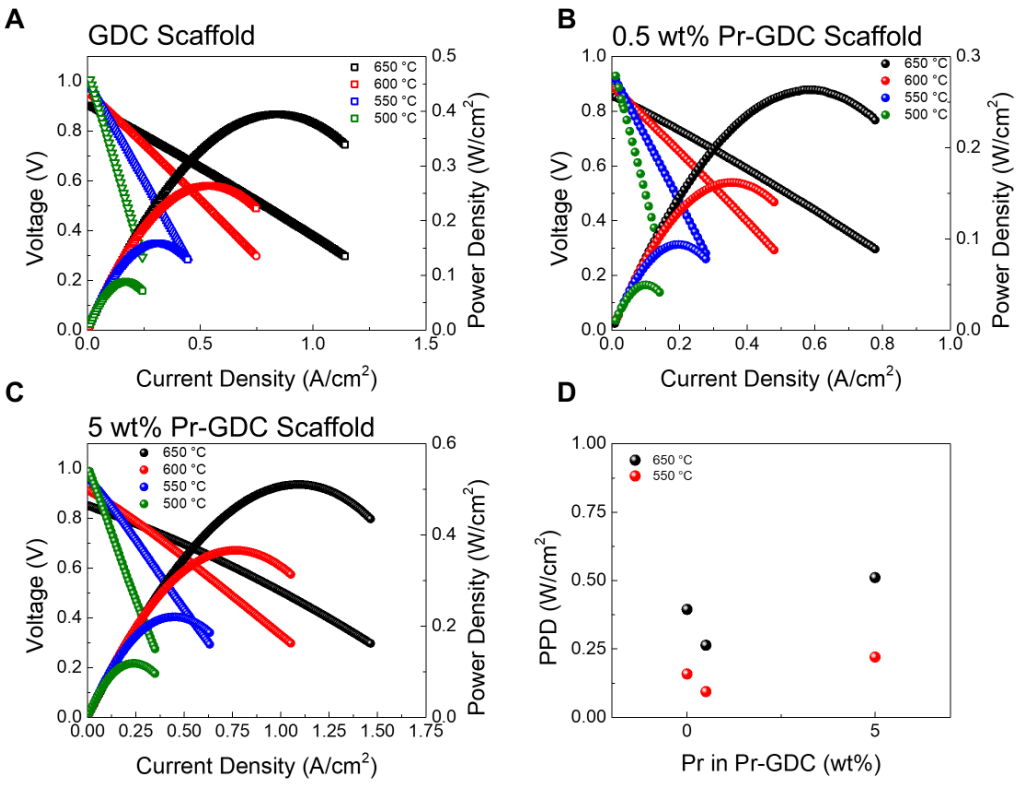

Figure 5.10 Scaffold Effect on Performance (iV). iV of **A** GDC scaffold, **B** 0.5wt% Pr-GDC scaffold, and **C** 5wt%Pr-GDC (5Pr-GDC) Scaffold. **D** PPD of cells tested at 550 °C and 650 °C. Each cell had 6 µL of PSC infiltrated into the respective scaffold. Cell configuration is Ni-GDC/GDC/Scaffold PSC infiltration.

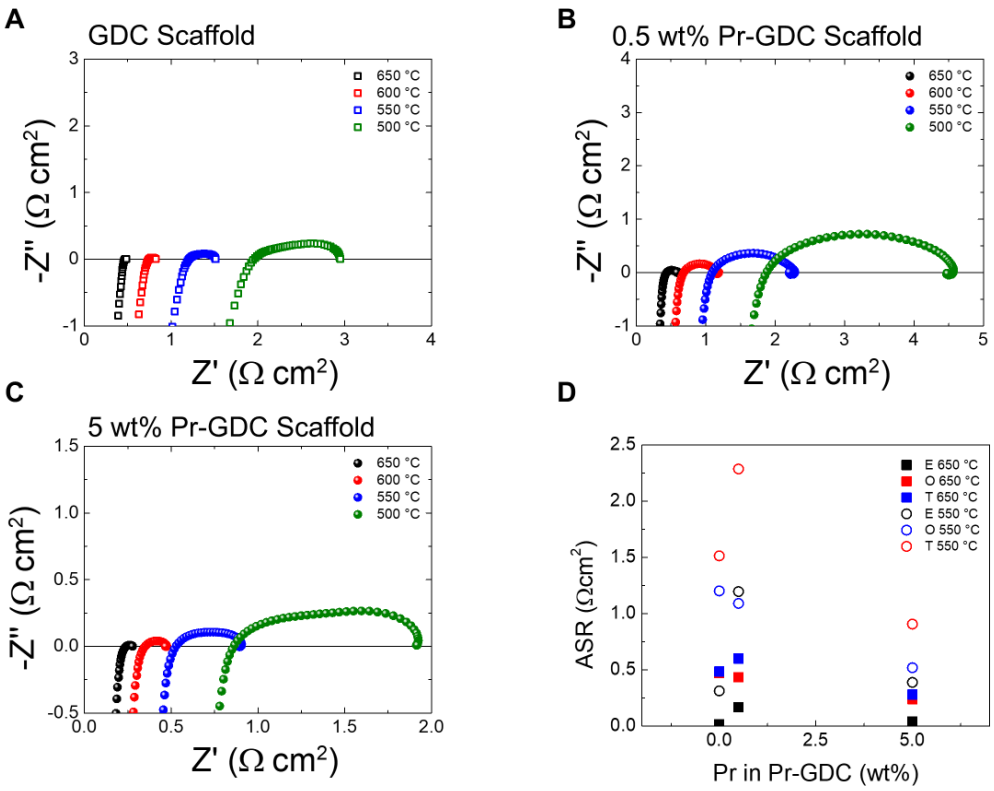

Figure 5.11 Scaffold Effect on Performance (EIS). A GDC, **B** 0.5wt% Pr-GDC, and **C** 5wt%Pr-GDC Scaffold. **D** Summary of each cell ohmic, non-ohmic, and total ASR. Cell configuration is Ni-GDC/GDC/Scaffold PSC infiltration.

The composition of the scaffold still did not seem to be conductive enough, because previous results, noted in Chapter 3, indicated that the ohmic losses of a 20 µm thick GDC electrolyte should be about 0.05-0.07 Ωcm^2 at 650 °C. The ohmic losses in the 5Pr-GDC scaffold infiltrated with 18 µL of PSC are about 0.1 Ωcm^2 so further work was done to increase the scaffold conductivity by adding Sm to the scaffold as explained previously. The Sm appeared to densify the scaffold slightly, so pore former was added to increase gas diffusion kinetics which may have been hindered in the densified 5-5-90 Pr-Sm-GDC scaffold. The full scaffold porosity study is shown below in Figure 5.12. The EIS curves indicate that without additional pore former, the infiltrate may not fully disperse in the scaffold. SEM results indicate the agglomeration

of PSC on the surface of the scaffold shown in Figure 5.15 as well as the ohmic resistance result seen in Figure 5.15 C. The ohmic resistance at 550 °C is 0.25 Ωcm^2 for the case with 0 wt% pore former whereas the scaffold with only 5 wt% pore former lowers the ohmic ASR to 0.13 Ωcm^2. This indicates the saturation point of PMMA loading has occurred by allowing the conductive PSC to reach the scaffold-electrolyte interface. Further pore former was added to decrease the cathode ASR but it had little effect. The 15 wt% PMMA scaffold did appear to have a lower quality sintering compared to the 5 wt% and 10 wt%. The post-sintering of the scaffold to cell observations revealed that the 15 wt% PMMA scaffold did not appear to have good contact with the cell, which could lead to delamination during operation. A void fraction calculation was performed by using an approximation of the density.[92] The density was estimated to be 7.8 g/cm^3, which was determined from an Archimedes measurement by sintering a 5-5-90 Pr-Sm-GDC pellet at 1450 °C. This composition was assumed to be fully dense at 1450 °C for four hours. A sample was sintered at 950 °C and a density measurement was taken via an Archimedes measurement revealing a relative density of 88% of the sample that was sintered at 1450 °C. For reference, the GDC10 density value is 7.2 g/cm^3 when sintered at 1450 °C. The total void fraction was then calculated by removing the total volume of PMMA added to the slurry vs the volume to the scaffold sintered at 950 °C. This calculation was performed to show that the necessary PMMA loading to increase the performance of the 5-5-90 Pr-Sm-GDC scaffold is minimal.

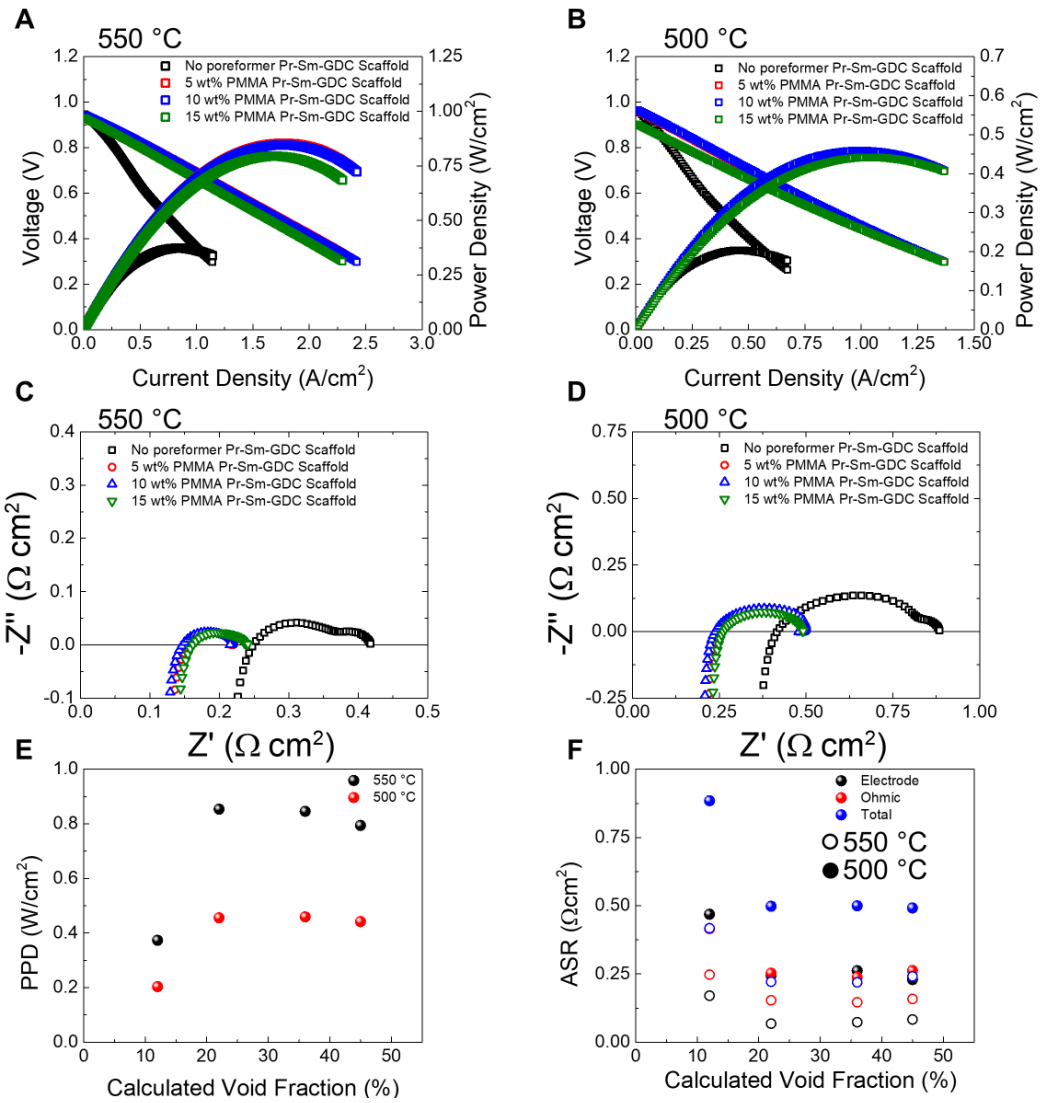

Figure 5.12 Scaffold Porosity Effect on 5-5-90 Pr-Sm-GDC. iV behavior at **A** 550 °C and **B** 500 °C. EIS at **C** 550 °C and **D** 500 °C. E PPD as a function of calculated void fraction assuming a dense scaffold of GDC (approximation). **F** Deconvoluted ASR as a function of calculated void fraction at 550 °C and 500 °C. Cell configuration is Ni-GDC/GDC (20μm)/5-5-90 Pr-Sm-GDC Scaffold infiltrated with 18 μL of PSC with varying concentrations of PMMA in the scaffold as pore former.

The symmetric cell effect on the PMMA loading in the 5-5-90 Pr-Sm-GDC infiltrated scaffolds is shown below in Figure 5.13 (Temperature dependence) and Figure 5.14 (pO_2). These results indicate that the 10 wt % PMMA loading could be the optimal porosity loading for the Pr-Sm-GDC scaffold. The pO_2 dependence results indicate about the same dependence on pO_2 for each of the scaffolds. However, the full

cell results indicate that 5 wt% PMMA is sufficient to allow for greater dispersion of the PSC infiltrate throughout the 5-5-90 Pr-Sm-GDC scaffold.

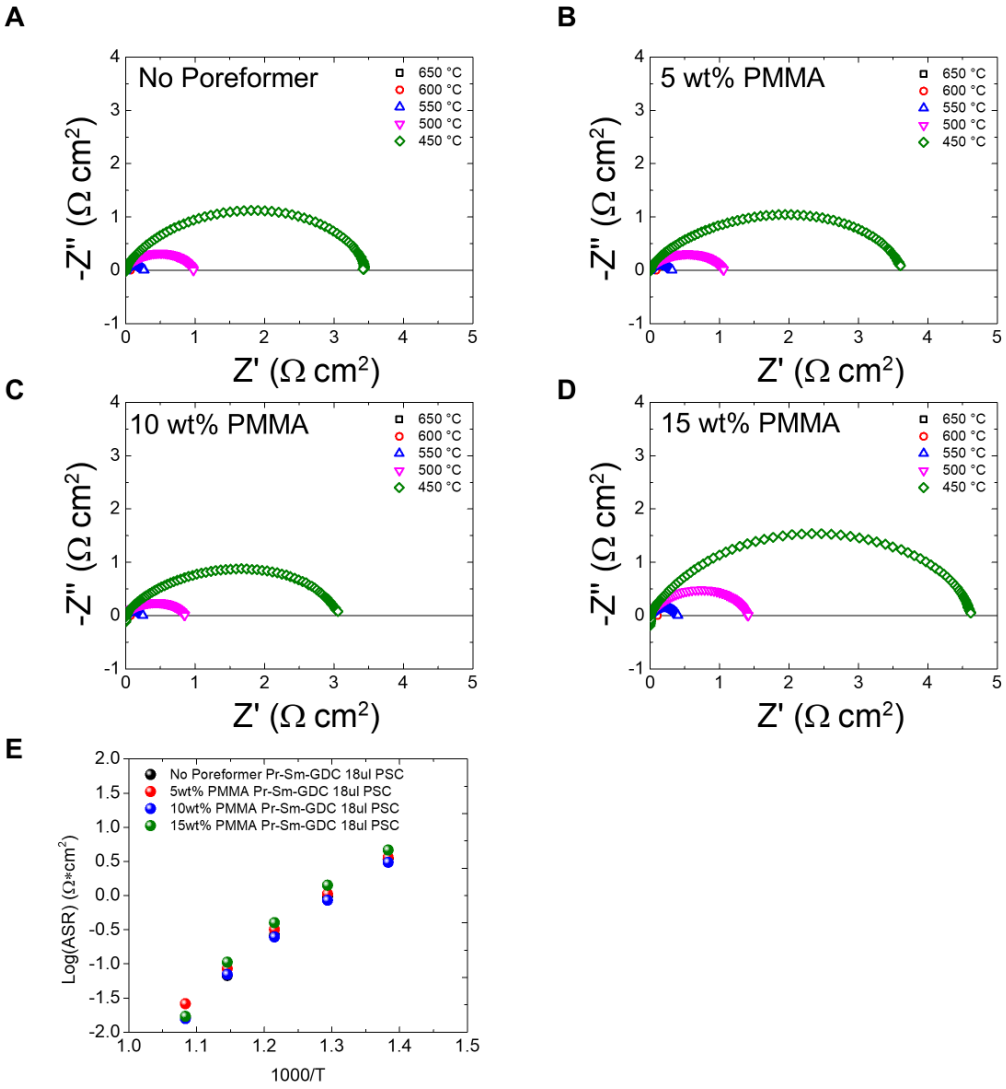

Figure 5.13 Symmetric Cell Porosity Effect of PSC infiltrated on 5-5-90 (Pr-Sm-GDC). Nyquist for the symmetric cell **A** without pore former, with **B** 5 wt% , **C** 10 wt%, and **D** 15 wt% PMMA. **E** Arrhenius behavior for symmetric cells tested with additional PMMA pore former. Symmetric Cell configuration is (PSC infiltrated 5-5-90 Pr-Sm-GDC Scaffold)/GDC/(PSC infiltrated 5-5-90 Pr-Sm-GDC Scaffold). 18 µL of PSC.

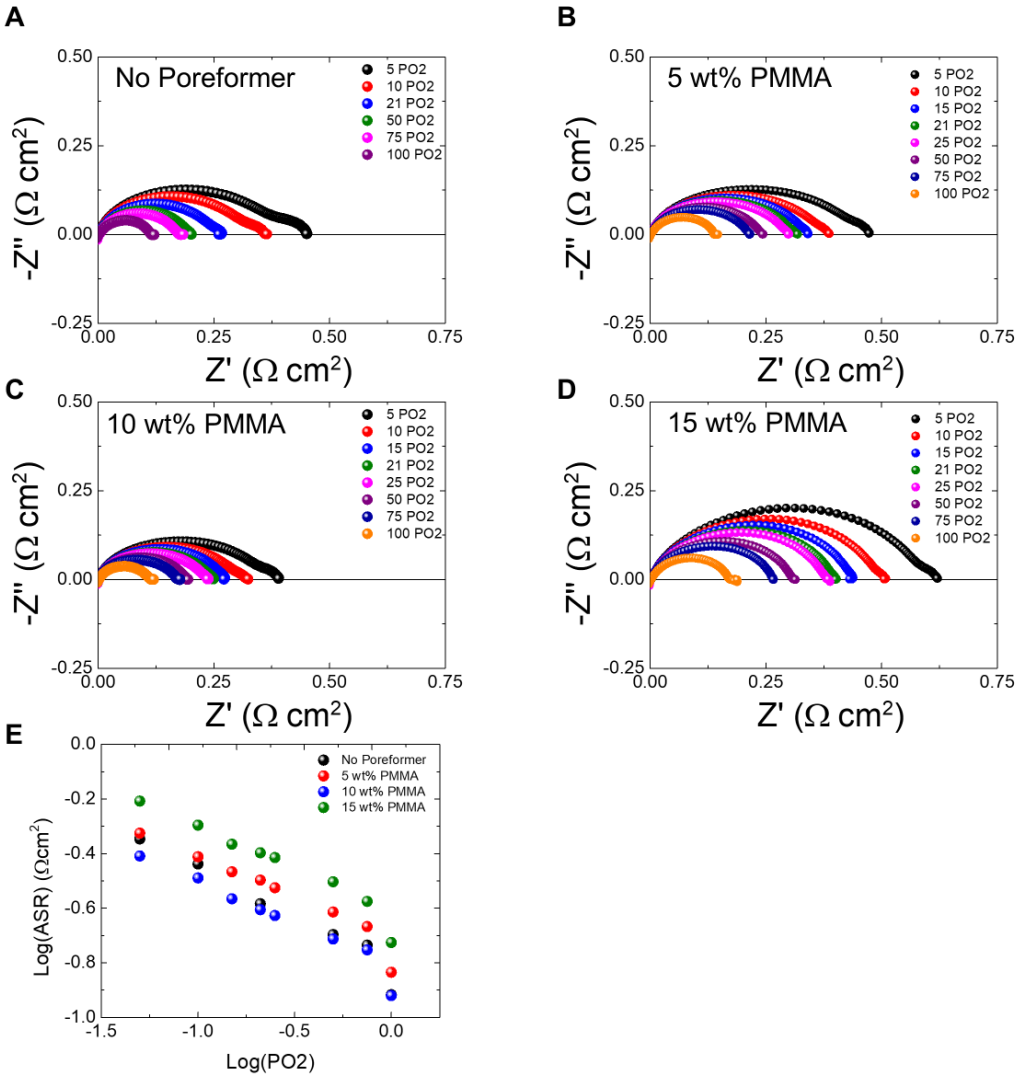

Figure 5.14 EIS pO_2 Dependence at 550 °C of 5-5-90 Pr-Sm-GDC PSC Infiltrated Symmetric Cells. Same symmetric cell configuration as Figure 5.13. **A** Nyquist of no pore former symmetric cell tested at 550 °C with varied pO_2 concentration denoted in the label. **B** Nyquist 5 wt% PMMA in 5-5-90 Pr-Sm-GDC Scaffold **C** Nyquist 10 wt% PMMA in 5-5-90 Pr-Sm-GDC Scaffold **D** Nyquist 15 wt% PMMA in 5-5-90 Pr-Sm-GDC Scaffold **E** electrode ASR vs log pO_2 showing pO_2 dependence of scaffold infiltrated symmetric cells at 550 °C.

The microstructure for the porosity study is shown in Figure 5.15 and Figure 5.16 below. SEM images were performed on infiltrated 5-5-90 Pr-Sm-GDC scaffolds. The results in Figure 5.15 A show that 5-5-90 Pr-Sm-GDC densifies the scaffold with increased lanthanide which could block gas diffusion or infiltrate dispersion to the

electrolyte region. This could explain the higher ohmic ASR seen in the impedance results in Figure 5.12. The calculated void fractions reveal that the 5 wt% PMMA was sufficient to increase the activity, however, SEM images show isolated pores compared to the 10 wt% and 15 wt%. Higher magnification is shown in Figure 5.16 and EDS results could agglomerate on the surface even with increased porosity leading us to believe that the scaffold is saturated with infiltrate.

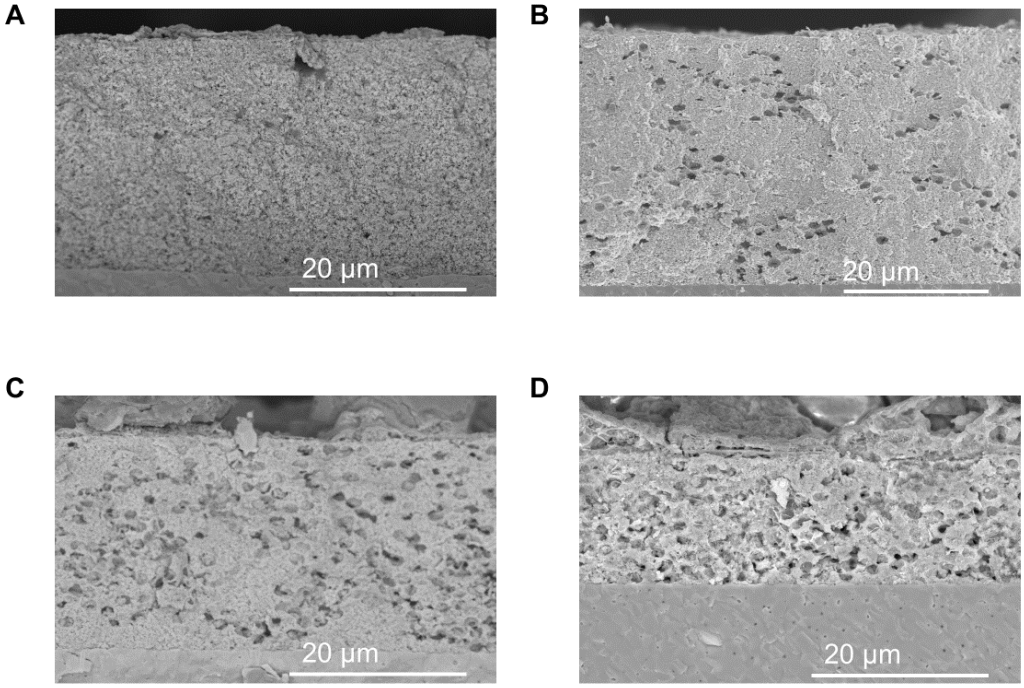

Figure 5.15 (5-5-90) Pr-Sm-GDC Scaffold Porosity Effect. 5-5-90 Pr-Sm-GDC **A** without PMMA pore former, with **B** 5 wt%, **C** 10 wt%, and **D** 15 wt% PMMA in the Pr-Sm-GDC scaffold. All cells were infiltrated with 18 µL PSC.

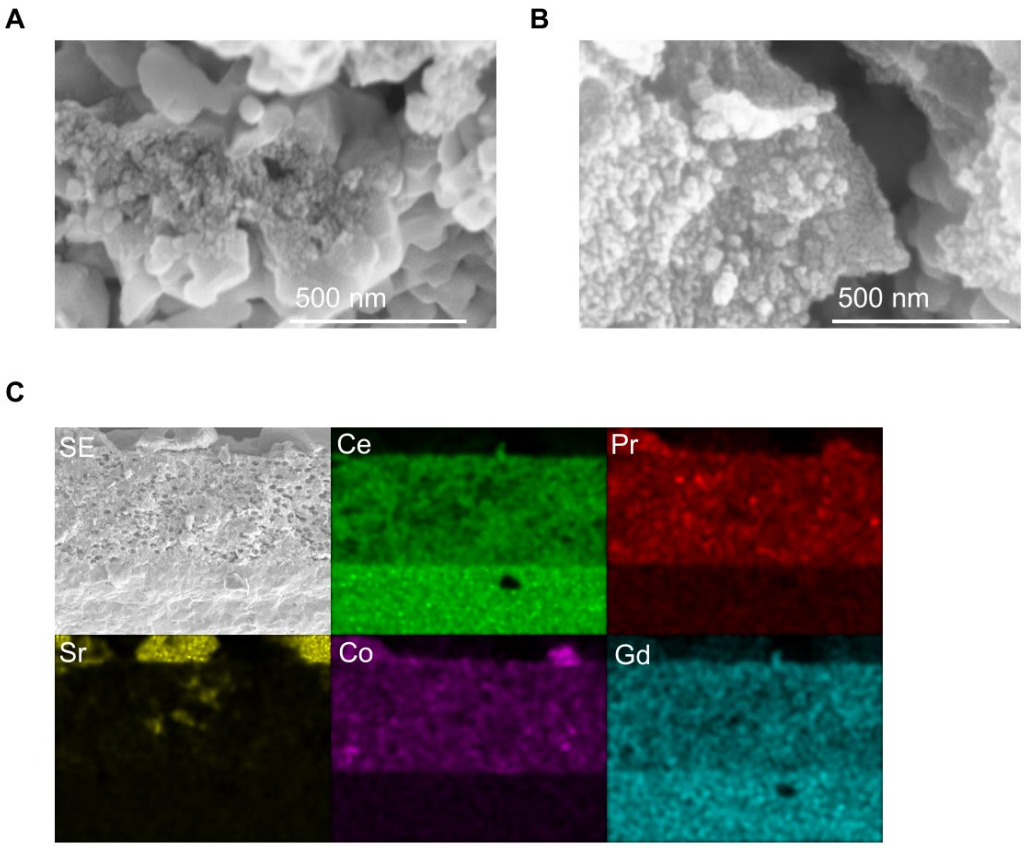

Figure 5.16 SEM Porosity Effect on Scaffold Continued. A 5wt% PMMA 5-5-90 Pr-Sm-GDC scaffold showing less connectivity of PSC than **B** 10 wt% PMMA 5-5-90 Pr-Sm-GDC scaffold. **C** EDS spectra showing agglomeration of strontium on the surface of the scaffold, Pr and Co are well dispersed through the scaffold.

The results for the other infiltrates screened on GDC scaffolds is shown below in Figure 5.17. Since there was agglomeration of strontium clearly seen in the EDS, it was thought that removing strontium from the infiltrate may increase the performance as isolated SrO is an insulating material. However, the impedance results on other screened symmetric cells show that strontium is a critical element in forming the active multiphase mixture. SSC was also screened due to its high activity proven as a SOFC cathode, but the low temperature infiltration likely did not form the correct SSC phase, leading PSC to be the most active material of the screened infiltrates and the infiltrate of interest for this study.

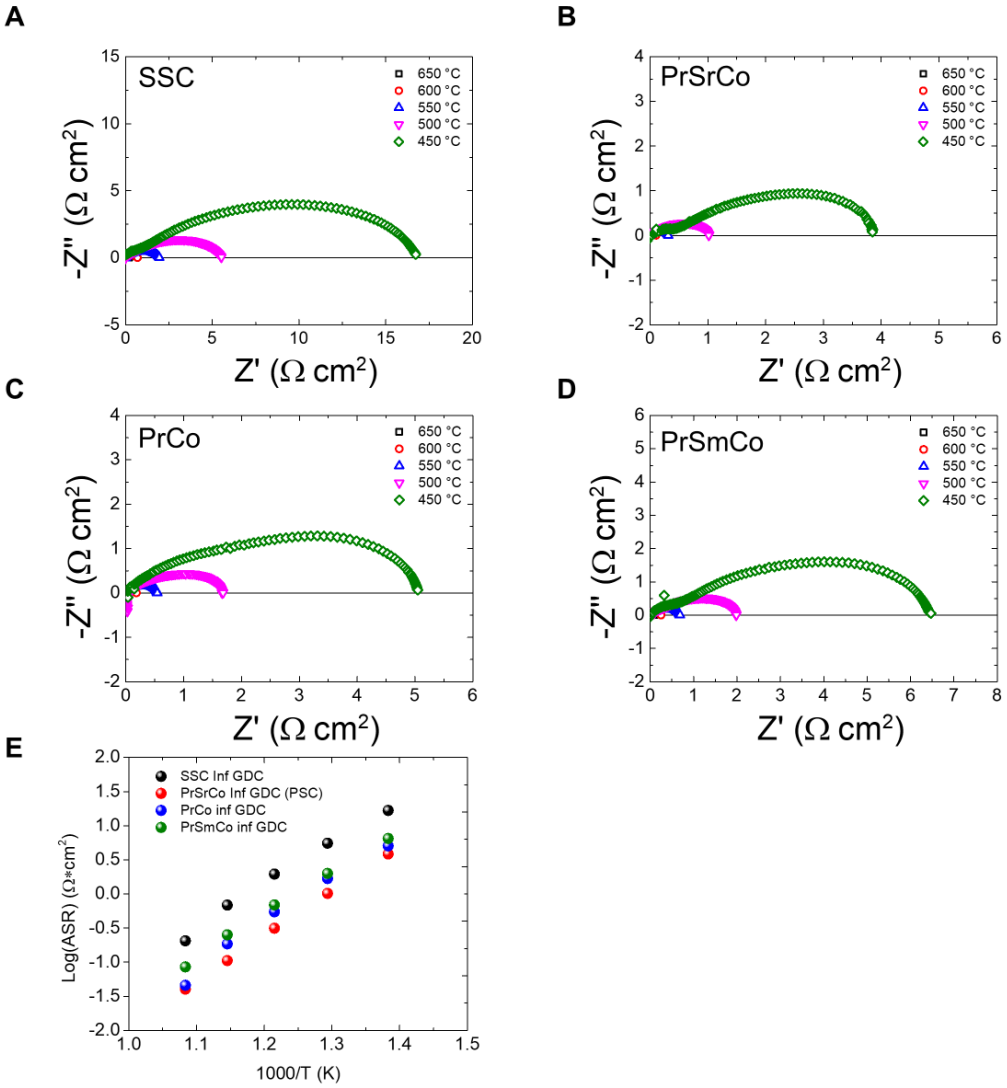

Figure 5.17 Screened Infiltrates **A** Sr-Sm-Co (1-1-2 mol ratio) infiltrated GDC symmetric cell Nyquist plot. **B** Pr-Sr-Co (1-1-2 mol ratio) infiltrated GDC symmetric cell Nyquist plot. **C** Pr-Co (1-1 mol ratio) infiltrated GDC symmetric cell. **D** Pr-Sm-Co (1-1-2 mol ratio) infiltrated GDC symmetric cell. **E** Arrhenius behavior of other screened infiltrate compositions. All symmetric cells were infiltrated with 6 µL of infiltrate on a GDC scaffold.

5.3 Conclusion

This work successfully demonstrates a viable, cost-effective, and scalable approach for low-temperature SOFCs, and by increasing the MIEC of scaffold, and the connectivity of the surface electrocatalysts, we addressed the electronic connectivity

issue generally associated with the scaffold design. Meanwhile, the low operating temperature prevents the agglomeration of surface electrocatalysts and ensures the continuously connective network even after 500 hours of operation.

The demonstrated promising approach to reduce the cost and processing intensity of high-temperature solid oxide devices, overcomes a critical step to deploy this technology on a wide scale. The use of ceria-based scaffold potentially decreases the number of high-temperature thermal processing steps and prevents interdiffusion between heterogenous layers while the switch from conventional bulk cathode to infiltrated nanoscale electrocatalysts reduces the material waste. This innovative design allows low cost, simplified processes, high performance, and high stability SOFCs that operate below 550 °C.

5.4 Experimental Methods not Previously Discussed in Chapter 2

Scaffold inks were created by mixing Pr_6O_{11} (Sigma-Aldrich), Sm_2O_3 (Alfa-aesar), and GDC (Fuel cell materials) powder to their respective compositions by wt% of precursor powder (e.g. 5Pr-GDC is 5wt% Pr_6O_{11} – 95wt% GDC) and so forth. The mixed composition was then ball milled overnight in ethanol and ESL 441 ink vehicle (Electroscience) was mixed with the mixture in a thinky mixer until a 1:1 by weight ESL:Powder ratio was met and all ethanol was evaporated. For the inks with PMMA, Sokken MX-150 PMMA was added to the mixture before ball milling by weight % to the powder. Inks were sintered on either symmetric or full cells at 950 °C for two hours with a 400 °C for 30 minutes intermediate burnout step to burn out the PMMA and binders.

The PSC electrocatalyst was synthesized by dissolving Pr-Sr-Co nitrates in a (1-1-2) mol ratio by metal cation. $Pr_{0.5}Sr_{0.5}CoO_{3-\delta}$ was the targeted phase. $PrCoO_3$, $Pr_{0.5}Sm_{0.5}CoO_{3-\delta}$, and $Sr_{0.5}Sm_{0.5}CoO_{3-\delta}$ infiltrates were also produced by the same method. The pH of the infiltrate mixture was balanced by adding ammonium hydroxide to the nitrate solution to a final pH of ~7. 3 wt% Triton X100 (Sigma Aldrich) to NO_3 ion was added as a surfactant to increase pore wettability. The results in Figure 5.1 were done with a solution that was not pH balanced and without Triton X100. Cells were infiltrated with 2 μL/0.31cm^2 vacuum dried for ~15 minutes to increase pore wettability. This was repeated two times per infiltration cycle for a total of 6 μL/0.31cm^2 of infiltrate per scaffold. The cells were fired at 450 °C for 30 minutes to evaporate the nitrate and the infiltration was repeated to meet the desired loading. 1 cycle corresponds to one low temperature firing in the furnace. High temperature XRD measurements were taken with a Bruker C2/D8 discover diffractometer.

Chapter 6. Metal Supported Solid Oxide Fuel Cells

Section 6.1 Introduction to Metal Supported SOFCs

Metal supported SOFC (MS-SOFC) are a relatively new type of SOFC that are comprised of a porous metal support infiltrated with electrode catalysts. [9,45,45,46,93–95] The metal support provides more mechanical durability, redox tolerance, and resistance to thermal cycling than cermet or ceramic supported SOFCs.[93] One of the most attractive traits of a MS-SOFC is their ability to heat up and cool down rapidly as stated before without shattering due to thermal shock like ceramic or cermet cells.[96] This makes MS-SOFCs an ideal candidate to be used for passenger transportation applications like cars and busses. While consumers do not want to wait an hour for their car or truck to heat up to the SOFC operating temperature, MS-SOFCs overcome this issue and can be heated to their operating temperature in minutes. [96]

For transportation applications, it is also important to utilize fuels that have high volumetric energy density and are comparable to gasoline.[13] This would also keep the fuel storage tank on the vehicle the same size, as SOFCs operate about 30% more efficiently that internal combustion engines. Figure 6.1 shows the volumetric energy density and gravimetric energy density of alternative fuels shown in green and current fuels used for transportation. Alternative fuels like dimethyl ether, ammonia, ethanol, and methanol are all commercially available and produced at a wide enough scale already, or could be easily scaled up, to meet the demands of SOFC-fueled vehicles. [97–101] For the fuels in green, most can be produced as a carbon neutral fuel. It would not be economically feasible to produce synthetic methane as it is abundant in natural gas. Ethanol, methanol, ammonia, and dimethyl ether can all be produced in a carbon

neutral method either through synthetic CO_2 utilization, Haber-Bosch utilizing electrolytically produced H_2, or through a bio-processing route.[14,99,102–105] A hybrid fuel cell-battery electric vehicle is an excellent route to decarbonizing passenger transportation.

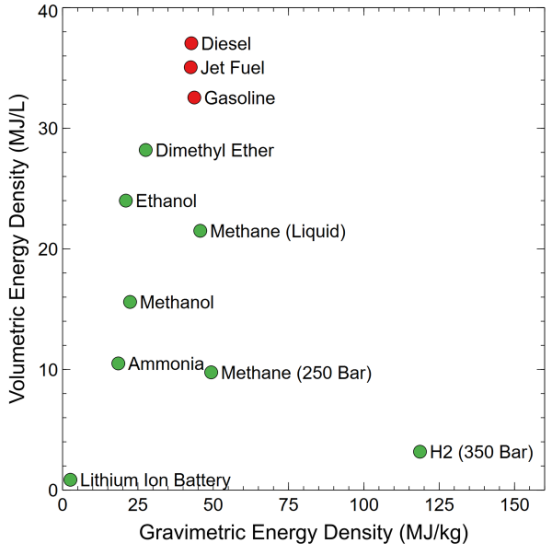

Figure 6.1 Energy Density Plot. Alternative fuels (green) to current fuels (red) used for transportation in passenger vehicles and lithium ion battery for reference. [13]

At the start of this project, MS-SOFCs had limited testing in alternative fuels other than hydrogen. To capitalize on the promising characteristics of MS-SOFCs, it became important to understand how they would operate on alternative fuels as cermet SOFCs had already shown to have great fuel flexibility. The main question to answer was "do MS-SOFCs have sufficient catalyst loading to internally reform C-H containing fuels?". MS-SOFCs only contain ~5-10 wt% nickel catalyst whereas cermet supported cells contain about 40-50% nickel in the anode. The specific fuels of interest were ethanol, methanol, ammonia, dimethyl ether, and methane.

Section 6.2 Experimental Methods MS-SOFC

6.2.1 Cell Preparation

Porous metal supports were prepared by a tape casting method and laminated together with tape cast yttria stabilized zirconia (YSZ) in line with reference. Electrode catalyst nitrate precursor solutions were prepared by mixing nitrate salts (Sigma Aldrich) along with Triton X-100 (Union Carbide Chemicals and Plastics Co., Inc.) surfactant. The nitrate precursor solution was then infiltrated into the porous metal support in accordance with reference. [45] The anode catalyst is samarium doped ceria with nickel (SDCN) and the cathode catalyst is lanthanum strontium manganite (LSM). The total cell active area is $1cm^2$. The amount of anode catalyst loading was tailored for the specific fuel condition.

6.2.2 Cell Testing

After infiltration, cells were attached to an in-house built test rig using a glass seal, and Pt mesh was spot-welded directly to the metal support. Gas flow rates are controlled by mass flow controllers and rotameters (MKS, Dwyer). To deliver the liquid fuel, a syringe pump (syringepump.com) was used at varying flow rates dependent on the targeted fuel utilization for each fuel to prevent carbon deposition. [2,106]

Initial fuel cell performance for each cell was evaluated in H_2 and its respective fuel at 700 °C, measuring open circuit voltage to evaluate cell seal, Electrochemical Impedance Spectroscopy (EIS) (Solartron 1260 potentiostat/frequency response analyzer) to evaluate electrode polarization, and potentiodynamic current voltage (iV)

to evaluate fuel reforming capability. To evaluate fuel cell performance, electrochemical impedance spectroscopy was used with a Solartron 1260 potentiostat/frequency response analyzer. A potential of 0.7 V was applied to the cell operating on its respective fuel to evaluate stability.

Section 6.3 Results and Discussion MS-SOFC

6.3.1 Methane

Cells operating on methane were initially evaluated for OCV, EIS polarization, and i-V characterization for 97%H_2/3% H_2O and subsequently repeated in 97% CH_4/3% H_2O at 700 °C. Figure 6.2 A. shows the initial i-V curve for a cell tested in H_2 and CH_4. The anode side of the cell was also infiltrated with Ruthenium Nitrosyl Nitrate (Sigma Aldrich), believed to enhance electrochemical activity in methane.[107] Measured OCCV was 1.10 V and 1.00V for H_2 and CH_4 respectively. A peak power density (PPD) of 338 mW/cm^2 and 186 mW/cm^2 were recorded in H_2 and CH_4 respectively. Figure 6.2 B shows the electrode polarization for the cell tested in methane and in hydrogen. The ohmic impedance is 0.15 (Ω cm^2), which shows the similar behavior for each of the cells tested in this study. The strong concentration polarization operating in CH_4 could be due to the lack of activity in the MS-SOFC configuration. Subsequent studies after this showed that more catalyst loading was sufficient to break the C-H bond.

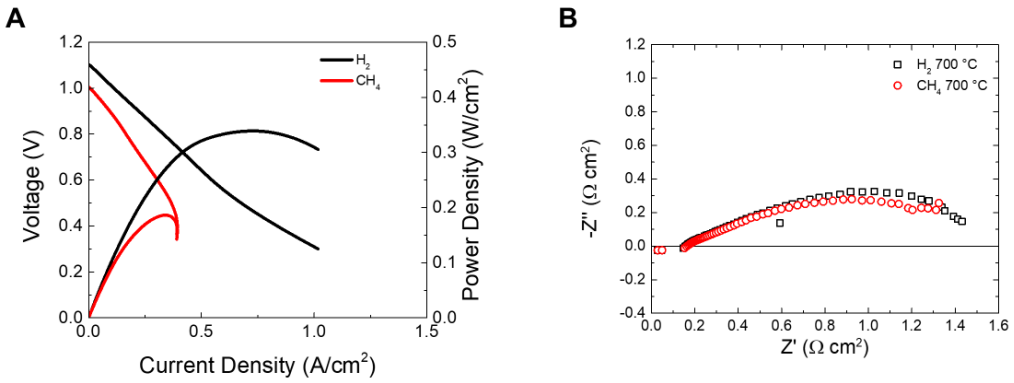

Figure 6.2 A) i-V for MS-SOFC operating on humidified H_2 (Black) and Humidified CH_4 (Red). B) MS-SOFC polarization running on Humidified H_2 (Black) and CH_4 (Red)

6.3.2 Ammonia

Ammonia is stored as a liquid and delivered to the cell directly as a gas, making ammonia an ideal candidate to utilize the current liquid refueling infrastructure. However, some safety precautions would need to be taken into consideration and this could limit its use. A few transportation candidate applications would be long-haul trucks, commercial shipping, trains, and aviation. Ammonia will thermally decompose into N_2 and H_2 and will not produce NO_x. Shown in Figure 6.3 A is the i-V curve for the MS-SOFC operating in dry ammonia. The OCV and PPD are 1.206V and 570 $mW*cm^{-2}$ respectively, at 700 °C. PPD in ammonia is within 10% that of hydrogen, indicating that the fuel dilution of ammonia is low; the N_2 content in ammonia does not have a significant effect on cell performance since the fuel provided to the cell is in excess and the cell is provided enough hydrogen from the ammonia.

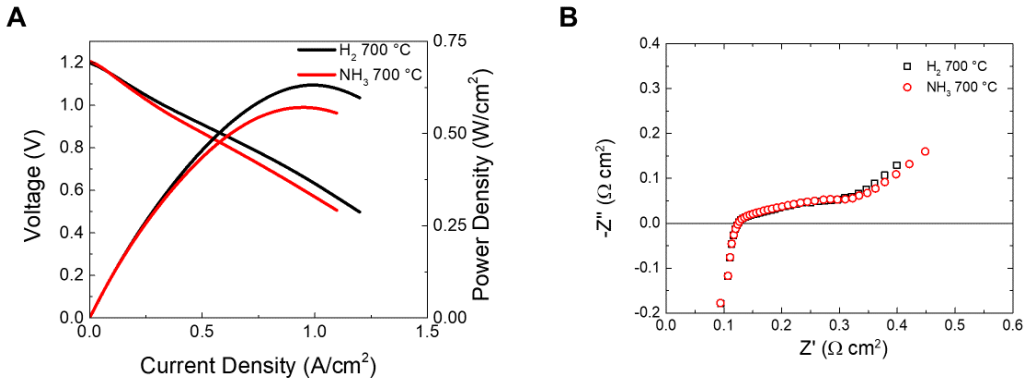

Figure 6.3 Metal Supported SOFC operating on dry H_2 (black) and dry NH_3 (red). A) iV behavior showing PPD in dry ammonia is 570 mW*cm^{-2} B) EIS showing ohmic ASR of about 0.1 Ωcm^2 and total ASR to be about 0.5 Ωcm^2.

6.3.3 Ethanol

An attractive liquid fuel that is currently mass-produced and is economical to store is ethanol. There have not been any reported studies of MS-SOFC operating on ethanol at the time of this project, so the collaborators in this study further researched MS-SOFCs operating on ethanol. Displayed in Figure 6.4 is a MS-SOFC operating on a 45%-55% water-ethanol mix delivered with a syringe pump. Power density operating on ethanol is 228 mW*cm^{-2} with an OCV of 0.99V at 700 °C. The i-V curve indicates that there is a significant amount of concentration polarization (large negative slope of the i-V curve) as the cell is driven with higher current. This could be due to anode catalyst loading being lower in MS-SOFCs (where the nanocatalyst is infiltrated into porous structure) than for all-ceramic SOFCs, which typically have 50% Ni metal in a few millimeter-thick anodes. Once the cell catalyst loading was optimized with more anode catalyst and a higher performing cathode, the follow up work done by Dogdibegovic et. al. the PPD at 700 °C in pure ethanol is about 1.4 W/cm^2.[9] The MS-SOFC shown here contains a thick, porous stainless steel without reforming

capabilities. Coating the anode backbone layer is a thin ≈ 100-300nm layer of $Sm_{0.2}Ce_{0.8}O_2$ with 20 wt% Nickel, functioning as the anode catalyst.

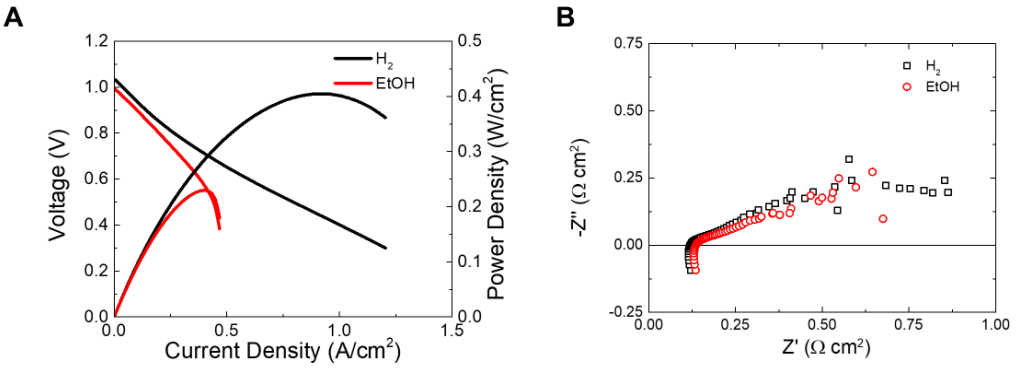

Figure 6.4 MS-SOFC operating on 45% EtOH 55% H_2O delivered through a syringe pump. A iV showing the PPD in ethanol is 200 mW/cm^2. B EIS showing that the total ASR is about 1 Ωcm^2 with an ohmic of 0.1 Ωcm^2 at 700 °C.

6.3.4 Methanol

Methanol is another liquid fuel that has been evaluated as an alternative fuel. Methanol is considered to be one of the more promising alternative fuels due to its high volumetric energy density, carbon neutral production capabilities, and facile storage capabilities. The main concern with using methanol is the safety of handling methanol because it is a toxic liquid that is not meant to be ingested. Gasoline is also not something that should be ingested, so refueling vehicles could be feasible if the right safety precautions are taken. Methanol delivery is similar to that of ethanol, so for comparison, a 45%-55% methanol-water mix was used which was delivered directly to the cell using a syringe pump. Shown in Figure 6.5 is the MS-SOFC operating on a methanol-water mix, with a PPD of 200 mW*cm^{-2} and OCV of 1.01V. The IV curve behavior is like that of the ethanol tested cell in Figure 6.4 and depicts high concentration likely due to insufficient catalyst loading. All cells used in this study were normalized to the same catalyst loading to have an understanding of how the

reference operates on different fuels. To increase the reforming capability in methanol higher catalyst loading should be introduced to the anode just like for ethanol.

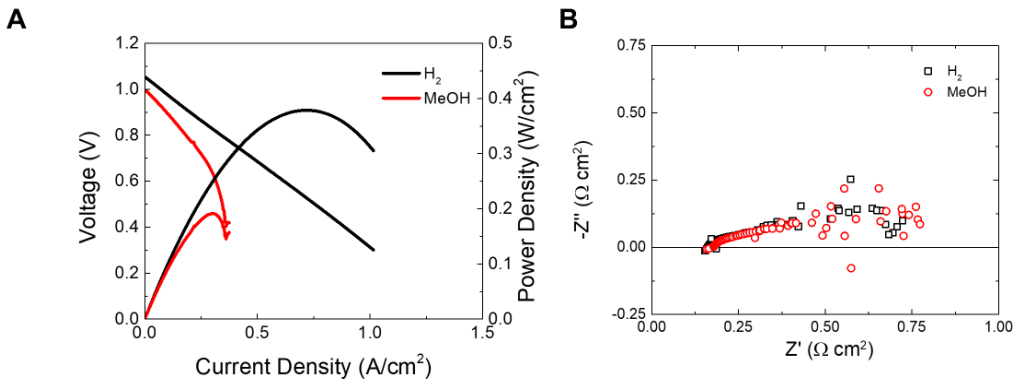

Figure 6.5 A) IV curve for MS-SOFC operating on methanol (45%) water (55%) mix. PPD of 200 mW/cm^2 and OCV of (0.99V). B) EIS The ohmic is 0.1 Ωcm^2 and the non ohmic is about 0.5 Ωcm^2.

6.3.5 Dimethyl Ether

Dimethyl ether is another candidate for alternative fuel due to its ability to be stored as a liquid, carbon neutral production capabilities, and low cost. Out of all of the fuels tested in this study, dimethyl ether contains the highest volumetric energy density (28 MJ/L) compared to that of ethanol, methanol, methane, and ammonia (< 25 MJ/L). Dimethyl ether has been touted as one of the most promising candidates for transportation purposes due to each of these factors. The use in a fuel cell is facile due to its storage as a liquid and DME is delivered as a gas which simplifies the fuel delivery. Figure 6.6 shows the performance of a MS-SOFC operating on DME. The performance in DME is about 70% of that in H_2 with the PPD being 350 mW/cm^2 compared to 500 mW/cm^2 respectively at 700 °C. The impedance reveals a lower ohmic ASR but higher non-ohmic which could be due to a few factors. First, DME is CH_3-O-CH_3 which has a lower bond strength (335 kJ/mol) than an OH bond (428

kJ/mol). Second, the fuel in each of the tested alcohols was also diluted to 45% alcohol by volume which could be a reason for reduced power density compared to DME. Nonetheless, a higher catalyst loading in the anode could add additional activity to the cell.

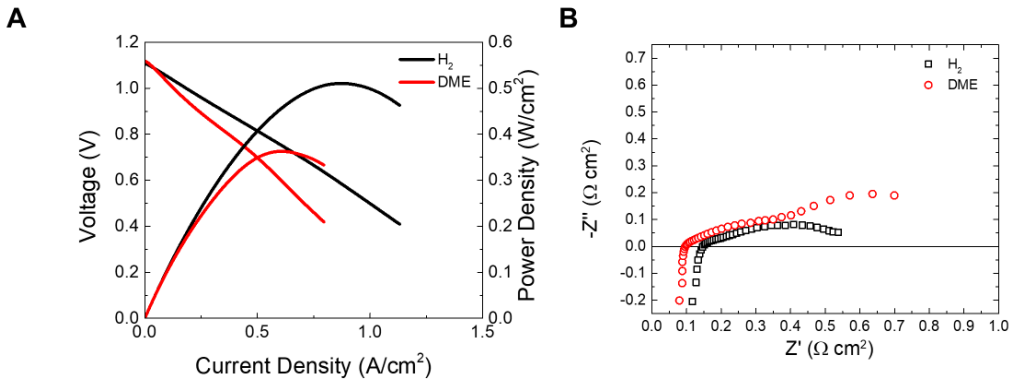

Figure 6.6 MS-SOFC performance operating on dimethyl ether. A) iV behavior showing a PPD of 350 mW/cm^2 which is 65% of the hydrogen performance. B) EIS for the cell in A.

Conclusion

In this project we have demonstrated the potential use of fuel flexible MS-SOFCs by evaluating initial performance with 5 different fuels: methane, ammonia, ethanol, dimethyl ether and methanol. Each fuel has a variety of commercial applications including power generation, grid demand management, transportation, and others. Dimethyl ether and ammonia seem to be the most promising fuels due to their high-power densities and storage and delivery applications. Both can be produced via carbon neutral methods, but this will require major advances in electrolysis technologies to produce economically viable clean hydrogen. In this project we have demonstrated that hydrocarbon fuels can be internally reformed in MS-SOFCs without SO_x or NO_x emissions. Further work is required to increase the catalytic activity (cell

performance) and durability of MS-SOFCs. The development of new anode catalyst materials is in progress.

Chapter 7. Conclusions and Future Work

7.1 Conclusions

The work shown in this dissertation accomplishes the main goal set out in the introduction of lowering the operating temperature of SOFCs and bringing the technology closer to wide scale commercialization. The techniques shown in this work prove that an SOFC can operate with high power density and high durability for multiple 2000-hour tests at various temperatures between 500 °C and 600 °C. The impact of lower temperature operation will allow for the use of new lower-cost stack components, namely SOFC interconnects, which are currently one of the main barriers to commercialization. Lowering the operating temperature of SOFCs to below 600 °C showed that most of the cell degradation can be mitigated with the use of a novel porous functional layer paired with surface modification via solution infiltration. The three main pillars of this work highlight several methods that can be used to improve the performance and durability of SOFCs. The first study focuses on performing solution infiltration at lower temperatures to preserve the nanostructure of nanoparticles, which is critical for high activity electrodes. The second study shows the impact of adding a porous ceria layer to utilize ceria's high oxygen ion transference number in a high pO_2 environment by forcing the porous layer to be exposed directly to air. The final study shows how the design of a ceria-based scaffold can efficiently use any desired electro catalyst as the cathode. An additional study was completed to demonstrate the feasibility of using MS-SOFCs to generate alternative fuels for transportation. The characterization of leading alternative fuel candidates was also completed on MS-

SOFCs highlighting the internal reforming capabilities to operate on 5 different alternative fuels.

The first study in this work explored the use of nano-catalysts to improve the activity and durability of SOFC cathodes. Both rare earth elements and transition metals were chosen for screening on symmetric cells in this work because they are both constituent elements in traditional SOFC cathodes. The motivation for testing transition metals arose from the idea that transition metals are responsible for the activity in cathode materials, and transition metal nano-particles were thought to increase activity. Contrary to our hypothesis, the transition metal catalysts screened in this study did not increase the activity of the selected SSC-GDC cathode as expected. The rare earth elements were selected based on whether they were multivalent or not. The multiple valance states of the Pr catalyst contributes to an increased number of oxygen vacancies as Pr has been found to have the ability to rapidly change its oxidation state in SOFC cathode operating conditions. Once the ideal catalyst, Pr, was selected, subsequent studies were done to characterize its role in the SSC-GDC cathode system. EIS experiments were performed and indicated Pr-SM low electrode ASR of $< 0.1\ \Omega cm^2$ at 600 °C compared to the unmodified SSC-GDC which was about $0.3\ \Omega cm^2$ at 600 °C. Other experiments including TPD, high temperature TEM, TEM-EELS, and TEM-EDS helped illuminate the role of the Pr catalyst in the system. TPD revealed that a low temperature nano-particle deposition preserved the nano-structure, which leads to higher oxygen activity and prevents nano-particle sintering. High temperature TEM showed how the structure of Pr catalyst changes across different temperatures as well as the oxidation state within the fuel cell operating regime (500-600 °C). TEM-EELS

showed how Pr coats the SSC-GDC cathode on only the cathode particle surface, adding activity to the ORR as it is a surface reaction. Further electrochemical testing on button cell SOFCs showed that the new Pr-SM SSC-GDC had excellent sustained durability with high power density at 600 °C for over 2000 hours. The main takeaway from this work is that a nanoscale catalyst can be used to modify an existing electrode to increase activity and durability.

The second study in this work focused on increasing the oxygen ion transference number, and therefore OCV, in ceria electrolyte-based SOFCs. Doped ceria is a great low temperature SOFC electrolyte, but it does not have an oxygen ion transference number of 1. The oxygen ion transference number of doped ceria is only about 0.8, which means that 20% of the reaction is being wasted due to an electronic leakage current. The oxygen ion transference number of ceria is pO_2 dependent and shows a lower transference number in a low pO_2 environment (fuel atmosphere pO_2 = 10^{-31}-10^{-25} atm), a slightly higher transference number in an intermediate pO_2 environment, and a higher transference number in a high pO_2 environment. The porous ceria layer, or PFL, is forced to be in a high pO_2 environment because it is porous and exposed to air which has a pO_2 = 0.21 atm, which causes the ceria to have a higher oxygen ion transference number within this regime. The oxygen ion transference number of the new PFL system is about 0.93 compared to 0.8 at 500 °C for the original single layer dense ceria configuration. This corresponds to only a 7% loss due to leakage current in the new PFL system, thus increasing the overall efficiency of the device. The PFL also increased the activity of the SSC-GDC cathode by adding active

dopants to the PFL. The structure and composition of the PFL was optimized to show that 2000 hours of operation at 500 °C with high power density (0.5 W/cm^2) is possible.

The third study in this work investigates methods to efficiently use electrocatalysts for SOFC cathodes. Currently, SOFC cathodes contain bulk cobalt oxide in their structures which are primarily used for catalytic activity towards the ORR and for electronic conductivity to transport electrons to the external circuit. The ORR is a surface reaction which means the ORR catalyst only needs to be on the surface of the electrode. A conductive scaffold was developed to avoid the use of cobalt oxide and other expensive catalyst materials. The scaffold facilitates oxygen ion and electron transport, leaving the PSC catalyst to function as the ORR catalyst in the multistep cathode reaction. A mechanism was proposed to show why the increased surface area of a nanoparticle + scaffold had higher activity than a traditional composite cathode. DRT results showed that the surface reaction step had a significant increase in activity, which lead to the proposed nanoparticles + scaffold approach. This study also showed that very high power density of 1 W/cm^2 at 550 °C could be attained using the scaffold infiltrated electrode approach, which does not contain a traditional SOFC cathode. The nano-particle structure was preserved for 500 hours at 550 °C and showed minimal degradation. The degradation that did occur appeared to be the result of nano-particle coarsening during the first 50 hours of operation. Further characterization of the PSC electrocatalyst revealed that a multiphase mixture of PrO_2, Co_3O_4, and $SrCoO_{3-\delta}$ were responsible for the high activity of this configuration. Other studies focus on achieving a pure phase perovskite before testing the electrocatalyst. This approach requires high temperature calcination of the nanoparticles (T>800 °C) which leads to nano-particle

sintering and lowers the activity of the catalyst. The first study in this dissertation shows that the low temperature calcination of nanoparticles is key to preserving the structure and activity of the catalyst. The main conclusions of the third study shows that a multiphase electrocatalyst can be deposited on a conductive cathode scaffold that is compatible with many electrocatalysts to achieve high power density, lasting durability, and efficient catalyst usage.

The final study explored the use of MS-SOFCs operating on alternative fuels for transportation applications. MS-SOFCs do not contain the same amount of Ni catalyst in the anode as a cermet-supported SOFC so there were concerns with the ability to internally reform hydrocarbon fuels. Some of the hydrocarbon fuels required additional catalyst, which was studied in a follow-up project by some of the coauthors of this initial feasibility study. The results of the alternative fuels project showed that MS-SOFCs can operate on a range of alternative fuels for transportation applications. The two best alternative fuels in this study were revealed to be ammonia and dimethyl ether because their PPDs only showed a marginal drop-off compared to hydrogen.

7.2 Contributions of this Dissertation

7.2.1 High Performance and Durable SOFCs Operating at Low Temperature

This work demonstrates the result of pairing a porous functional layer with the infiltration of Pr nanoparticles on SOFC cathodes - high performing SOFCs (PPD 0.5 W/cm^2) capable of operating with limited degradation for over 2000 hours at 500 °C. This is a major breakthrough that allows for the use of cheaper cell components and

shorter startup-shutdown times, and brings the technology closer to commercialization by operating at a lower temperature.

7.2.2 CO_2 Durability

This work shows that strontium-based cathodes operating in the presence of CO_2 can be durable and maintain low ASR (<0.3 Ωcm^2) at 600 °C for over 500 hours. The impact of CO_2 durability shows that SOFC cathodes can operate with exposure to the common contaminant gas CO_2, which is contained in the air and is an issue for current SOFC cathodes.

7.2.3 Limiting the Electronic Leakage Current in Ceria

LT-SOFC ceria-based electrolytes currently have issues with electronic leakage current, which lowers the efficiency of the SOFC reaction, and prevents their use as a viable LT-SOFC electrolyte. This work overcomes the leakage current issue by engineering a porous functional layer that increases the ionic transference number of a thin ceria-based electrolyte SOFC from 0.8 to 0.93 at 500 °C. The impact of this increases the faradaic efficiency of the SOFC reaction by 16%.

7.2.4 Universal Cathode Scaffold

A universal cathode scaffold was developed as a conductive backbone to use cathode materials more efficiently. Currently, SOFC cathodes contain scare and expensive materials like cobalt oxide, which is contained in the bulk. This work limits the use of the cathode catalyst to the surface of the scaffold, and shows high durability (over 500 hours of operation) with high performance (1 W/cm^2 at 550 °C). This

approach uses catalyst more efficiently, allows for the exploitation of any desired electrocatalyst, and still maintains high performance without the use of a bulk cathode.

7.2.5 Fuel Flexibility in MS-SOFCs

MS-SOFCs are ideal candidates for passenger transportation due to their ability to be rapidly thermally cycled, redox tolerance, and mechanical durability. However, prior to this work they have only been explored for operation on hydrogen. The U.S. currently lacks hydrogen refueling infrastructure, but passenger transportation needs to shift to carbon neutral fuels to combat climate change. This work demonstrates the use of MS-SOFCs operating on carbon neutral fuels (Ammonia, Ethanol, Methanol, and Dimethyl Ether) that could be easily integrated with current U.S. refueling infrastructure.

7.3 Future Work

7.3.1 Scaffold Infiltrated Electrodes

The same approach used for cathode scaffold optimization shown in Chapter 5 could be considered for the anode. Further studies could be done on a ceria-based anode scaffold as the anode still has numerous challenges associated with it. First, cermet anode supported cells are susceptible to fracture by redox cycling due to the oxidation and reduction of nickel oxide. The oxidation and reduction of nickel oxide results in a 40% volume expansion between Ni and NiO, causing the cell to crack. If there was a scaffold infiltrated anode as the case of a ceramic anode, it would show that the size of the infiltrated nickel is small relative to the size of the pores and electrolyte. So, if a

10nm infiltrated nickel particle oxidizes and reduces in a pore that is 1.5 μm in size it has the required space to expand and contract without cracking.

Shown in Figure 7.1 is a GDC scaffold supported cell that has a ~400 μm thick porous GDC support and 20 μm thick dense GDC electrolyte. The GDC was infiltrated with Ni for testing. The performance was too low for this to be an operable cell, but further work could be done to increase the electronic conductivity of the GDC support to enhance the performance. If a suitable ceria based cell scaffold was synthesized for the anode, the entire cell could be sintered in one step which would limit the high temperature processing steps to only one as the Pr-Sm-GDC scaffold has already been developed for the cathode. This would allow for the infiltration of any desired nanocatalyst into both the anode and cathode without concerns for material compatibility as ceria is proven to be compatible with a variety of materials and is chemically resilient. Since Ni-based anodes are not coke tolerant, coke tolerant catalysts could be infiltrated concurrently with Ni to enhance coking tolerance. As Ni is necessary for the hydrogen oxidation catalyst, this would open the door to any catalyst that is durable in fuel cell operating conditions to be infiltrated on a scaffold to operate on a variety of fuels as a “kitchen sink” approach.

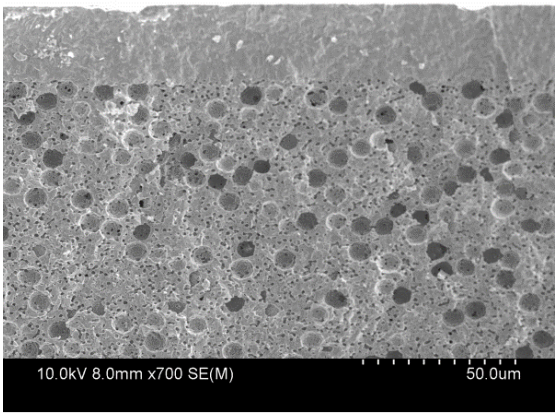

Figure 7.1 GDC Scaffold Supported Cell, GDC Scaffold Infiltrated with Ni.

Screening additional cathode catalysts could also be a route for improving cathode performance and chemical resiliency. Other studies have shown that different Pr containing compounds are effective at blocking CO_2 degradation in LSCF cathodes.[52] As Pr is a highly active ORR catalyst, it could be worth investigating the effect of the Pr containing compounds in addition to the ones shown in this work in the Pr-Sm-GDC scaffold as it is a proven conductive cathode scaffold.

7.3.2 Tuning the Stoichiometry of the PFL

To further enhance the OCV in MIEC electrolyte-based SOFC, further work could be performed on studying new dopants in ceria within the PFL. It was found that Pr enhanced total conductivity of the PFL, but not necessarily the ionic transference number, compared to porous GDC. There could be an optimal thickness of PFL that could lead to an enhancement in OCV for FE's > 95% which is a desired target of SOECs or reversible SOFCs. Other dopants that limit the Ce^{3+}-Ce^{4+} redox couple in the low and intermediate pO_2 regimes. To date, only a few elements have been studied for the effect on OCV in doped porous GDC.[77] Additional elements will have an effect

in this porous structure as it has been shown that a simple porous ceria layer behaves differently from its dense counterpart with a higher oxygen ion transference number.

7.3.3 Dense Layer at Cathode-PFL interface

A second thin dense layer could be placed at the PFL-cathode scaffold interface to enhance the OCV of the scaffold infiltrated electrode cells. The second dense layer would prevent the infiltrated electrode from going to the electrolyte cathode interface. The thickness of the dense layer would need to be minimized to be as thin as necessary to prevent the infiltrate from infiltrating the PFL. If the infiltrate reaches the electrolyte-PFL interface, then the OCV enhancement effect is negated.

Bibliography

1. Won, J. Y., Sohn, H. J., Song, R. H. & Woo, S. I. Glycerol as a Bioderived Sustainable Fuel for Solid-Oxide Fuel Cells with Internal Reforming. *ChemSusChem* **2**, 1028–1031 (2009).
2. Liu, M. *et al.* Direct liquid methanol-fueled solid oxide fuel cell. *J. Power Sources* **185**, 188–192 (2008).
3. Liao, M., Wang, W., Ran, R. & Shao, Z. Development of a Ni–Ce0.8Zr0.2O2 catalyst for solid oxide fuel cells operating on ethanol through internal reforming. *J. Power Sources* **196**, 6177–6185 (2011).
4. Wachsman, E. D. & Lee, K. T. Lowering the Temperature of Solid Oxide Fuel Cells. *Science* **334**, 935–939 (2011).
5. Steele, B. C. H. Running on natural gas. *Nature* **400**, 619–621 (1999).
6. Mehran, M. T. *et al.* Performance characteristics of a robust and compact propane-fueled 150 W-class SOFC power-generation system. *Int. J. Hydrog. Energy* **44**, 6160–6171 (2019).
7. Shao, Z. & Haile, S. M. A high-performance cathode for the next generation of solid-oxide fuel cells. *Nature* **431**, 170–173 (2004).
8. Taek Lee, K., M. Gore, C. & D. Wachsman, E. Feasibility of low temperature solid oxide fuel cells operating on reformed hydrocarbon fuels. *J. Mater. Chem.* **22**, 22405–22408 (2012).
9. Dogdibegovic, E., Fukuyama, Y. & Tucker, M. C. Ethanol internal reforming in solid oxide fuel cells: A path toward high performance metal-supported cells for vehicular applications. *J. Power Sources* **449**, 227598 (2020).

10. Chen, Y. *et al.* A robust fuel cell operated on nearly dry methane at 500 °C enabled by synergistic thermal catalysis and electrocatalysis. *Nat. Energy* **3**, 1042–1050 (2018).

11. D. Wachsman, E., A. Marlowe, C. & Taek Lee, K. Role of solid oxide fuel cells in a balanced energy strategy. *Energy Environ. Sci.* **5**, 5498–5509 (2012).

12. Ralph, J. M., Schoeler, A. C. & Krumpelt, M. Materials for lower temperature solid oxide fuel cells. *J. Mater. Sci.* **36**, 1161–1172 (2001).

13. Davis, S. J. *et al.* Net-zero emissions energy systems. *Science* **360**, eaas9793 (2018).

14. Ebbesen, S. D., Jensen, S. H., Hauch, A. & Mogensen, M. B. High Temperature Electrolysis in Alkaline Cells, Solid Proton Conducting Cells, and Solid Oxide Cells. *Chem. Rev.* **114**, 10697–10734 (2014).

15. L. Brett, D. J., Atkinson, A., P. Brandon, N. & J. Skinner, S. Intermediate temperature solid oxide fuel cells. *Chem. Soc. Rev.* **37**, 1568–1578 (2008).

16. *Solid state electrochemistry*. (Wiley-VCH, 2009).

17. Maricle, D. L., Swarr, T. E. & Karavolis, S. Enhanced ceria — a low-temperature SOFC electrolyte. *Solid State Ion.* **52**, 173–182 (1992).

18. SOFC OPERATING PRINCIPLE. *netl.doe.gov* https://www.netl.doe.gov/coal/sofc/operating-principle.

19. Barnett, S. A. A new solid oxide fuel cell design based on thin film electrolytes. *Energy* **15**, 1–9 (1990).

20. Hussain, A. M. & Wachsman, E. D. Liquids-to-Power Using Low-Temperature Solid Oxide Fuel Cells. *Energy Technol.* **7**, 20–32 (2019).

21. Yamahara, K., Jacobson, C. P., Visco, S. J., Zhang, X.-F. & De Jonghe, L. C. Thin film SOFCs with cobalt-infiltrated cathodes. *Solid State Ion.* **176**, 275–279 (2005).

22. Vohs, J. M. & Gorte, R. J. High-Performance SOFC Cathodes Prepared by Infiltration. *Adv. Mater.* **21**, 943–956 (2009).

23. Ding, D., Li, X., Lai, S. Y., Gerdes, K. & Liu, M. Enhancing SOFC cathode performance by surface modification through infiltration. *Energy Environ. Sci.* **7**, 552–575 (2014).

24. Kim, S. J. & Choi, G. M. Stability of LSCF electrode with GDC interlayer in YSZ-based solid oxide electrolysis cell. *Solid State Ion.* **262**, 303–306 (2014).

25. Lee, S., Miller, N., Abernathy, H., Gerdes, K. & Manivannan, A. Effect of Sr-Doped LaCoO3 and LaZrO3 Infiltration on the Performance of SDC-LSCF Cathode. *J. Electrochem. Soc.* **158**, B735 (2011).

26. Liu, M. *et al.* Enhanced performance of LSCF cathode through surface modification. *Int. J. Hydrog. Energy* **37**, 8613–8620 (2012).

27. Huang, Y.-L., Pellegrinelli, C. & Wachsman, E. D. CO2 and O2 Co-Exchange on Multivalent Metal Oxides. *J. Phys. Chem. C* **123**, 17711–17718 (2019).

28. Chen, Y. *et al.* A highly active, CO 2 -tolerant electrode for the oxygen reduction reaction. *Energy Environ. Sci.* **11**, 2458–2466 (2018).

29. Pellegrinelli, C., Huang, Y.-L., Taillon, J. A., Salamanca-Riba, L. G. & Wachsman, E. D. Investigating the Relationship between Operating Conditions and SOFC Cathode Degradation. *ECS Trans.* **68**, 773–784 (2015).

30. Hecht, E. S. *et al.* Methane reforming kinetics within a Ni–YSZ SOFC anode support. *Appl. Catal. Gen.* **295**, 40–51 (2005).

31. Weber, A. Oxidation of H2, CO and methane in SOFCs with Ni/YSZ-cermet anodes. *Solid State Ion.* **152–153**, 543–550 (2002).

32. Yang, Q. *et al.* Enhanced coking tolerance of a MgO-modified Ni cermet anode for hydrocarbon fueled solid oxide fuel cells. *J. Mater. Chem. A* **4**, 18031–18036 (2016).

33. Duan, C. *et al.* Highly durable, coking and sulfur tolerant, fuel-flexible protonic ceramic fuel cells. *Nature* **557**, 217–222 (2018).

34. Liu, M., Lynch, M. E., Blinn, K., Alamgir, F. M. & Choi, Y. Rational SOFC material design: new advances and tools. *Mater. Today* **14**, 534–546 (2011).

35. Matsuzaki, Y. The poisoning effect of sulfur-containing impurity gas on a SOFC anode: Part I. Dependence on temperature, time, and impurity concentration. *Solid State Ion.* **132**, 261–269 (2000).

36. Papurello, D. *et al.* Sulfur poisoning in Ni-anode solid oxide fuel cells (SOFCs): Deactivation in single cells and a stack. *Chem. Eng. J.* **283**, 1224–1233 (2016).

37. Weber, A., Dierickx, S., Kromp, A. & Ivers-Tiffée, E. Sulfur Poisoning of Anode-Supported SOFCs under Reformate Operation. *Fuel Cells* **13**, 487–493 (2013).

38. Hays, T., Hussain, A. M., Huang, Y.-L., McOwen, D. W. & Wachsman, E. D. Improved Sulfur Tolerance of SOFCs through Surface Modification of Anodes. *ACS Appl. Energy Mater.* **1**, 1559–1566 (2018).

39. Mistler, R. E. & Twiname, E. R. *Tape casting: theory and practice*. (American Ceramic Society, 2000).

40. Basics of EIS: Electrochemical Research-Impedance. https://www.gamry.com/application-notes/EIS/basics-of-electrochemical-impedance-spectroscopy/.

41. Thangadurai, V., Huggins, R. A. & Weppner, W. Mixed ionic-electronic conductivity in phases in the praseodymium oxide system. *J. Solid State Electrochem.* **5**, 531–537 (2001).

42. battery-EIS-Distribution of Relaxation Times DRT - Electrochemistry - Application Note 60. *Biologic* https://www.biologic.net/documents/battery-eis-distribution-of-relaxation-times-drt-electrochemistry-application-note-60/.

43. Wan, T. H., Saccoccio, M., Chen, C. & Ciucci, F. Influence of the Discretization Methods on the Distribution of Relaxation Times Deconvolution: Implementing Radial Basis Functions with DRTtools. *Electrochimica Acta* **184**, 483–499 (2015).

44. Hong, J., Bhardwaj, A., Bae, H., Kim, I. & Song, S.-J. Electrochemical Impedance Analysis of SOFC with Transmission Line Model Using Distribution of Relaxation Times (DRT). *J. Electrochem. Soc.* **167**, 114504 (2020).

45. Tucker, M. C., Lau, G. Y., Jacobson, C. P., DeJonghe, L. C. & Visco, S. J. Performance of metal-supported SOFCs with infiltrated electrodes. *J. Power Sources* **171**, 477–482 (2007).

46. Dogdibegovic, E., Wang, R., Lau, G. Y. & Tucker, M. C. High performance metal-supported solid oxide fuel cells with infiltrated electrodes. *J. Power Sources* **410–411**, 91–98 (2019).

47. Huang, Y.-L., Hussain, A. M., Robinson, I. A. & Wachsman, E. D. Nanointegrated, High-Performing Cobalt-Free Bismuth-Based Composite Cathode for Low-Temperature Solid Oxide Fuel Cells. *ACS Appl. Mater. Interfaces* **10**, 28635–28643 (2018).

48. Huang, Y.-L., Hussain, A. M. & Wachsman, E. D. Nanoscale cathode modification for high performance and stable low-temperature solid oxide fuel cells (SOFCs). *Nano Energy* **49**, 186–192 (2018).

49. Burnham, D. A. & Eyring, L. Phase transformations in the praseodymium oxide-oxygen system: high-temperature x-ray diffraction studies. *J. Phys. Chem.* **72**, 4415–4424 (1968).

50. Osinkin, D. A., Bogdanovich, N. M., Beresnev, S. M. & Zhuravlev, V. D. High-performance anode-supported solid oxide fuel cell with impregnated electrodes. *J. Power Sources* **288**, 20–25 (2015).

51. Nicollet, C. *et al.* An innovative efficient oxygen electrode for SOFC: Pr6O11 infiltrated into Gd-doped ceria backbone. *Int. J. Hydrog. Energy* **41**, 15538–15544 (2016).

52. Chen, H. *et al.* Improving the Electrocatalytic Activity and Durability of the La0.6Sr0.4Co0.2Fe0.8O3−δ Cathode by Surface Modification. *ACS Appl. Mater. Interfaces* **10**, 39785–39793 (2018).

53. Lu, M. Y. *et al.* Mechanisms of PrOx performance enhancement of oxygen electrodes for low and intermediate temperature solid oxide fuel cells. *Mater. Today Energy* 100362 (2019) doi:10.1016/j.mtener.2019.100362.

54. Ding, X., Zhu, W., Hua, G., Li, J. & Wu, Z. Enhanced oxygen reduction activity on surface-decorated perovskite La0.6Ni0.4FeO3 cathode for solid oxide fuel cells. *Electrochimica Acta* **163**, 204–212 (2015).

55. Kromp, A., Leonide, A., Weber, A. & Ivers-Tiffée, E. Electrochemical Analysis of Reformate-Fuelled Anode Supported SOFC. *J. Electrochem. Soc.* **158**, B980–B986 (2011).

56. Chen, Y. *et al.* A Highly Efficient Multi-phase Catalyst Dramatically Enhances the Rate of Oxygen Reduction. *Joule* **2**, 938–949 (2018).

57. Fukunaga, H., Koyama, M., Takahashi, N., Wen, C. & Yamada, K. Reaction model of dense Sm0.5Sr0.5CoO3 as SOFC cathode. *Solid State Ion.* **132**, 279–285 (2000).

58. Choi, S. *et al.* Highly efficient and robust cathode materials for low-temperature solid oxide fuel cells: PrBa 0.5 Sr 0.5 Co 2−x Fe x O 5+δ. *Sci. Rep.* **3**, 1–6 (2013).

59. Yan, A., Maragou, V., Arico, A., Cheng, M. & Tsiakaras, P. Investigation of a Ba0.5Sr0.5Co0.8Fe0.2O3−δ based cathode SOFC: II. The effect of CO2 on the chemical stability. *Appl. Catal. B Environ.* **76**, 320–327 (2007).

60. Bucher, E., Egger, A., Caraman, G. B. & Sitte, W. Stability of the SOFC Cathode Material (Ba , Sr) (Co , Fe) O3 − δ in CO2-Containing Atmospheres. *J. Electrochem. Soc.* **155**, B1218–B1224 (2008).

61. Takasu, Y. *et al.* Temperature-programmed desorption on the unstable lattice oxygen of praseodymium oxide. *J. Catal.* **69**, 51–57 (1981).

62. Bowman, W. J., March, K., Hernandez, C. A. & Crozier, P. A. Measuring bandgap states in individual non-stoichiometric oxide nanoparticles using

monochromated STEM EELS: The Praseodymium–ceria case. *Ultramicroscopy* **167**, 5–10 (2016).

63. Mark Ormerod, R. Solid oxide fuel cells. *Chem. Soc. Rev.* **32**, 17–28 (2003).
64. Kharton, V. V., Marques, F. M. B. & Atkinson, A. Transport properties of solid oxide electrolyte ceramics: a brief review. *Solid State Ion.* **174**, 135–149 (2004).
65. Riess, I. Characterization of solid oxide fuel cells based on solid electrolytes or mixed ionic electronic conductors. *Solid State Ion.* **90**, 91–104 (1996).
66. Riess, I. The possible use of mixed ionic electronic conductors instead of electrolytes in fuel cells. *Solid State Ion.* **52**, 127–134 (1992).
67. Kee, R. J., Zhu, H., Sukeshini, A. M. & Jackson, G. S. Solid Oxide Fuel Cells: Operating Principles, Current Challenges, and the Role of Syngas. *Combust. Sci. Technol.* **180**, 1207–1244 (2008).
68. Duncan, K. L. & Wachsman, E. D. Continuum-Level Analytical Model for Solid Oxide Fuel Cells with Mixed Conducting Electrolytes. *J. Electrochem. Soc.* **156**, B1030 (2009).
69. Wachsman, E. D., Jayaweera, P., Jiang, N., Lowe, D. M. & Pound, B. G. Stable High Conductivity Ceria/Bismuth Oxide Bilayered Electrolytes. *J. Electrochem. Soc.* **144**, 233–236 (1997).
70. Zhang, X. *et al.* Internal shorting and fuel loss of a low temperature solid oxide fuel cell with SDC electrolyte. *J. Power Sources* **164**, 668–677 (2007).
71. Duncan, K. L., Lee, K.-T. & Wachsman, E. D. Dependence of open-circuit potential and power density on electrolyte thickness in solid oxide fuel cells with mixed conducting electrolytes. *J. Power Sources* **196**, 2445–2451 (2011).

72. Eguchi, K., Setoguchi, T., Inoue, T. & Arai, H. Electrical properties of ceria-based oxides and their application to solid oxide fuel cells. *Solid State Ion.* **52**, 165–172 (1992).

73. Zhang, J., Lenser, C., Menzler, N. H. & Guillon, O. Comparison of solid oxide fuel cell (SOFC) electrolyte materials for operation at 500 °C. *Solid State Ion.* **344**, 115138 (2020).

74. Bishop, S. R., Stefanik, T. S. & Tuller, H. L. Defects and transport in Pr x Ce1-x O2-[delta]: Composition trends. *J. Mater. Res. Warrendale* **27**, 2009–2016 (2012).

75. Leonide, A. SOFC modelling and parameter identification by means of impedance spectroscopy. https://publikationen.bibliothek.kit.edu/1000019173 (2010) doi:10.5445/KSP/1000019173.

76. Chen, Y. *et al.* An In Situ Formed, Dual-Phase Cathode with a Highly Active Catalyst Coating for Protonic Ceramic Fuel Cells. *Adv. Funct. Mater.* **28**, 1704907 (2018).

77. Pan, K.-J. *et al.* Evolution of Solid Oxide Fuel Cells via Fast Interfacial Oxygen Crossover. *ACS Appl. Energy Mater.* **2**, 4069–4074 (2019).

78. Huang, Y.-L., Pellegrinelli, C. & Wachsman, E. D. Direct Observation of Oxygen Dissociation on Non-Stoichiometric Metal Oxide Catalysts. *Angew. Chem. Int. Ed.* **55**, 15268–15271 (2016).

79. Murray, E. P., Tsai, T. & Barnett, S. A. Oxygen transfer processes in (La,Sr)MnO3/Y2O3-stabilized ZrO2 cathodes: an impedance spectroscopy study. *Solid State Ion.* **110**, 235–243 (1998).

80. Fleig, J., Kim, H.-R., Jamnik, J. & Maier, J. Oxygen Reduction Kinetics of Lanthanum Manganite (LSM) Model Cathodes: Partial Pressure Dependence and Rate-Limiting Steps. *Fuel Cells* **8**, 330–337 (2008).

81. Nicholas, J. D. & Barnett, S. A. Measurements and Modeling of Sm0.5Sr0.5CoO3 − x – Ce0.9Gd0.1O1.95 SOFC Cathodes Produced Using Infiltrate Solution Additives. *J. Electrochem. Soc.* **157**, B536 (2010).

82. Cheng, Y. *et al.* Preparation of SOFC Cathodes by Infiltration into LSF-YSZ Composite Scaffolds. *J. Electrochem. Soc.* **163**, F54 (2015).

83. Lee, S. *et al.* Pr0.6Sr0.4CoO3−δ electrocatalyst for solid oxide fuel cell cathode introduced via infiltration. *Electrochimica Acta* **56**, 9904–9909 (2011).

84. Olivetti, E. A., Ceder, G., Gaustad, G. G. & Fu, X. Lithium-Ion Battery Supply Chain Considerations: Analysis of Potential Bottlenecks in Critical Metals. *Joule* **1**, 229–243 (2017).

85. Chen, Y., Liu, Q., Yang, Z., Chen, F. & Han, M. High performance low temperature solid oxide fuel cells with novel electrode architecture. *RSC Adv.* **2**, 12118–12121 (2012).

86. Lu, M. Y. *et al.* Mechanisms of PrOx performance enhancement of oxygen electrodes for low and intermediate temperature solid oxide fuel cells. *Mater. Today Energy* 100362 (2019) doi:10.1016/j.mtener.2019.100362.

87. Zemann, J. Crystal structures, 2nd edition. Vol. 1 by R. W. G. Wyckoff. *Acta Crystallogr.* **18**, 139–139 (1965).

88. Liu, X. & Prewitt, CharlesT. High-temperature X-ray diffraction study of Co3O4: Transition from normal to disordered spinel. *Phys. Chem. Miner.* **17**, (1990).

89. Nakatsuka, A., Yoshiasa, A., Nakayama, N., Mizota, T. & Takei, H. Oxygen-deficient strontium cobaltate, SrCoO2.64. *Acta Crystallogr. C* **60**, i59–i60 (2004).

90. Nie, L., Liu, M., Zhang, Y. & Liu, M. La0.6Sr0.4Co0.2Fe0.8O3−δ cathodes infiltrated with samarium-doped cerium oxide for solid oxide fuel cells. *J. Power Sources* **195**, 4704–4708 (2010).

91. Ding, D. *et al.* Efficient Electro-Catalysts for Enhancing Surface Activity and Stability of SOFC Cathodes. *Adv. Energy Mater.* **3**, 1149–1154 (2013).

92. Badwal, S. P. S. *et al.* Structural and microstructural stability of ceria – gadolinia electrolyte exposed to reducing environments of high temperature fuel cells. *J. Mater. Chem. A* **1**, 10768–10782 (2013).

93. Tucker, M. C. Progress in metal-supported solid oxide fuel cells: A review. *J. Power Sources* **195**, 4570–4582 (2010).

94. Tucker, M. C., Lau, G. Y., Jacobson, C. P., DeJonghe, L. C. & Visco, S. J. Stability and robustness of metal-supported SOFCs. *J. Power Sources* **175**, 447–451 (2008).

95. Udomsilp, D. *et al.* Metal-Supported Solid Oxide Fuel Cells with Exceptionally High Power Density for Range Extender Systems. *Cell Rep. Phys. Sci.* **1**, 100072 (2020).

96. Matus, Y., Dejonghe, L., Jacobson, C. & Visco, S. Metal-supported solid oxide fuel cell membranes for rapid thermal cycling. *Solid State Ion.* **176**, 443–449 (2005).

97. Lan, R., Irvine, J. T. S. & Tao, S. Ammonia and related chemicals as potential indirect hydrogen storage materials. *Int. J. Hydrog. Energy* **37**, 1482–1494 (2012).

98. Afif, A. *et al.* Ammonia-fed fuel cells: a comprehensive review. *Renew. Sustain. Energy Rev.* **60**, 822–835 (2016).

99. Alternative Fuels Data Center: Dimethyl Ether. https://afdc.energy.gov/fuels/emerging_dme.html.

100. Alternative Fuels Data Center: Methanol. https://afdc.energy.gov/fuels/emerging_methanol.html.

101. Wojcik, A., Middleton, H., Damopoulos, I. & Van herle, J. Ammonia as a fuel in solid oxide fuel cells. *J. Power Sources* **118**, 342–348 (2003).

102. Birdja, Y. Y. *et al.* Advances and challenges in understanding the electrocatalytic conversion of carbon dioxide to fuels. *Nat. Energy* **4**, 732–745 (2019).

103. Chen, G.-F. *et al.* Advances in Electrocatalytic N2 Reduction—Strategies to Tackle the Selectivity Challenge. *Small Methods* **3**, 1800337 (2019).

104. De Luna, P. *et al.* What would it take for renewably powered electrosynthesis to displace petrochemical processes? *Science* **364**, eaav3506 (2019).

105. Jouny, M., Luc, W. & Jiao, F. General Techno-Economic Analysis of CO_2 Electrolysis Systems. *Ind. Eng. Chem. Res.* **57**, 2165–2177 (2018).

106. Badwal, S. P. S., Giddey, S., Kulkarni, A., Goel, J. & Basu, S. Direct ethanol fuel cells for transport and stationary applications – A comprehensive review. *Appl. Energy* **145**, 80–103 (2015).

107. Hibino, T., Hashimoto, A., Yano, M., Suzuki, M. & Sano, M. Ru-catalyzed anode materials for direct hydrocarbon SOFCs. *Electrochimica Acta* **48**, 2531–2537 (2003).